

Tracer Transport in Three
Dimensions: Dispersion
of Methane on Mars,
Coupled Chemistry and
Dynamics on Exoplanets,
and Submesoscale Mixing
in the Ocean

Thesis by
Yangcheng Luo

In Partial Fulfillment of the Requirements for
the Degree of
Doctor of Philosophy

The logo for the California Institute of Technology (Caltech), featuring the word "Caltech" in a bold, orange, sans-serif font.

CALIFORNIA INSTITUTE OF TECHNOLOGY
Pasadena, California

2023
(Defended January 24th, 2023)

© 2023

Yangcheng Luo
ORCID: 0000-0003-0983-3650

ACKNOWLEDGEMENTS

After attending school for 21 years, I finally obtained my Ph.D. degree in Planetary Science from Caltech. I could not have fulfilled my academic dream at the age of 26 without the support of my family, my advisors, and my friends, to whom I would like to express my sincerest gratitude.

First of all, I would like to express my gratitude for my family. My parents put the seed of becoming a planetary scientist in the heart of a preschooler. My favorite bedtime story at the age of four was the legendary experiences of two astronauts on different planets—a story made up by my father. My mother bought me many Isaac Asimov's popular science books on astronomy and planetary science, and I read these books tens of times as a primary schooler. I still remember the amazing planets—arid Mars, hot Venus, big Jupiter, and beautiful Saturn rings. Influenced by my father, I wanted to become a scientist when I was very young, and all that I imagined about a scientist was a dedicated person studying astronomy and planetary science. My parents also encouraged me to pursue my academic dreams—they supported all my decisions, including going to the School of Physics at Peking University, choosing atmospheric science as my undergraduate major, flying over the Pacific to study, and coming to Caltech. They set examples for how passionate and focused a person should be.

I would also like to thank my grandparents for raising me when I was a primary schooler. Although they didn't have a chance to receive good education seventy years ago, they supervised me and made sure I fostered good habits of studying, which are the base of all my academic achievements. They prepared three meals a day for me for almost fifteen years until I left home for high school. I also learned to be an upright and sincere person from them.

Next, I would like to thank my advisors. Professor Yuk L. Yung taught me not only skills, but also the philosophy for research and life. From so many conversations with him, both academic and casual, over the past five years, I have realized many truths about science, research, and life. I realized that experiments (or missions for planetary science) are the real driving force for scientific advances. I also learned to grasp the main contradiction and avoid wasting time on trivial details—something that bothered me a lot when I first learned to do

research. He taught me how to, and provided me with many chances to collaborate. He showed me a very good example of how to advise students and manage a research group. His passion for science and diligence are something I will remind myself of for my whole life. He also showed me how to combine personal pursuits for both science and art, and eventually live a meaningful life. His insights for history and culture are extremely thought-provoking.

I feel like working with a genius at every meeting with Professor Jörn Callies. I am amazed every time he walks up to the blackboard in his office in the middle of a discussion and writes down equations swiftly without any thinking. I am also impressed by his passionate for science—he could walk into my office and continue a discussion five minutes after I left his office, by the time of which he might have come up a solution or some new ideas. He also showed me how to become a good teaching assistant and a good professor. He reviewed every problem set that I graded and gave me suggestions on how to point out students' mistakes while still encouraging them. He wrote very detailed class notes and designed the best problem sets that I have ever seen.

I especially want to thank Professor Yongyun Hu and Professor Jun Yang. They are the ones who introduced me into the research of planetary science when I was a sophomore, and they encouraged me to choose the academic career for my life. They are always supportive, both in research and in life. At Professor Hu's group meetings, I learned the paths to a meaningful life—an academic life that contributes to human advancement. Over so many phone calls with Professor Hu after I left Peking University, I was convinced to stay in academia and return to China in the future. At every one-on-one meeting with Professor Yang, I learned so many things, from how to solve specific technical problems with models, to how to relate different things and come up with new ideas. I was greatly encouraged by Professor Yang every time he appreciated the value of my work, no matter how tiny it was. Professor Hu and Professor Yang hosted me while I was in China in 2021. They provided me with computational resources and gave me good ideas which made Chapter 3 of this thesis possible. They also offered me an opportunity to attend the first National Planetary Science Conference and engage with colleagues in June 2021. They are my true role models.

In particular, I would like to thank my girlfriend and my spiritual partner, Jiaxin Xu, who made my lonely days at home during the two years of the pandemic full of fun, inspirations, and love. Professor Yung said, finding a good wife is more difficult than completing a PhD. I think keeping a long-distance relationship across the Pacific for two years is even more challenging, but we did it. Knowing that I love *the Story of the Stone*, she started reading it. Knowing that I was interested in world politics, she often listened to my lengthy speeches with patience and discussed with me about a multitude of topics, from modernization to cyberpunk, and from epidemiology to pedagogy. I came up with so many ideas, for both research and life, while talking with her, and these ideas made me excited about life over and over again. She also supervised me on sleeping early and doing regular exercise to keep fit during the pandemic. Coincidentally, in order to meet her in person (and also to escape from Los Angeles, one of the hardest hit areas by the pandemic), I went back to China in 2021, which gave me a chance to continue on my unpublished work with Professor Hu that led to the unexpected discoveries in Chapter 3 of this thesis. I am indebted to Jiaxin for such a long time of separation, but I hope I can ultimately make a bright future for both of us.

Next, I want to thank my thesis committee advisors, Professor Bethany L. Ehlmann and Professor Andrew P. Ingersoll. Professor Ehlmann showed her great interest in my work on Mars methane (Chapter 2 of this thesis), which encouraged me to better complete this project. She also raised many valuable questions that I later tried to answer using the methodology I developed. Professor Ingersoll has such a wide interest and passion in so many research areas of planetary science. He showed me the best example of how one can find happiness from research for a whole life.

I also would like to thank my collaborators, Dr. Michael A. Mischna, Professor John C. Lin, Benjamin Fasoli, Professor Ronald W. Klusman, Dr. Pin Chen, Dr. Xu Zhang, Dr. Stanley P. Sander, Dr. Jiazheng Li, Danica Adams, Professor Cheng Li, Dr. Michael Zhang, and Dr. Renyu Hu. They shared great ideas with me and provided valuable advice on my research projects. I cherish every fruitful discussion with them. Among them, I especially want to thank Dr. Michael A. Mischna, who has always been very responsive to my requests for data and inquiries. I want to thank him for taking his time after work to run the Mars GCM and prepare the wind data for me, without which Chapter 2 of the thesis would not be possible.

I would also like to thank the professors of the Caltech courses I have taken—Professor Tapio Schneider, Professor Andrew F. Thompson, Professor Victor Tsai, Professor Christian Frankenberg, Professor Jörn Callies, Professor Andrew P. Ingersoll, Professor Paul O. Wennberg, Professor John H. Seinfeld, Professor Andrew F. Thompson, Professor Brian P. Wernicke, Professor Bethany L. Ehlmann, Professor Robert W. Clayton, Professor Michael C. Gurnis, Professor Yuk L. Yung, Professor Konstantin Batygin, Professor David J. Stevenson, Professor Yaser Abu-Mostafa, and Professor Yisong Yue. The knowledge I learned from them forms the foundation of all my academic achievements. The field trips to the Catalina Islands and the Death Valley are unforgettable memories in my entire life. It is so impressive that Professor Andrew F. Thompson spent two whole days on the oral final examinations when he interviewed students one by one. Professor Victor Tsai made his lectures easy to understand—I finally understood some basic principles of linear algebra four years after I first learned them in the classroom of Peking University. Professor Andrew P. Ingersoll encouraged me to carry on with my term project on polar vortices on Jupiter after the term ended. Although I didn't have enough time to finish this project in the end, working with him was so heuristic that I will never forget this special experience.

Professor Yuk L. Yung's research group—the Yuk Army—is a pool of talented people who have shared with me brilliant ideas and provided me with timely support. They also gave me a sense of belonging, making me feel like in a family. I want to acknowledge the support from Dr. Run-Lie Shia, Dr. Stuart J. Bartlett, Professor Zhao-Cheng Zeng, Professor Yuan Wang, Professor Chao Liu, Dr. Cheng Li, Dr. Peter Gao, Dr. Michael L. Wong, Dr. Siteng Fan, Dr. Tianhao Le, Dr. Jiazheng Li, Dr. Lixiang Gu, Danica Adams, Sihe Chen, and Jiani Yang, and thank them for keeping me company. During the pandemic when the campus was shut down, it is the communications with them that made me feel the warmth of the paused world.

I want to express my special thanks to my friends and roommates in Pasadena. They made me feel like home and alleviated my loneliness from the social distancing during the pandemic. I want to thank Sam Zhang, Heng Dong, Dr. Ignacio Lopez-Gomez, Dr. Lixiang Gu, Yongzhao Guo, Yida Li, Dr. Jin Sima, Daniel Echeverri, Dr. Siteng Fan, Tianzhe Zheng, Yang Zhang, Cheng Shen, Xiaoqiao Chen, Tian Xie, Sihe Chen, Maria Yu, Luna Bai, Ke

Liu, Jiaqi Fang, Professor Menglin Yu, etc. I spent the first Thanksgiving holiday after I arrived at Caltech with Sam Zhang. We cooked, watched horrors, and played ping-pong. She fearlessly tasted the food I first learned to cook and gave me great affirmation no matter how plain the food tasted. Heng Dong lived next door to me, and he often came over to my apartment to work on problem sets together. Discussing problems with a smart person like him kept my mind sharp and we had so much fun in coming up with solutions. I will never forget Office 222 in Linde Laboratory at 3 a.m., when Dr. Ignacio Lopez-Gomez and I were working hard on Professor Jörn Callies's physical oceanography problem sets. We both looked down upon each other's ideas to solve a problem but eventually adopted each other's solutions. Dr. Lixiang Gu lived near my apartment in the first year of the pandemic, when the strictest social distancing was implemented. She kept me company in the loneliest days—we often went out for a walk together after dinner. Dr. Siteng Fan took me to go skiing—my last happy experience before the pandemic started. I had a good time at the Joshua Tree National Park with Yongzhao Guo, Cheng Shen, and Maria Yu in October 2020. I had an unforgettable spring holiday at the Sequoia National Park, the Yosemite National Park, and California State Route 1 with Maria Yu, Ke Liu, and Jiaqi Fang in March 2022. Furthermore, I also want to thank my old friend since my freshman year at college, Zhenzi He, who has always been willing to discuss current affairs and politics with me, although we are on the two sides of the Pacific.

I would also like to thank my peers in the GPS Division—Sam Zhang, Heng Dong, Yongzhao Guo, Dr. Ignacio Lopez-Gomez, Sara E. Murphy, Clare E. Singer, Lily A. Dove, Maria Camarca, Mike Greklek-McKeon, etc, for the great time we spent together in the classroom and office. Discussion with them has always helped me better understand course materials.

I would also like to thank the alumni of Peking University and Caltech who shared exciting ideas with me and gave me invaluable support—Professor Wanying Kang, Professor Cheng Li, Professor Xi Zhang, Professor Da Yang, Dr. Zhihong Tan, Zeyuan Hu, Ziwei Wang, Bowen Fan, Hao Fu, Liyin He, and Yaoxuan Zeng, etc. I look forward to attending every academic conference because it is so much fun to meet with them. Every conversation with them sparks new ideas.

I want to thank my high school dormmates and classmates in the United States—Dr. Baichuan Mo, Xinghe Jiang, and Jinzhao Li. Meeting with them every time brings me back to my high school years, when we were all courageous, ambitious, and ready to change the world. These memories have always encouraged me to take the challenge during my adventures into the uncharted waters of science.

I would like to thank my advisor and peers at the 2022 Rossbypalooza summer school—Professor Edwin Kite, Dr. Kaitlyn Loftus, Xinhuiyu Liu, Bowen Fan, Ziwei Wang, Xuan Ji, Yaoxuan Zeng, and Huanzhou Yang, etc. Living and working with a group of enthusiastic young scientists for two weeks is such a wonderful experience!

I would like to express my sincere gratitude for my high school teachers, especially Junying Zong and Dan Lyu, who gave me opportunities to participate in scientific research at the Chinese Academy of Sciences when I was a highschooler. I chose to study physics at Peking University in large part because of this special high school experience. They also showed their full support for my decision to pursue science in the long run, which I deeply appreciate.

Finally, I would like to thank the staffs in the GPS Division—Julie Lee, Margaret Carlos, Ulrika Terrones, and Nora J. Oshima—for helping me process administration issues. I wouldn't be able to focus on my research without their help. I also want to thank Scott A. Dungan, who helped me solve computer problems, and Laura Flower Kim and Daniel Yoder at the International Student Programs, who are so responsive to my inquiries about immigration documents.

ABSTRACT

One-dimensional (1D) modeling from a horizontally averaged perspective can oftentimes greatly simplify problems in atmospheric and oceanic sciences and thus capture leading-order physics. Meanwhile, 1D numerical models have great advantages such as numerical stability and time efficiency, hence they are widely used to gain insights into complex problems. However, oversimplification by 1D models may cause failures in finding solutions, revealing novel phenomena, and discovering scaling laws in the three-dimensional (3D) real world, and those are when 3D thinking proves its value. Also, the rise in computational power has allowed investigations using 3D numerical models. This thesis discusses three examples of how 3D modeling transcends the limitations of 1D modeling and reveals new solutions, phenomena, and scalings in planetary atmospheres and Earth's ocean.

Chapter 2 is focused on the dispersion of methane plumes on Mars and how it can reconcile the discrepancy between observations. In the face of ostensibly inconsistent observational results of methane on Mars, we adopt a novel approach—inverse Lagrangian modeling in 3D space—to find the scenarios in which the inconsistency in the observations can be reconciled and locate the methane source. We find that the inconsistency between the results of the near-surface *in situ* methane measurements and the satellite remote sensing measurements can be reconciled if and only if an active methane emission hot spot is located in the immediate vicinity of the Curiosity rover in northwestern Gale crater, or unknown physical or chemical processes are rapidly removing methane.

Chapter 3 presents a novel phenomenon that could exist on exoplanets—self-sustained photochemical oscillations, which is only produced by 3D atmospheric models. We use a 3D, fully coupled, chemistry-radiation-dynamics model to simulate the ozone-NO_x-HO_x photochemistry in the atmosphere of a tidally locked Earth-like exoplanet in the circumstellar habitable zone, and calculate the transmission spectra during transits. We find that under certain conditions, biological nitrogen fixation like the one on the Earth can drive large-magnitude, self-sustained photochemical oscillations in the atmospheres of terrestrial exoplanets. The resulting large temporal variability in ozone abundance on exoplanets, if

observed, may suggest a strong surface NO_x emission source, which could signal extrasolar life participating in the nitrogen cycle on exoplanets. Fully coupled, three-dimensional atmospheric chemistry-radiation-dynamics models can reveal new phenomena that may not exist in one-dimensional models, and hence they are powerful tools for future planetary atmospheric research.

Chapter 4 uses a 3D fluid dynamics model to study the vertical exchange in the upper part of Earth's ocean that potentially has great implications for the marine ecosystem. We develop scaling laws for the exchange rate between the surface ocean and the ocean interior which is critical to the rate of nutrient supply to phytoplankton near the ocean surface. These scaling laws could substitute the crude 1D parameterizations that are currently widely used in ocean models. We find that submesoscale turbulence energized by baroclinic instability in the ocean mixed layer can induce tracer exchange between the surface ocean and the ocean interior. Various environmental physical parameters affect the exchange rate. The exchange is stronger where the ocean mixed layer is thicker, the Richardson number (defined as the ratio of the squared buoyancy frequency to the squared vertical shear of the horizontal flow) of the thermocline is smaller, and the Richardson number of ocean mixed layer is larger. The associated nutrient supply from the ocean interior to the surface ocean is also expected to be stronger under these conditions.

PUBLISHED CONTENT AND CONTRIBUTIONS

Luo, Y., et al. (2021). “Mars methane sources in northwestern Gale crater inferred from back-trajectory modeling”. In: *Earth and Space Science*, **8**, e2021EA001915. doi: 10.1029/2021EA001915.

Y. L. participated in the conception of the project, developed the Mars version of the inverse Lagrangian model, performed the back-trajectory simulations and analyses, plotted the figures, and wrote the manuscript.

—*Used in Chapter 2*

Luo, Y., et al. (2023). “Beyond steady states: Coupled atmospheric chemistry, radiation and dynamics of an exoplanet produce self-sustained oscillations”. Submitted.

Y. L. participated in the conception of the project, performed the three-dimensional chemistry-radiation-dynamics simulations, analyzed the simulation results, plotted the figures, and wrote the manuscript.

—*Adapted for the contents in Chapter 3*

Luo, Y., & Callies, J. (2023). “Exchange between the mixed Layer and thermocline induced by mixed layer instability”. In preparation.

Y. L. participated in the conception of the project, performed the linear stability analysis and nonlinear simulations, analyzed the simulation results, plotted the figures, and wrote the manuscript.

—*Adapted for the contents in Chapter 4*

TABLE OF CONTENTS

Acknowledgements	iii
Abstract.....	ix
Published Content and Contributions	xi
Table of Contents	xii
List of Illustrations	xiv
List of Tables.....	xvi
Chapter 1: Introduction	1
1.1 Overview	1
1.2 Transport and dispersion of methane plumes on Mars	3
1.3 Self-sustained oscillations in photochemistry and atmospheric dynamics on exoplanets.....	4
1.4 Submesoscale vertical mixing in the upper ocean.....	6
Chapter 2: Mars Methane Sources in Northwestern Gale Crater Inferred From Back-Trajectory Modeling.....	7
2.1 Abstract	8
2.2 Introduction	8
2.3 Methods.....	12
2.3.1 GCM wind simulations.....	12
2.3.2 Inverse Lagrangian analysis	14
2.4 Results	16
2.4.1 Categorization of methane spikes.....	16
2.4.2 Atmospheric circulations	17
2.4.3 Influential upstream regions	18
2.4.4 Minimum methane emission	21
2.4.5 Consecutive methane measurements.....	24
2.5 Conclusions	26
2.6 Appendix	27
Chapter 3: Beyond Steady States: Coupled Atmospheric Chemistry, Radiation and Dynamics of an Exoplanet Produce Self-Sustained Oscillations	39
3.1 Abstract	40
3.2 Introduction	40
3.3 Results	43
3.3.1 Periodic oscillations of trace gas abundances	43
3.3.2 Mechanisms behind the self-oscillations.....	44
3.3.3 Observational prospects.....	51
3.4 Discussion	52
3.5 Materials and Methods.....	54
3.5.1 Fully coupled 3D atmospheric chemistry-radiation-dynamics simulations	54
3.5.2 Stellar spectrum	55

3.5.3 Calculation of the transmission spectra.....	56
3.6 Appendix	57
Chapter 4: Exchange Between the Mixed Layer and Thermocline Induced by Mixed Layer Instability.....	62
4.1 Abstract	63
4.2 Introduction	63
4.3 Linear stability analysis	66
4.3.1 Model formulation	66
4.3.2 Results	71
4.4 Nonlinear simulations	78
4.4.1 Model formulation	78
4.4.2 Results	82
4.5 Discussion and summary	90
Chapter 5: Conclusions	95
Bibliography	97

LIST OF ILLUSTRATIONS

<i>Number</i>	<i>Page</i>
2.1 TLS methane signals versus Mars season and local time	10
2.2 Simulated winds in the bottom layer of MarsWRF at $L_s = 81.84^\circ$	18
2.3 Maps of time-integrated STILT footprint.....	19
2.4 Minimum amount of methane emitted from putative emission locations ...	22
2.5 Comparison between the footprint maps for background and Spike 6.....	25
2.S1 MarsWRF domains on the four nesting levels.....	27
2.S2 MarsWRF-simulated winds averaged over the lowest 5 km	28
2.S3 Dispersion of backward-traveling particles within Gale crater	29
2.S4 Vertical dispersion of particles in a STILT simulation.....	30
2.S5 Maps of time-integrated STILT footprint for all methane spikes.....	31
2.S6 Minimum amount of methane emitted for all methane spikes	33
2.S7 An example time series of the footprint magnitude for Spike 1	34
2.S8 Decay of STILT footprint with distance	35
2.S9 Time of maximum STILT footprint at all putative emission sites	36
2.S10 Maximum area of the emission regions where certain amounts of emitted methane can produce the observed methane spikes	37
3.1 Time variability of O_3 and NO_x abundances	44
3.2 Key processes in the negative feedback loop that drive self-oscillations....	45
3.3 Evolution of the self-oscillatory system within a cycle	49
3.4 Atmospheric dynamics in the stratosphere greatly affects ozone abundance.....	50
3.5 Detectability of the ozone layer and its variability.....	52
3.6 The M-dwarf stellar spectrum used in the simulation.....	56
3.S1 Lightning NO emission depends on the location of the substellar point...	57
3.S2 Spatial distributions of ozone and some important atmospheric variables in different stages of the oscillations	58

3.S3 Average cloud distribution	59
3.S4 Observational prospects in a cloudy scenario	60
3.S5 Sea surface temperature and sea ice distribution	61
3.S6 Time series of global mean column abundances of O ₃ and NO _x with different NO emission fluxes	61
4.1 Configuration of an Eady model for the mixed layer and thermocline	67
4.2 Spatial structures of the modes of mixed layer instability	72
4.3 Large thermocline Richardson numbers suppress vertical velocity at the layer interface.....	73
4.4 Dependence of the behaviors of the linear model on the Richardson numbers of the two layers.....	75
4.5 Evolution of the perturbation buoyancy at the mixed layer midplane.....	83
4.6 Binary tracer and PV trace each other in the nonlinear simulations.....	84
4.7 The amount of thermocline water entrained into the mixed layer is inversely proportional to the Richardson number difference between the mixed layer and the thermocline in the initial state.....	85
4.8 The transition from the linear phase to the nonlinear phase happens when the surface relative vorticity reaches f	89
4.9 Horizontally averaged upward fluxes of the binary tracer and PV.....	92
4.10 Homogenization of the binary tracer concentration and hydrostatic PV in the mixed layer.....	93

LIST OF TABLES

<i>Number</i>	<i>Page</i>
2.S1 TLS methane measurements investigated in Chapter 2.....	38

INTRODUCTION

1.1 Overview

The three-dimensional (3D) planetary atmospheres are not isotropic; instead, the horizontal direction and the vertical direction are distinct from each other. The aspect ratios of planetary atmospheres are small—for example, the thickness of Earth’s atmosphere, measured from the surface to the exobase, is less than 1,000 km, whereas the horizontal dimension of Earth’s atmosphere, measured by the perimeter of Earth, is about 40,000 km, 1–2 orders of magnitude larger than the vertical dimension. From the perspective of atmospheric dynamics, the thickness of Earth’s atmosphere is measured by its scale height, which is less than 10 km, and the horizontal dimension of Earth’s atmosphere is measured by the Rossby deformation radius of large-scale dynamics, which is on the order of 1,000 km, two orders of magnitude larger than the vertical dimension. The small aspect ratio results in greater spatial variability and hence richer physics in the vertical direction than in the horizontal direction. Meanwhile, the atmosphere has a well-defined lower boundary, and is photochemically and radiatively forced at its upper and lower boundaries. These characteristics inspired the invention of one-dimensional (1D, in altitude) radiative-convective models and photochemical-radiative-convective models that only explicitly resolve the altitude dependence but ignore or parameterize horizontal heterogeneity. These characteristics also allow 1D models to capture leading order physics and chemistry of the atmosphere. The time efficiency and numerical stability have also made 1D models popular in atmospheric research. Application of 1D models (e.g., Allen et al., 1981) has proved to be successful in reproducing vertical thermal structure of the atmosphere (e.g., Manabe & Souffer, 1980) and chemical compositions of planetary atmospheres in the solar system (e.g., Yung & DeMore, 1982; Yung et al., 1984; Nair et al., 1994) and also explaining the underlying mechanisms. Given the success in 1D modeling, 1D models have also been widely used to investigate the climate and photochemistry of extrasolar planets (e.g., Segura et al., 2003, 2005; Krissansen-Totton et

al., 2018; Lustig-Yaeger et al., 2019). In oceanography, 1D models (in depth) have also been used to study the turbulent mixing in the upper ocean as they are simple enough and easy to implement (e.g., Large et al., 1994; Van Roekel et al., 2018).

However, oversimplification by 1D models may cause failures in finding solutions, revealing novel phenomena, and discovering scaling laws in the three-dimensional (3D) real world. In particular, tracer transport by atmospheric or ocean circulations in 3D space is highly simplified in 1D models (e.g., represented by a “vertical effective vertical diffusivity” in atmospheric models), whereas in fact, tracer transport has its preferred directions in 3D space which are dictated by geofluid dynamics. Examples of failures or fallacies of 1D models can be found in Chapters 2–4 in this thesis. To overcome the problems with 1D models and to be more realistic, 3D models have been developed, and the rise in computational power has allowed wide applications using 3D numerical models. In 3D atmospheric models, different atmospheric processes, such as atmospheric transport influenced atmospheric dynamics, photochemistry, radiative transfer, cloud physics, etc, can be fully coupled, which allows more feedbacks to be included. This greatly enhances the complexity of atmospheric models and their potential to reveal novel solutions, phenomena, and scalings. 3D oceanic models can elucidate the geofluid dynamics underlying tracer transport. This thesis discusses three examples of how 3D modeling transcends the limitations of 1D modeling in planetary atmospheres and Earth’s ocean.

The first part of this thesis is about 3D modeling for the transport and dispersion of methane plumes on Mars. The second part of this thesis is about large-magnitude, periodic, self-sustained oscillations of atmospheric chemistry on exoplanets—a special phenomenon only produced in 3D fully coupled chemistry-radiation-dynamics models of the atmosphere. The third part of this thesis is about 3D modeling for the vertical exchange caused by submesoscale dynamics of the upper ocean that leads to new understandings of the physics and new scaling laws. It is the author’s intention that the three chapters of this thesis altogether can demonstrate the power of 3D modeling in atmospheric and oceanic sciences.

1.2 Transport and dispersion of methane plumes on Mars

Advances in astronomy in the early 20th century made it possible to measure the concentration of trace gases in the atmosphere of Mars using ground-based telescopes, and soon afterwards the presence of methane in the Martian atmosphere was reported for the first time (Krasnopolsky et al., 2004). As a reduced gas in a highly oxidized environment, methane has been proposed as a potential biosignature, as life can make improbable chemistry happen, causing chemical disequilibrium. The fact that more than 90% of methane in the Earth's atmosphere has biological origins (Cicerone & Oremland, 1988) also adds to the speculation that methane on Mars has ties to past or extant life. Follow-up observational campaigns reported positive detections, but with inconsistent atmospheric concentrations (e.g., Formisano et al., 2004; Geminale et al., 2008). Methane concentration in the Martian atmosphere was even reported to be highly variable in time (Mumma et al., 2009), which contradicts the long residence time predicted by standard photochemical models (Formisano et al., 2004; Lefèvre & Forget, 2009) and implies unknown removal mechanisms. The landing of the *Curiosity* rover at Gale crater in 2012 initiated a new era of methane measurements, when powerful spectrometers on or orbiting Mars can reduce measurement uncertainties down to tens of parts-per-trillion. Results from *Curiosity* surprisingly added to the puzzle of methane—high time variability in methane concentration was confirmed, and the sudden rises and falls of the ambient methane concentration require further explanation (Webster et al., 2015, 2018). In order to measure the methane concentration in the mid- to high altitudes of the Martian atmosphere—where the sensor of *Curiosity* cannot sample, the ExoMars Trace Gas Orbiter (TGO) started orbiting Mars in 2016. Surprisingly, it soon reported non-detections, adding to the conundrum that some mysterious removal mechanisms are shortening the residence time of methane on Mars, thus allowing spatial heterogeneity (Korablev et al., 2019; Knutsen et al., 2021; Montmessin et al., 2021).

1D photochemical models not including a planetary boundary layer have failed to reconcile the discrepancy between the *Curiosity* results and the TGO results (e.g., Grenfell et al., 2022). After considering the planetary boundary layer, some 1D models can crudely explain the discrepancy, but horizontal transport, which is equivalently important to the *Curiosity*

methane measurements, is neglected in such models (Moores et al., 2019a, 2019b). If both the *Curiosity* measurements and the TGO measurements returned credible results, then the only possible scenario is that by chance *Curiosity* landed near a methane emission hot spot, so it is heavily influence by near-field effects. Chapter 2 of this thesis digs into this scenario, and constrained the conditions under which the *Curiosity* results and the TGO results are compatible with each other by 3D transport and dispersion modeling.

1.3 Self-sustained oscillations in photochemistry and atmospheric dynamics on exoplanets

Since 1992, more than 5000 exoplanets have been discovered, and among them, up to 60 are believed to be potentially habitable exoplanets. Many kinds of remotely detectable signs of life for exoplanets have been proposed, and they fall into four broad categories: gaseous biosignatures—spectral features of atmospheric constituents that are more likely to be produced by life than abiotic processes, surface biosignatures—spectral properties of planetary surface that come into being because of life, temporal biosignatures—temporal variability of planetary spectra caused by life, oftentimes time-dependent modulations by a biosphere acting on a planetary environment, and technosignatures—signs of technological civilization (Schwieterman et al., 2018). The observation of these biosignatures demands high-precision spectroscopy, which is becoming a reality with new generations of space telescopes such as James Webb Space Telescope (JWST), Habitable Exoplanet Observatory (HabEx), and the Large UV/Optical/IR Surveyor (LUVOIR).

To predict prospective gaseous biosignatures and gas-based temporal biosignatures that can be detected in the future, a synergistic modeling approach using atmospheric chemistry models and radiative transfer models is adopted. Atmospheric chemistry models simulate the response of atmospheric constituents to biological sources and sinks under various stellar and planetary contexts, and radiative transfer models simulate the planetary spectra, either transmission or reflection, after starlight travels through the planetary atmosphere. To simulate atmospheric chemistry, one-dimensional (in altitude) photochemistry-radiation models have been widely used (e.g., Segura et al., 2003, 2005), in which atmospheric

dynamics and the transport of atmospheric constituents are parameterized using artificial vertical diffusivity at different altitudes. One-dimensional models can provide good insights, but the lack of explicit representation of the feedbacks between chemistry-radiation and dynamics-transport makes the results questionable. With recent advances in computational efficiency, fully coupled, three-dimensional chemistry-radiation-dynamics models have been increasingly employed to simulate exoplanetary atmospheres (Proedrou & Hocke, 2016; Chen et al., 2018, 2019, 2021; Yates et al., 2020), which are expected to yield more credible simulation results and discover novel phenomena that are missed by one-dimensional models.

In photochemical studies of planetary atmospheres, it is generally believed that if all external forcings, such as insolation and emission rates, are non-varying, any initial value problem can ultimately reach a unique steady state. In fact, counterexamples have been found in idealized box models based on parameters of the Earth's atmosphere, but they have received insufficient attention due to the lack of applicability in Earth's real atmosphere that is constantly disturbed by varying external conditions. In Chapter 3 of this thesis, we use fully coupled, three-dimensional chemistry-radiation-dynamics models to demonstrate that self-sustained, large-magnitude oscillations in photochemistry are possible on exoplanets, and they require a strong source of nitrogen oxides into the atmosphere, the latter most likely biogenic. We also demonstrate that such oscillations are remotely detectable and can be distinguished from other types of temporal variability caused by abiotic processes. Therefore, we propose that such self-sustained, large-magnitude photochemical oscillations are a novel type of exoplanet biosignature. This can be categorized as a temporal biosignature, but it expands the conventional definition of a temporal biosignature which is based on time-dependent modulations by a biosphere; instead, in our case, the influence by the biosphere in the form of nitrogen oxide emission is non-varying in time, and the temporal variability results from self-oscillations in the atmosphere with the presence of a strong emission flux. Our findings highlight the need to revisit exoplanetary spectra over multidecadal timescales, from which unexpected variability might be found. The findings also highlight the need to use fully coupled, three-dimensional chemistry-radiation-dynamics models to study

planetary atmospheres, which are shown to have a chance of revealing novel processes in planetary atmospheres.

1.4 Submesoscale vertical mixing in the upper ocean

Photosynthesis of phytoplankton in the surface ocean contributes more than half of the total primary productivity in Earth's biosphere (Field et al., 1998). The understanding of how phytoplankton completes its life cycle and affects marine ecology must be based on the understanding of the fluid dynamics of sea water—the constantly moving living space for phytoplankton, as the latter provides access to light and nutrients (e.g., nitrogen and phosphorus)—the prerequisites for metabolism—for phytoplankton.

The vertical exchange between the ocean mixed layer and the thermocline affects both the light conditions and the nutrient conditions. On one hand, entrainment of nutrient-rich and high potential vorticity thermocline water into the mixed layer can supply nutrients for phytoplankton growth and help restratify the mixed layer, enhancing light exposure for phytoplankton. On the other hand, subduction of mixed layer water into the ocean interior moves phytoplankton away from the euphotic zone, reducing light exposure. Therefore, it is important to investigate how the vertical exchange happens and how it depends on environmental parameters.

Traditional understanding of the vertical mixing by turbulence in the upper ocean is from a 1D model—the K-profile parameterization (KPP) that recommends the matching of interior diffusivities and their gradients to the values predicted by KPP in the ocean surface boundary layer. Although widely implemented in ocean models, this 1D model does not elucidate the underlying physics and fails to capture scaling laws for the dependence of the vertical mixing on environmental parameters. In Chapter 4 of this thesis, we use 3D modeling to elaborate on the underlying physics of how submesoscale turbulence transports nutrients from the ocean interior to the surface ocean, and develop scaling laws for its dependence on environmental conditions.

Mars Methane Sources in Northwestern Gale Crater Inferred From Back-Trajectory Modeling

Yangcheng Luo¹, Michael A. Mischna², John C. Lin³, Benjamin Fasoli³, Xiang Cai⁴, and Yuk L. Yung^{1,2}

¹Division of Geological and Planetary Sciences, California Institute of Technology,
Pasadena, CA, USA

²Jet Propulsion Laboratory, California Institute of Technology, Pasadena, CA, USA

³Department of Atmospheric Sciences, University of Utah, Salt Lake City, UT, USA

⁴Columbia University, New York, NY, USA

Luo, Y. et al. (2021). “Mars methane sources in northwestern Gale crater inferred from back-trajectory modeling”. In: *Earth and Space Science*, **8**, e2021EA001915. doi: 10.1029/2021EA001915.

2.1 Abstract

During its first seven years of operation, the Sample Analysis at Mars Tunable Laser Spectrometer (TLS) on board the Curiosity rover has detected seven methane spikes above a low background abundance in Gale crater. The methane spikes are likely sourced by surface emission within or around Gale crater. Here, we use inverse Lagrangian modeling techniques to identify upstream emission regions on the Martian surface for these methane spikes at an unprecedented spatial resolution. Inside Gale crater, the northwestern crater floor casts the strongest influence on the detections. Outside Gale crater, the upstream regions common to all the methane spikes extend toward the north. The contrasting results from two consecutive TLS methane measurements performed on the same sol point to an active emission site to the west or the southwest of the Curiosity rover on the northwestern crater floor. The observed spike magnitude and frequency also favor emission sites on the northwestern crater floor, unless there are fast methane removal mechanisms at work, or either the methane spikes of TLS or the non-detections of ExoMars Trace Gas Orbiter cannot be trusted.

2.2 Introduction

Almost all of the methane in the present-day Earth's atmosphere can be traced back to biological origins (Cicerone & Oremland, 1988). Extending this observation to Mars, the presence of methane in its atmosphere could be a biosignature on this seemingly lifeless planet (Yung et al., 2018). Alternative, abiotic methane production mechanisms on Mars invoke past or present geological activity (reviewed in Oehler & Etiope, 2017) such as serpentinization (Oze & Sharma, 2005), which would indicate the presence of liquid water, an indispensable ingredient for life. Abundant methane in the ancient Martian atmosphere could also provide a solution to the conflict between the Faint Young Sun and a warm surface suggested by fluvial and lacustrine features on Mars (e.g., Kite et al., 2017).

In the past two decades, the significance of methane in the Martian atmosphere has motivated a number of remote sensing observations aimed at both retrieving the methane abundance in the Martian atmosphere and mapping out its spatial distribution. These observations have reported inconsistent and highly variable methane concentrations

(Krasnopolsky et al., 2004; Formisano et al., 2004; Geminale et al., 2008; Mumma et al., 2009; Fonti & Marzo, 2010; Krasnopolsky, 2012; Aoki et al., 2018; Giuranna et al., 2019). To overcome the technical challenges faced by remote sensing observations, the Tunable Laser Spectrometer (TLS; Mahaffy et al., 2012) on board the *Curiosity* rover was sent to Gale crater to make *in situ* measurements. During 7.1 years of operation as of January 2020, twenty direct-ingest measurements and sixteen enrichment measurements (refer to Webster et al. (2015) and Webster et al. (2018) for the descriptions for the two measurement types) revealed a baseline level of ~ 0.41 parts-per-billion-by-volume (ppbv) (Webster et al., 2018), with episodic spikes up to ~ 21 ppbv (Webster et al., 2021) as summarized in Fig. 2.1. These spikes have been interpreted as discrete methane emission events (Webster et al., 2015, 2018). Notably, the latest ~ 21 ppbv methane spike was the first spike detected in an enrichment measurement. It has a much higher signal-to-noise ratio than the earlier spikes detected in direct-ingest measurements; therefore, it has increased the credibility of the previous methane spike observations. Concurrently, the ExoMars Trace Gas Orbiter (TGO) has made solar occultation measurements of methane concentration at mid- to high-altitudes. However, it has reported stringent upper limits down to 0.02 ppbv (Korablev et al., 2019; Knutsen et al., 2021; Montmessin et al., 2021). Assuming methane is a long-lived species with a 330-year lifetime as indicated by standard photochemical models (Lefèvre & Forget, 2009), it should be uniformly mixed throughout the Martian atmosphere, so TGO's stringent upper limits have been interpreted as an upper limit for methane concentration in the entire atmosphere, which is contradictory to TLS's significantly more elevated ~ 0.41 ppbv background level. But some mechanisms have been proposed to reconcile this inconsistency. For example, TLS performed all its measurements in the near-surface planetary boundary layer (PBL), and methane, if released from the surface, could accumulate in the shallow nighttime PBL (Moore et al., 2019a, 2019b). Some speculative fast removal mechanisms that can possibly cause temporal and spatial inhomogeneity of methane concentration have also been proposed (Gough et al., 2010; Knak Jensen et al., 2014; Hu et al., 2016), which might also reconcile the inconsistency between the TLS and the TGO results. In this study, we first accept both the results from

TLS and TGO, and investigate the circumstances under which their discrepancies can be reconciled. We will then re-evaluate the probability of these circumstances.

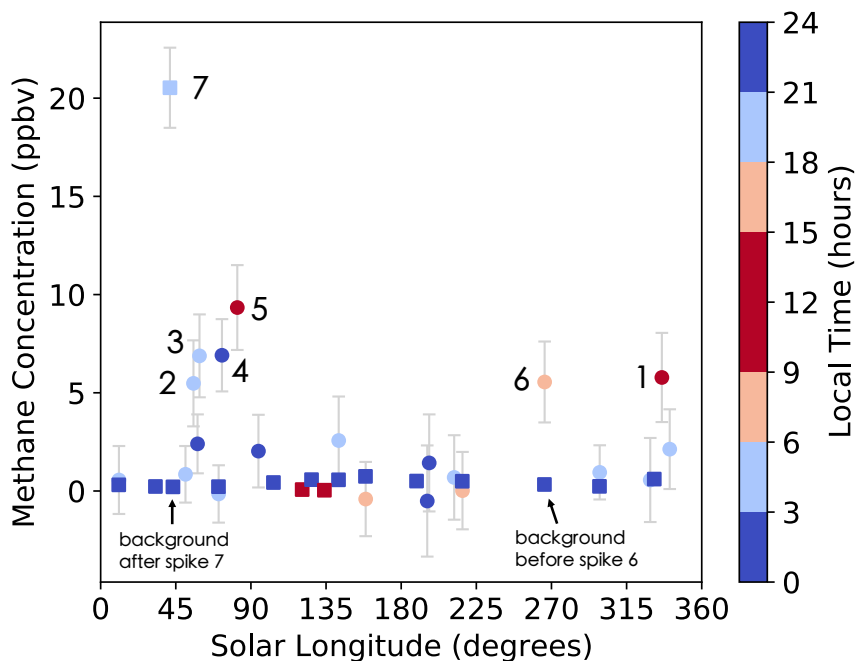


Figure 2.1. TLS methane signals versus Mars season and local time. The seven data points above 5 ppbv are regarded as “methane spikes” with their indices labelled. The twenty-nine data points below 5 ppbv are regarded as the background abundance. Two background-level measurements are also marked, one performed immediately before the detection of Spike 6 and the other after Spike 7. Direct-ingest measurements are shown in circles. Enrichment measurements are shown in squares. Colors show the local time of methane ingestions. Error bars show $\pm 1 \sigma$ uncertainty. Adapted from Webster et al. (2018, 2021).

Assuming the existence of methane on Mars is real, its origin will have profound implications for geology and astrobiology. Identification of the methane’s origin requires that we first find the surface emission sites, results from which can inform future missions of high priority landing sites and enable them to directly probe the methane source. The results can also guide orbiting instruments to better focus their methane observation strategies.

Inferring the locations of methane emission sites requires correct modeling of complex atmospheric transport processes. An early attempt to do so involved using a diffusion model to represent the spread of observed methane plumes (Mumma et al., 2009),

which was shown to be oversimplified by addressing the importance of advection by bulk wind (Mischna et al., 2011). More recently, the Global Environmental Multiscale (GEM)-Mars general circulation model (GCM) was used to simulate methane transport and then a statistical approach based on the idea of simultaneous satisfaction of multiple observational constraints was used for methane source localization (Giuranna et al., 2019). Results suggested an emission region to the east of Gale crater for TLS's first methane spike (Spike 1 in Fig. 2.1). Later, the Mars Regional Atmospheric Modeling System (MRAMS) mesoscale model was used to simulate the transport and dispersion of methane plumes emitted from ten selected source regions around Gale crater (Pla-García et al., 2019). Substantial dilution during tracer transport was observed, which demonstrates the importance of incorporating turbulent dispersion into tracer transport modeling. Among all the ten emission region candidates, the region to the northwest of the crater was favored, different from the prior findings of Giuranna et al. (2019).

The aforementioned studies have all adopted a forward Eulerian approach to identify potential emission sites, in which the model integrates three-dimensional tracer fields forward in time and quantifies how much tracer released at a specific emission location at a specific time can ultimately reach the detector. However, this trial-and-error approach is computationally inefficient, as most of the injected methane does not reach the detector, so usually only a small number of putative emission sites are selected and studied in depth (e.g., Pla-García et al., 2019). Meanwhile, the spatial resolution of emission regions is limited by the size of GCM grid boxes. In commonly used GCMs that provide a global coverage, the size of grid boxes is typically a few degrees in latitude and longitude, or several hundred kilometers. Such GCMs have difficulty in differentiating emission sites within the 154-km diameter Gale crater (e.g., Giuranna et al., 2019).

In this work, we adopt an inverse Lagrangian approach (Lin et al., 2003, 2012) of emission site identification to overcome the challenges faced by the forward Eulerian approach. The inverse Lagrangian approach, also known as back-trajectory analysis, is widely used in the environmental science community to map out upstream emission regions (e.g., Lin et al., 2003; Gerbig et al., 2003; Lin et al., 2004; Kort et al., 2008;

Macatangay et al., 2008; Mallia et al., 2015). An ensemble of computational particles, representing individual air parcels, is released from the detector at the time of detection and transported backwards in time within the model. The particles' transport pathways are determined by the bulk wind, and the particles are dispersed by parameterized subgrid-scale turbulence. The locations where backward-travelling particles are found within the PBL and, hence, are potentially affected by surface emission, are identified as potential upstream surface emission regions. The quantitative linkage between measured atmospheric mole fraction at the detector (e.g., TLS) and upstream surface fluxes can be established for any putative emission site via the number density of particles at that emission site (Lin et al., 2003; Fasoli et al., 2018). A single inverse Lagrangian simulation can quantify the influence of all upstream emission regions on a detection, and the spatial resolution of emission regions is not limited by the resolution of the underlying GCM. As such, high-resolution maps of all upstream emission regions can be produced, which is critical for the search for emission sites within and around a comparatively small crater like Gale.

2.3 Methods

2.3.1 GCM wind simulations

Since global, high-quality wind observations on Mars have been lacking to date, we use MarsWRF, a GCM of the Martian atmosphere, to simulate the wind fields necessary for inverse Lagrangian modeling. MarsWRF is derived from the terrestrial Weather Research and Forecasting (WRF) model and is a Mars-specific implementation of PlanetWRF (Richardson et al., 2007; Toigo et al., 2012). MarsWRF is a finite-difference grid-point model projected onto an Arakawa-C grid with user-defined horizontal and vertical resolutions. The vertical grid follows a modified-sigma (terrain-following) coordinate from the surface to ~80 km altitude. The total present-day atmospheric CO₂ budget is tuned to fit the Viking Lander annual pressure curves (~6.1 mbar), and both surface albedo and thermal inertia are matched to Mars Global Surveyor Thermal Emission Spectrometer (MGS-TES) observations (Christensen et al., 2001; Putzig et al., 2005), while

a Mars Orbiter Laser Altimeter (MOLA) topography base map is employed and scaled to the chosen model resolution (Smith et al., 2001).

Multiple studies in the past have validated MarsWRF through comparison of its behavior against data from the *Mars Global Surveyor* Thermal Emission Spectrometer (Lee et al., 2011; Toigo et al., 2012; Guzewich et al., 2013, 2014), the *Mars Reconnaissance Orbiter* Mars Climate Sounder (Guzewich et al., 2013), and the weather stations on board *Curiosity* (Fonseca et al., 2018; Newman et al., 2017) and *InSight* (Newman et al., 2020), showing MarsWRF reproduces observed atmospheric pressure, atmospheric and ground temperature, near-surface wind speeds and wind directions well.

MarsWRF permits multiple embedded “nests” with increasing spatial resolutions in a single model run. This allows atmospheric circulations influenced by small-scale topographic features to be fully resolved in a simulation while the simulation also covers the entire globe at a coarser resolution. In this study, we run MarsWRF at increasing horizontal resolutions around Gale crater. The final model consists of four nested levels, each scaled up in resolution (spatial and temporal) by a factor of three from its “parent” nest. Level 1 provides global coverage with a horizontal resolution of $2^\circ \times 2^\circ$ and a 60-second timestep. Level 2 encompasses an $80^\circ \times 80^\circ$ domain with a horizontal resolution of $0.67^\circ \times 0.67^\circ$ and a 20-second timestep. Level 3 encompasses a $26.67^\circ \times 26.67^\circ$ domain with a horizontal resolution of $0.222^\circ \times 0.222^\circ$ and a 6.67-second timestep. Level 4 encompasses an $8.89^\circ \times 8.89^\circ$ domain with a horizontal resolution of $0.074^\circ \times 0.074^\circ$ (4.4 km \times 4.4 km) and a 2.22-second timestep (Fig. 2.S1). Level 4 fully resolves the crater circulation. Two-way boundary conditions link a nested domain with its parent, with information being passed both up and down between parent and child domains. A description of this process may be found in Richardson et al. (2007). In order to speed up the simulations, we performed test simulations in advance to determine the duration of MarsWRF simulations on each nesting level. A particular nest is no longer necessary after 99% of the initially released backward-traveling particles have left the domain of that nest.

Given the lack of a global coverage of high-quality wind observations, it is impossible to reproduce precise “real” atmospheric circulations on spatial scales smaller than tens of

kilometers, as stochastic weather events can significantly impact wind speed and even direction. As a result, we do not intend to reproduce the “real” winds. Rather, we aim to produce “mean” winds that are representative of their respective season and time of day. For each TLS measurement, we repeat MarsWRF simulations for the corresponding Mars year four or five times, each time starting from a different initial condition. For each Mars year, the different rounds of GCM simulations are all driven by the same seasonally representative dust loadings. Results show slight variations in year-to-year conditions as a consequence of stochastic variability in the weather. The variance in results across the four or five times of simulation is, however, small.

On short timescales (<1 week), it is not anticipated there will be a significant change in the mean atmospheric conditions on Mars, so for each of the four or five rounds of wind simulation, we treat the sol of the methane measurement, and one, two, and three sols before and after the measurement as equally representative of the circulation pattern at the time of the TLS measurement, and release particles at the time of day of each measurement on all of the seven sols. In this way, we form an ensemble of ~30 back-trajectory simulations for each investigated TLS measurement. Then, for each measurement, we average the results of its ~30 back-trajectory simulations. This ensures that discrete weather patterns are smoothed out.

2.3.2 Inverse Lagrangian analysis

The wind fields from MarsWRF are used to drive the Stochastic Time-Inverted Lagrangian Transport (STILT) Lagrangian Particle Dispersion Model (Lin et al., 2003; Fasoli et al., 2018) to simulate plume transport and dispersion. STILT is based on the Hybrid Single Particle Lagrangian Integrated Trajectory (HYSPLIT) model (Draxler & Hess, 1998; Stein et al., 2015) that is extensively used in air quality, volcanic ash and industrial plume modeling, and STILT inherits all of the validated components of its predecessor. Although STILT was originally designed for terrestrial use, the Monin–Obukhov similarity theory for the PBL, along with the adherence to the well-mixed criterion (Thomson, 1987), a manifestation of the second law of thermodynamics, ensures

that the physics and fluid dynamics underlying STILT can be applied to all substantial planetary atmospheres, including the atmosphere of Mars, after modifications to some model parameters. The modified parameters include planetary radius, gas constant, angular rotation rate of the planet, surface gravity, dynamic viscosity of air, mean free path of air, molecular weight of air, surface air pressure, specific heat capacity of air, the map of land use, and the map of surface roughness length (Hébrard et al., 2012), etc.

In its application, STILT transports an ensemble of computational particles (ten thousand particles in each simulation in this study) from the site of the detector (here and henceforth, the location of the *Curiosity* rover) using time-reversed grid-scale wind plus a parameterized subgrid-scale turbulent velocity (Hanna, 1984). The timestep in STILT is determined dynamically based on the wind field, and typically ranges between one minute and ten minutes. When combined with a GCM, STILT linearly interpolates the simulated bulk wind from the GCM grid points to the precise positions of each particle at each timestep, and then displaces the particles according to the reversed wind arrow. Meanwhile, STILT adds a random velocity component, determined by a Markov chain process based statistically on the simulated meteorological conditions, to the bulk wind velocity. The random velocity represents turbulent motions that are unresolved by the GCM and results in dispersion of the particle cloud (Fig. 2.S3). Additionally, vertical mixing in the PBL is parameterized by vertically redistributing particles to random altitudes within the PBL (Fig. 2.S4). In the hyper-near field around the detector, an “effective mixing depth” smaller than the PBL thickness is calculated based on the homogeneous turbulence theory, and particles are redistributed within the effective mixing depth rather than the entire air column within the PBL (Fasoli et al., 2018). This will prevent the particles released near the surface from ascending to the top of the PBL instantaneously.

At every timestep in a back-trajectory simulation (which corresponds to a putative emission time), STILT tallies the instantaneous particle density in the PBL at all locations and generates a “footprint” map in units of ppbv μmol^{-1} (Lin et al., 2003), which quantifies the contribution of unit methane emission from a putative emission site to the methane mole fraction at the detector. The footprint value is proportional to the column-integrated

particle number density within the PBL and the molar mass of air, and inversely proportional to the PBL thickness and the average air density within the PBL (Lin et al., 2003). The footprint value at any location (representing a putative emission site) at any time (representing a putative emission time) is equal to the prospective methane mole fraction in units of ppbv above the background level (~ 0.41 ppbv) induced by $1 \mu\text{mol}$ of methane emission at that emission site and emission time. High footprint values indicate emission times and locations when and where emission casts strong influence over the detection. If integrated over all putative emission times, the footprint will measure the influence of a constant-flux emission on a detection, and the map of it will show all important upstream regions.

In computing the footprints, the domain is first gridded horizontally (a grid that is separate from that of the GCM) so that STILT can count the number of particles within each horizontal grid and calculate the particle density at all putative emission locations. The resolution of this grid becomes the resolution of the map of the emission regions. We use 2° as the resolution for the domain from 80°S to 80°N and from 60°E eastward to 140°W . For the subdomain from 17.6°S to 8.4°N and from 124.2°E to 150.4°E , we use a resolution of 0.2° , or ~ 11.8 km. For the subdomain from 6.64°S to 3.72°S and from 136.24°E to 139.16°E , we use a resolution of 0.02° , or ~ 1.18 km. We note that the definition of the STILT footprint in this study is slightly different from its original form in Lin et al. (2003). The new definition has excluded the influence of the grid size and the timestep of footprint calculation on footprint values.

2.4 Results

2.4.1 Categorization of methane spikes

We focus on the seven methane spikes reported by the TLS instrument during the 7.1 years of the *Curiosity* mission through January 2020 (Fig. 2.1, Table 2.S1). The seven spikes can be categorized based on the season and the time of day of their detections. In terms of seasons, Spikes 1 and 6 were detected in the late northern fall and winter. Spikes 2–5 and 7 were detected in northern spring. In terms of the time of day, Spikes 1 and 5

were detected in the early afternoon, and Spikes 2–4, 6, and 7 were detected between midnight and early morning. As a result, Spikes 1 and 6 share similar seasonal, regional and global circulation patterns, as do Spikes 2–5 and 7. Spikes 1 and 5 share similar diurnal crater circulation patterns, as do Spikes 2–4, 6, and 7. The similarity in atmospheric circulation patterns also manifests itself in the subsequent STILT footprint maps.

2.4.2 Atmospheric circulations

MarsWRF simulations show that the circulation at Gale crater consists of three components—a global meridional overturning circulation, a regional circulation, and a crater-scale circulation. Figure 2.2 shows an example of near-surface winds simulated by MarsWRF. In northern winter, the rising branch of the global meridional overturning circulation is centered in the southern hemisphere. Prevailing winds at the topographic dichotomy adjacent to Gale crater are southward and are particularly strong around 270° solar longitude ($L_s = 270^\circ$), when Spike 6 was detected. In northern spring, the large-scale prevailing winds at Gale crater are weak. The regional circulation is characterized by upslope northeasterlies along the topographic dichotomy in the afternoon, and downslope southwesterlies in the nighttime. The crater circulation is characterized by upslope winds along the inner crater rim and the slope of Mount Sharp in the afternoon, and downslope winds in the nighttime. The PBL thickness at Gale crater also undergoes a daily cycle between a nighttime minimum thickness of tens of meters, and a daytime maximum thickness of about three kilometers, similar to previous findings by Fonseca et al. (2018).

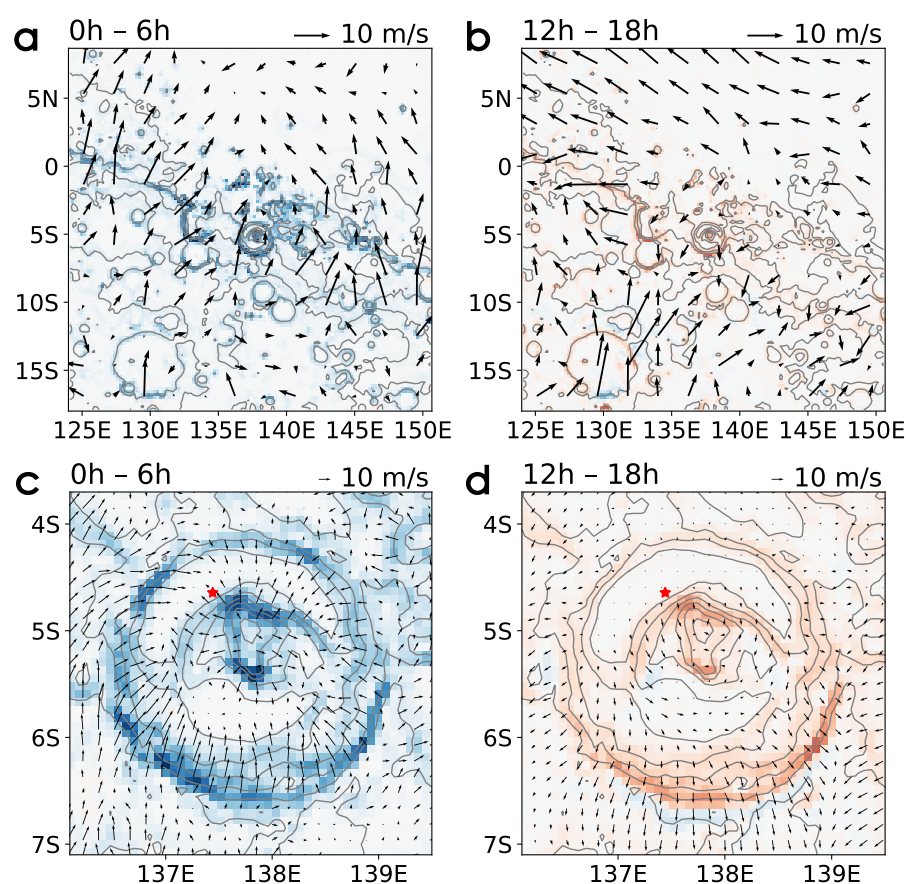


Figure 2.2. Simulated winds in the bottom layer of MarsWRF at $L_s = 81.84^\circ$ (Spike 5). The plotted data are an average over the six hours indicated by the time period on the upper left of each panel. (a) and (b) show the regional circulation, from which one can identify southwesterly downslope winds along the topographic dichotomy from midnight to sunrise, and northeasterly upslope winds from noon to sunset. (c) and (d) show the Gale crater circulation, from which one can identify downslope winds along the inner wall of the crater rim and along Mount Sharp from midnight to sunrise, and upslope winds from noon to sunset. The crater circulation is well resolved by MarsWRF. Red colors show rising air. Blue colors show sinking air. Contours show surface elevation. Red stars mark the position of *Curiosity*.

2.4.3 Influential upstream regions

Figure 2.3 shows the time-integrated footprints of Spikes 1 and 2. Refer to Fig. 2.S5 for the footprints of all seven methane spikes. Located on the heavily faulted topographic dichotomy that is favourable for microseepage, Gale crater as a whole has been proposed as a potential methane seepage site (Oehler & Etiope, 2017). Within Gale crater, the strongest footprint of Spike 1 lies to the north of the TLS detector (Fig. 2.3a), which is also the case for Spike 5 (Fig. 2.S5m). This means that these two early-afternoon measurements

are both more sensitive to the emission from the north than the emission from other directions. The similarity in the footprints for Spikes 1 and 5 is consistent with the similarity in the early-afternoon crater-scale circulation patterns at the *Curiosity* site, in which northerlies dominate, although Spikes 1 and 5 were detected in different seasons. For Spike 2, the strongest footprint lies over the entire northwestern crater floor (Fig. 2.3d). This is also the case for Spikes 3, 4, 6, and 7 (Fig. 2.S5g, j, p, s), although there are some finer spatial patterns in the footprint map of Spike 6. These five spikes were all detected in the nighttime or in the early morning when the PBL was shallow. The released computational particles are confined within the PBL and only dispersed horizontally; therefore, they imprint almost equally strong footprints over the entire northwestern crater floor. In consequence, a nighttime detection is sensitive to the emission from all the northwestern crater floor.

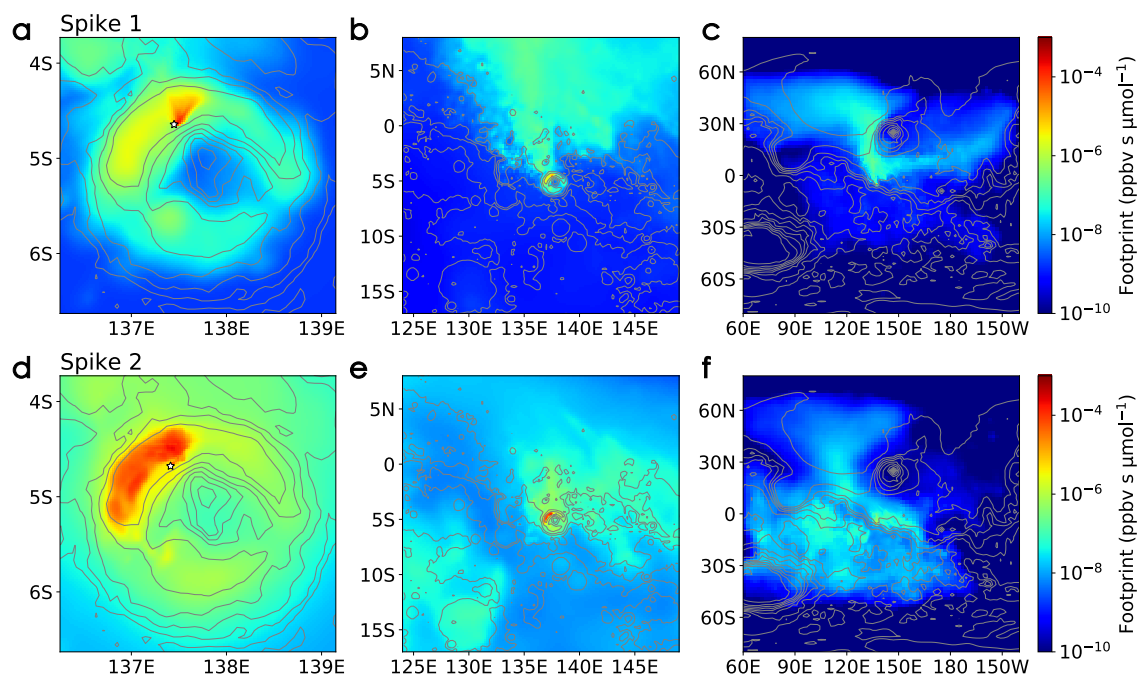


Figure 2.3. Maps of time-integrated STILT footprint, showing the influence of any putative emission site on (a–c) Spike 1 and (d–f) Spike 2. The maps are shown in (a, d) the crater scale, (b, e) the regional scale, and (c, f) the hemispherical scale. The footprint is integrated in putative emission time over a thirty-sol time window prior to a methane measurement. High footprint values indicate upstream regions. The footprint value at any location (a putative emission site) is equal to the prospective TLS methane signal in ppbv above the ~ 0.41 ppbv background after a thirty-sol constant-flux methane emission event with an emission flux of $1 \mu\text{mol s}^{-1}$ occurs at that location. The choice of integrating

over thirty sols is based on the fact that few particles can still imprint footprints after traveling backwards for thirty sols; hence, the maps here show almost all the footprints that can be imprinted, and one can infer almost all the possible upstream regions from these footprint maps. Stars in (a) and (d) mark the positions of *Curiosity*.

Outside Gale crater, the strongest footprint for Spike 1 lies to the north of the crater, as a result of the prevailing regional-scale northerlies in this season (Fig. 2.3b). This is also true for Spike 6 (Fig. 2.S5q). This means that, for these two spikes, if an emission region exists in the neighborhood of Gale crater (but outside the crater), it is most likely located to the north of the crater. The locations of the upstream regions of Spike 2 are, however, less definitive. The strongest footprint of Spike 2 covers the regions in the first and third quadrants of Gale crater (Fig. 2.3e). This is also the case for Spikes 3–5, and 7 (Fig. 2.S5h, k, n, t). Despite this ambiguity, the strongest footprints of all the seven spikes overlap in a region within 300 km to the north of Gale crater. It is noteworthy that the “E8” and “ESE” regions (142–146°E, 2–10°S), suggested as the most likely emission regions for Spike 1 by Giuranna et al. (2019), do not bear high footprint values in our study and are, hence, not identified as the preferred upstream regions for Spike 1 (Fig. 2.3b).

Further zooming out to the hemispherical scale, the high-footprint regions of Spike 1 extend from Elysium Planitia into two directions—one heading for the north along the western side of Elysium Mons to Utopia Planitia, and the other heading for the east along the southern side of Elysium Mons to Amazonis Planitia (Fig. 2.3c). This is also the case for Spike 6, although the northern branch appears more prominent (Fig. 2.S5r). This suggests that among all the distant large-scale geographic units, the aforementioned ones are the most likely to be the emission regions for Spikes 1 and 6. For Spikes 2–5 and 7, the high-footprint regions cover many large-scale geographic units around Gale crater (Fig. 2.3f, Fig. 2.S5i, l, o, u), including the aforementioned Elysium Planitia and Utopia Planitia. It is noteworthy that many thousands of mud-volcano-like structures have been found in Utopia Planitia, which could be methane emission hot spots, according to Oehler & Etiope (2017).

2.4.4 Minimum methane emission

Based on these footprints, the minimum amount of methane emitted from any putative emission site that could give rise to the observed methane spikes can be calculated. The ~ 0.41 ppbv background level from TLS is first subtracted from the seven methane spikes. The remainder of the signals must then be a consequence of recent emission. It is unknown whether the emission was continuous, intermittent, or episodic, but, to put a lower bound on the required methane emission, for each methane spike, we can assume that an instantaneous emission event occurred at the exact moment when a putative emission site had the strongest influence on the methane measurement. Then, for any location (representing a putative emission site), dividing each methane signal (after subtracting the background level) by the maximum footprint value of all putative emission times yields the minimum amount of methane emitted from that putative emission site that would be required to explain the methane signal (Fig. 2.4). Upstream regions, which had the highest footprint values in Fig. 2.3, now bear the smallest values in Fig. 2.4, the latter meaning that they can more easily produce a methane spike. For example, any putative emission site on the northwestern crater floor (the blue region in Fig. 2.4d) is able to produce Spike 2 by emitting only ~ 100 kilograms of methane (refer to the left colorbars in Fig. 2.4). In order to directly compare with the results from TGO, under the assumption that methane is a long-lived species in the atmosphere, this ~ 100 kilograms of methane will result in an increase of $\sim 10^{-5}$ ppbv in the global mean methane concentration (refer to the right colorbars in Fig. 2.4). In comparison, if Spike 2 results from an emission event in Utopia Planitia, at least several millions of kilograms of methane must have been emitted, which would result in an increase of several hundreds of pptv (parts-per-trillion-by-volume, $1 \text{ pptv} = 10^{-3} \text{ ppbv}$) in the global mean methane concentration (Fig. 2.4f). For Spike 1, only a small, fan-shaped area to the north of the *Curiosity* site is able to produce the spike by emitting ~ 100 kilograms of methane (Fig. 2.4a), as a consequence of vigorous mixing in the daytime PBL. Figure 2.S6 in the Supporting Information shows the maps of minimum methane emission for all seven methane spikes.

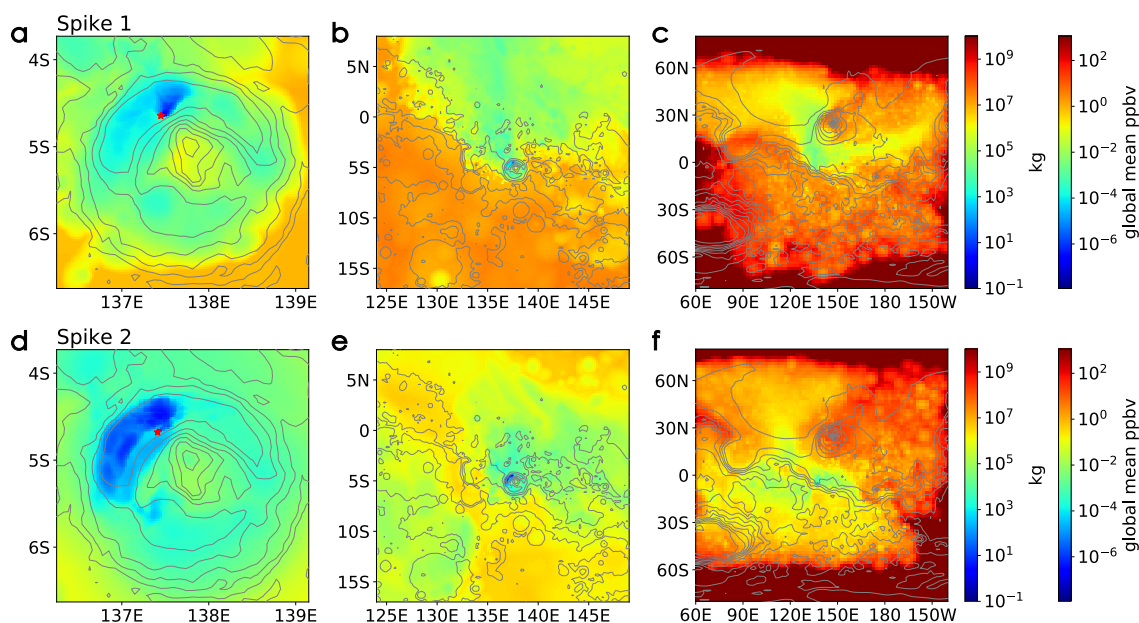


Figure 2.4. The minimum amount of methane emitted from every putative emission location that can produce (a–c) Spike 1 and (d–f) Spike 2. For every putative emission site, an emission event is assumed to occur at the exact moment when the site has the strongest influence on a methane measurement. The left colorbars show the minimum mass of emitted methane as required by the magnitude of the spikes. The right colorbars show the increase in the globally averaged methane concentration after one of the aforementioned smallest emission event occurs. Stars in (a) and (d) mark the positions of *Curiosity*.

The 0.02 ppbv upper limit (Montmessin et al., 2021) of TGO, interpreted as the upper limit on the average methane concentration in the Martian atmosphere, if combined with the 330-year lifetime estimated from standard photochemical models (Lefèvre & Forget, 2009), implies that, on average, no more than 6×10^{-5} ppbv of methane (or ~ 530 kg of methane) is replenished every year. Then, during the 7.1 years of TLS operation, on average, no more than $\sim 4.3 \times 10^{-4}$ ppbv (or ~ 3700 kilograms) could have been emitted into the atmosphere. Assuming the seven methane spikes result from seven emission events, on average, each of them could emit no more than ~ 530 kilograms of methane; otherwise, the methane release would have resulted in a significant and potentially observable rise in the background methane concentration. Only the blue areas in Fig. 2.4 qualify as areas able to produce a methane spike with the observed mole fraction but emitting no more than ~ 530 kilograms of methane (refer to the left colorbars in Fig. 2.4). More quantitative analysis shows that these “qualified areas” are only 1560 km^2 in total, about 8.4% the total area of

Gale crater or 1.1 in 100,000 the total surface area of Mars (Fig. 2.S10). This means that without fast removal mechanisms significantly reducing the methane lifetime, any putative methane emission site responsible for the TLS methane spikes has to be located within the 1560 km² around the *Curiosity* site inside Gale crater. If an emission site has equal chances to reside at any location on the surface of Mars, the probability of it being located within the 1560 km² around the site of *Curiosity* is only 1.1 in 100,000. Despite this low probability, this is the only way that the TLS spikes and the TGO non-detections can be reconciled if one sticks to the ~330-year lifetime of methane. The 1560 km² area is invariably an overestimate, as the assumed situation, where only seven methane emission events occurred during the 7.1 years and all of them were captured by the TLS measurements, is essentially impossible. The actual methane spike frequency at the *Curiosity* site may be much higher, which will put a much lower upper bound on the amount of methane emitted by a single emission event. In that case, the qualified emission regions will be confined within even smaller areas that are very close to the location of the *Curiosity* rover, such as the deep blue areas on the northwestern crater floor in Fig. 2.4. Even for the 1560 km² upper limit of the qualified emission region, this invokes a coincidence that *Curiosity* was sent to the immediate vicinity of a methane emission hotspot, essentially an impossibility.

One possibility that does not invoke this coincidence is that unknown, rapid methane removal mechanisms are at work. If the methane lifetime is shorter than 330 years, more methane can be emitted into the atmosphere per year without perturbing the long-term background methane concentration, and the emission sites will have some freedom to be located at more distant places outside Gale crater, most likely in the upstream regions found in Section 3.3. Figure 2.S10 provides a more quantitative analysis of the required “coincidence” if we accept the results from both TLS and TGO and the 330-year methane lifetime from classical models. To summarize, under the three assumptions: 1. TLS’s methane spikes are real, 2. TGO’s upper limits are real and they represent the upper limit of the methane abundance throughout the Martian atmosphere, and 3. the lifetime of methane is ~330 years, the methane emission site(s) that gave rise to the methane spikes will fall within an area of 1560 km² around the *Curiosity* site in northwestern Gale crater.

Although Gale crater was carefully selected as the landing site for *Curiosity* based on its unique geological context (e.g., Grotzinger et al., 2015), it is still very unlikely that the only methane emission site on Mars resides so close to the site of the rover. Therefore, probably at least one of the three assumptions above needs to be reevaluated. We note that some concerns about contamination by terrestrial methane in the foreoptics chamber and other parts of the TLS instrument have been raised (e.g., Zahnle, 2015), which may have complicated the retrieved *in situ* methane concentrations, but the possibility of measurement bias was ruled out by the TLS team (Webster et al., 2018).

2.4.5 Consecutive methane measurements

More precise emission site identification is possible when we make use of consecutive methane measurements that report a large difference in methane abundances. At $L_s \approx 266^\circ$ in Mars Year 33, two measurements were obtained within a few hours. The first measurement started at $\sim 01:30$ local time and detected a 0.332 ppbv signal, close to the background level. Only a few hours later, the second measurement, at $\sim 06:30$ local time, detected Spike 6 with 5.55 ppbv. One possible explanation for the rapid increase in the ambient methane concentration is that an emission event was initiated between the two measurements. Here, we focus on another possibility that the two measurements were both performed in the midst of an emission event, but a change in the wind direction between the two measurements induced the temporal variability of the methane signals. For any emission event, it would produce a methane signal only if the emission site was located in the upstream region of the detector at the time of emission. Figure 2.5 shows a comparison between the time-integrated footprints for Spike 6 and for the background level. A significant difference can be found between the upstream regions within Gale crater (Fig. 2.5a, d). On the northwestern crater floor, the upstream region of Spike 6, indicated by high footprint values, primarily lies to the west and the southwest of *Curiosity* rover, whereas the upstream region of the background level primarily lies to the northeast of the rover. Therefore, if one assumes the TLS measurements to be correct, the region to the west and the southwest of *Curiosity* in northwestern Gale crater is identified as the preferred methane

emission site for this spike. There are no significant differences between the upstream regions at larger scales (Fig. 2.5b, e, and Fig. 2.5c, f).

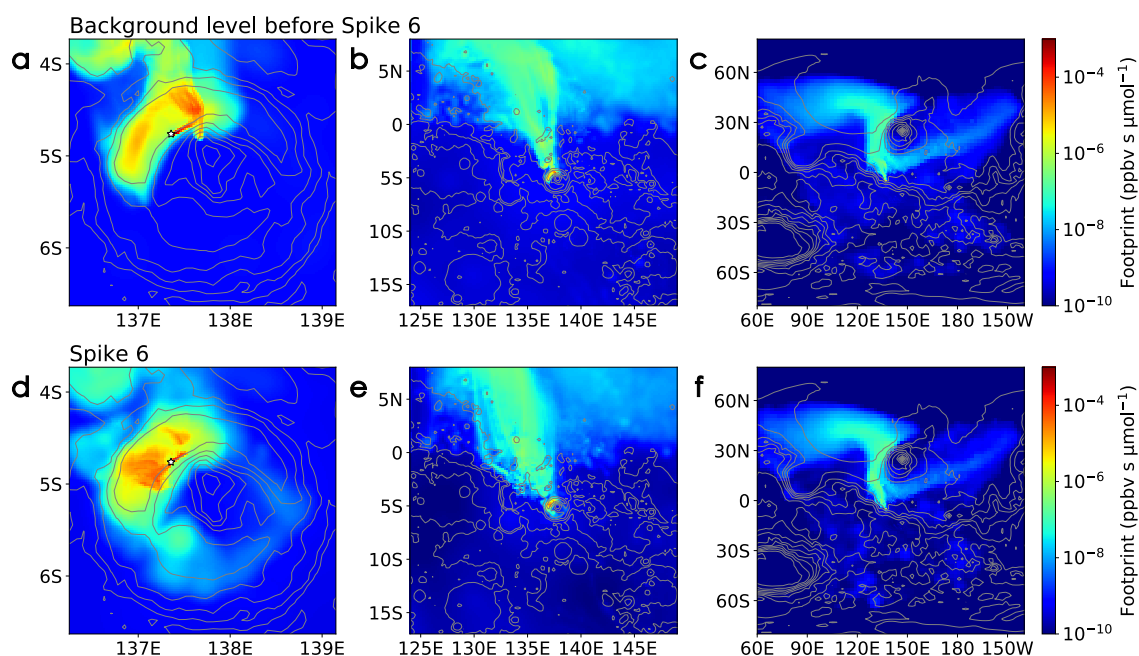


Figure 2.5. Comparison between the footprint maps for a background level and for Spike 6, which were measured on the same sol at $L_s \approx 266^\circ$ in Mars Year 33. Panels (a–c) show the STILT footprint of the background concentration measured at $\sim 01:30$ local time. (d–f) show the STILT footprint of Spike 6, measured at $\sim 06:30$ local time. The stars in (a) and (d) show the positions of *Curiosity*. An emission site with weak influence on the background level and strong influence on Spike 6 would bear a small footprint of the former and a large footprint of the latter. Comparing (a) and (d), regions to the west and the southwest of *Curiosity* on the northwestern crater floor are such sites. The differences between (b) and (e) and between (c) and (f) at the larger scales are smaller than the uncertainty.

We note that this method based on consecutive methane measurements is able to precisely constrain the location of a nearby emission site, but it has high requirements for the measurements. First, the measurements must be consecutively performed within a short period of time, such that the multiple detections have a good chance to be influenced by the same emission event. We have no information about how long a methane emission event on Mars would typically last, but an initial guess for the time period will be at most a few days and optimally a few hours. Second, the measurements must be performed at different times of sol. As currently only “mean” winds representative of their seasons and time of sol can be simulated with a GCM, the winds at the same time of sol on a few

consecutive sols are highly similar, making it difficult to tell the difference between the upstream regions of different measurements. For example, we attempted to apply this method to Spike 7 detected at 03:51 local time on Sol 2442 (after the landing of *Curiosity*) and a background level detected at 01:52 on Sol 2446, but, because these two measurements were both made in the middle of night, no significant difference is found between their upstream regions; hence, this method fails to precisely locate the emission region based on these two measurements. The drop in the measured methane concentration during the four sols is probably due to the cessation of an emission event.

2.5 Conclusions

If we trust the methane abundances detected by both TLS and TGO and accept the 330-year methane lifetime from known photochemistry, our back-trajectory modeling for atmospheric transport strongly supports surface emission sites in the vicinity of the *Curiosity* rover in northwestern Gale crater. This includes the special case that TLS, itself, is the methane source. However, an emission site in northwestern Gale crater invokes a coincidence that we selected a landing site for *Curiosity* so close to an active methane emission site, which is a small probability event. Other possibilities that do not invoke this coincidence include the existence of fast methane removal mechanisms that are unknown to date, false positives of TLS and/or false negatives of TGO. Should future studies confirm the existence of heterogeneous pathways or other unknown photochemical processes for methane destruction, the methane emission sites can be located outside Gale crater, and most likely to the north of the crater.

Our study demonstrates the feasibility and the advantages of applying the inverse Lagrangian modeling technique to emission site identification problems on other planets. The difference between our conclusions about the probable location(s) of the putative emission site(s) and the conclusions in Giuranna et al. (2019) may demonstrate the necessity of small-scale wind simulations and repetitive simulations for removing weather stochasticity. Methane concentration data from future *in situ* measurements, especially

those collected in consecutive measurements performed within a few hours, could further improve the emission site identification.

2.6 Appendix

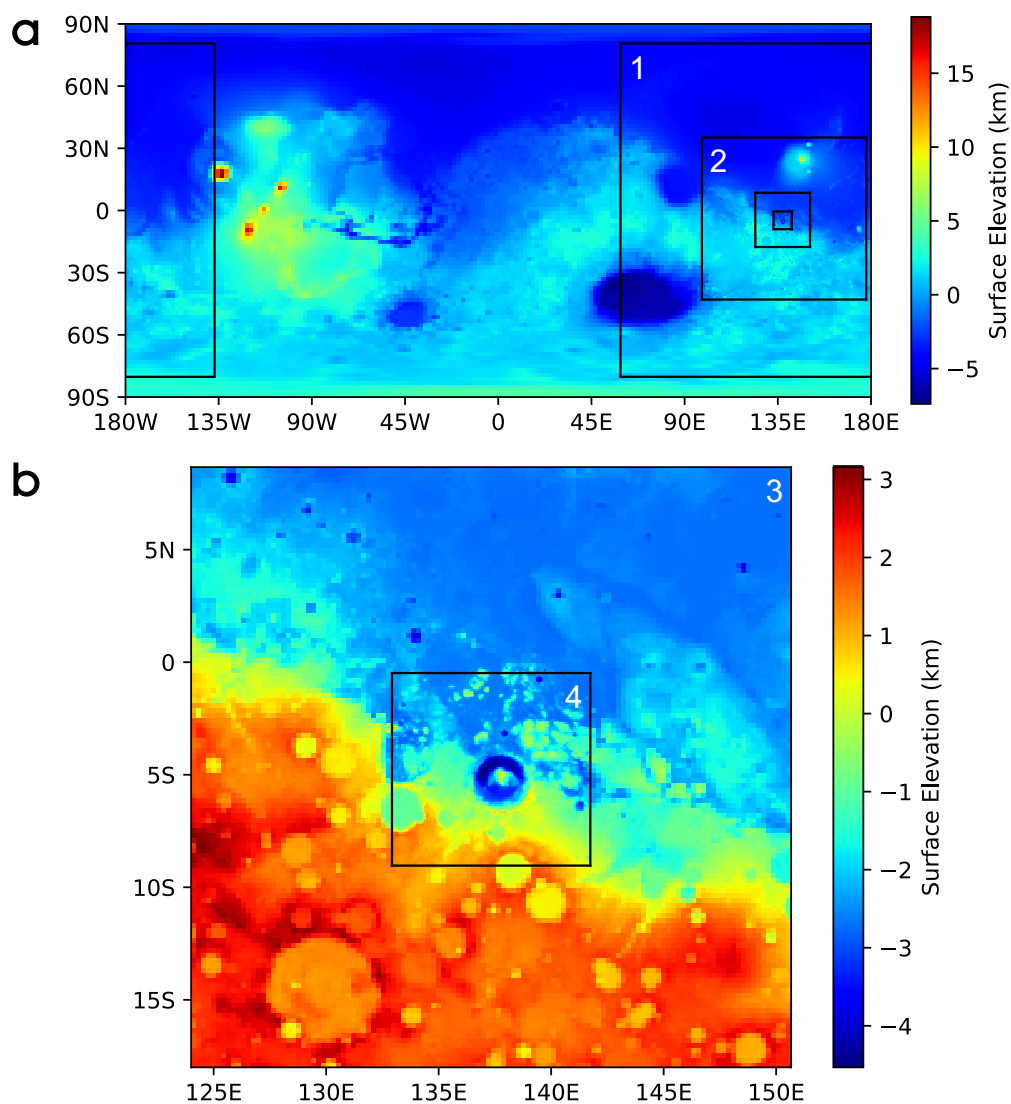


Figure 2.S1. MarsWRF domains on the four nesting levels. (a) Level 1, with a horizontal resolution of $2^\circ \times 2^\circ$ or $118 \text{ km} \times 118 \text{ km}$, and level 2, $0.67^\circ \times 0.67^\circ$ or $39 \text{ km} \times 39 \text{ km}$. (b) Level 3, $0.222^\circ \times 0.222^\circ$ or $13.1 \text{ km} \times 13.1 \text{ km}$, and level 4, $0.074^\circ \times 0.074^\circ$ or $4.4 \text{ km} \times 4.4 \text{ km}$. Colors show surface elevation in the corresponding horizontal resolution of each of the four resolution levels.

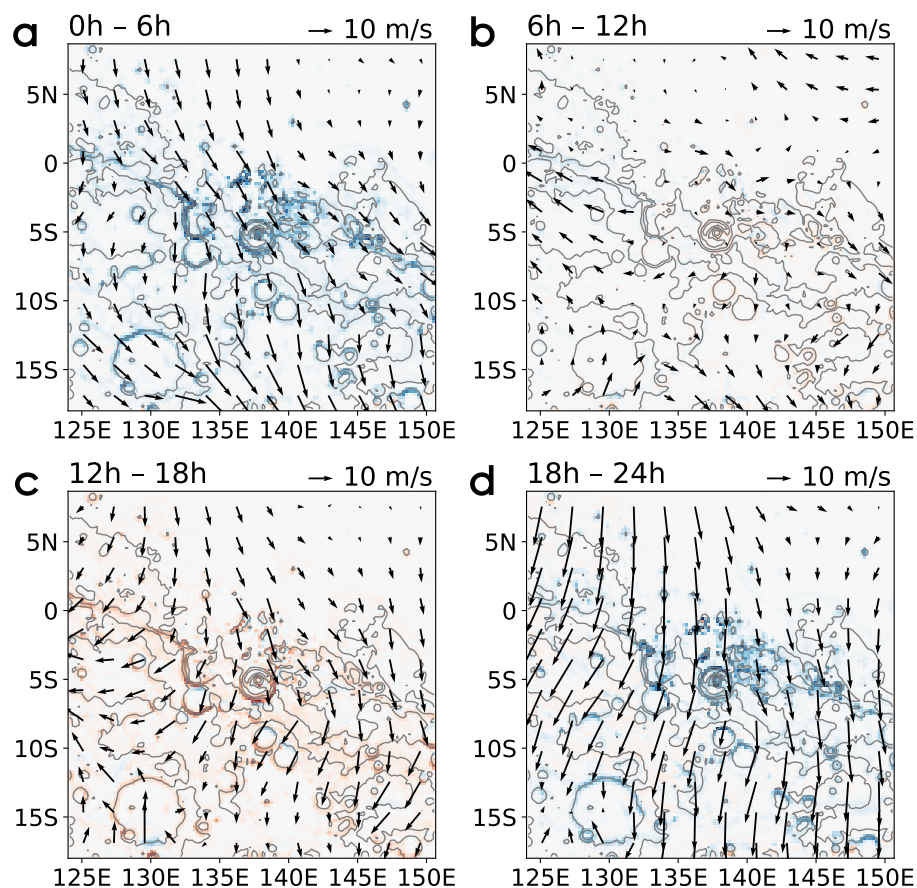


Figure 2.S2. MarsWRF-simulated winds averaged over the lowest 5 km of the atmosphere at $L_s = 336.12^\circ$ (Spike 1). The plotted data is an average over the six hours indicated by the time period on the upper left of each subplot, and also an average over an ensemble of thirty-five sols. Weighted average by air density is performed in the vertical direction. Each arrow shows the horizontal wind averaged over a $131 \text{ km} \times 131 \text{ km}$ square. Red colors show rising air. Blue colors show sinking air. Contours show surface elevation. This figure can be directly compared to Fig. S17 in Giuranna et al. (2019). Between 00:00 and 06:00 local time and between 12:00 and 24:00 local time, the MarsWRF winds and the GEM-Mars winds are similar in directions – both of them are primarily northerly, although the MarsWRF winds are stronger. Between 06:00 and 12:00 local time, the GEM-Mars winds are weak easterlies, which was argued as responsible for transporting methane plumes from the regions to the east and the southeast of Gale crater into Gale itself (Giuranna et al., 2019). The MarsWRF winds in this time period are different. They are weak in general and do not show a dominant wind direction.

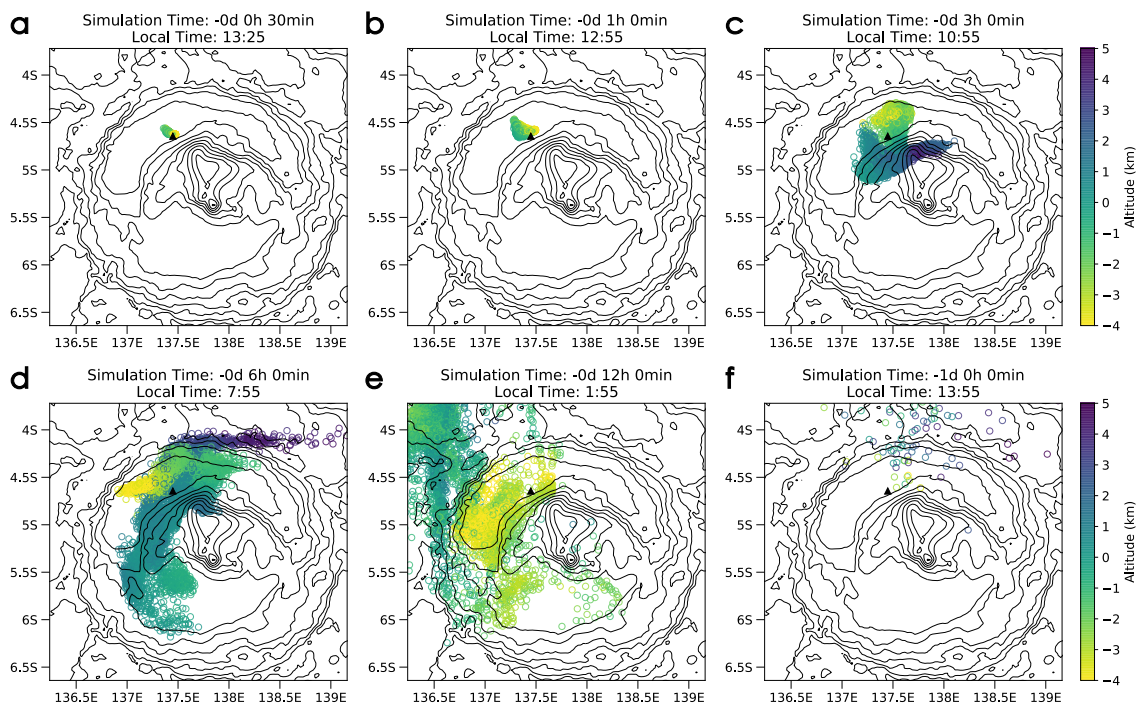


Figure 2.S3. Dispersion of backward-traveling particles within Gale crater (a) thirty minutes, (b) one hour, (c) three hours, (d) six hours, (e) twelve hours, and (f) one sol after particles are released. The STILT simulation is for Spike 1. Each circle shows the position of a single particle. Ten thousand particles are released in the simulation. Colors show the altitude of the particles relative to the Mars datum elevation. Contours show surface elevation. The black triangles mark the position of *Curiosity*. Almost all particles are ventilated out of Gale crater after one sol, indicating an exchange timescale of shorter than one sol, consistent with the findings in Pla-García et al. (2019).

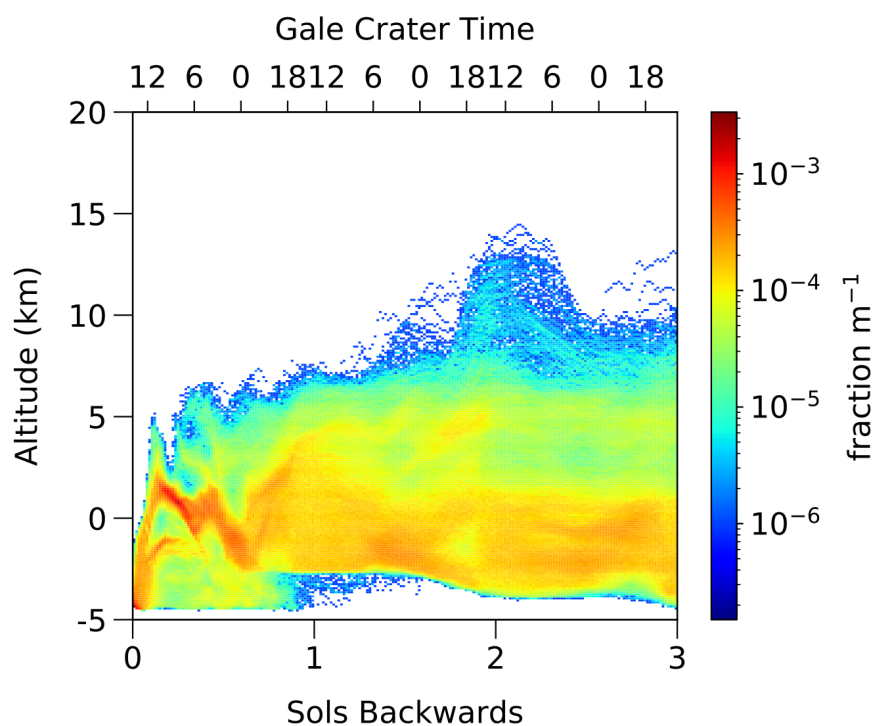
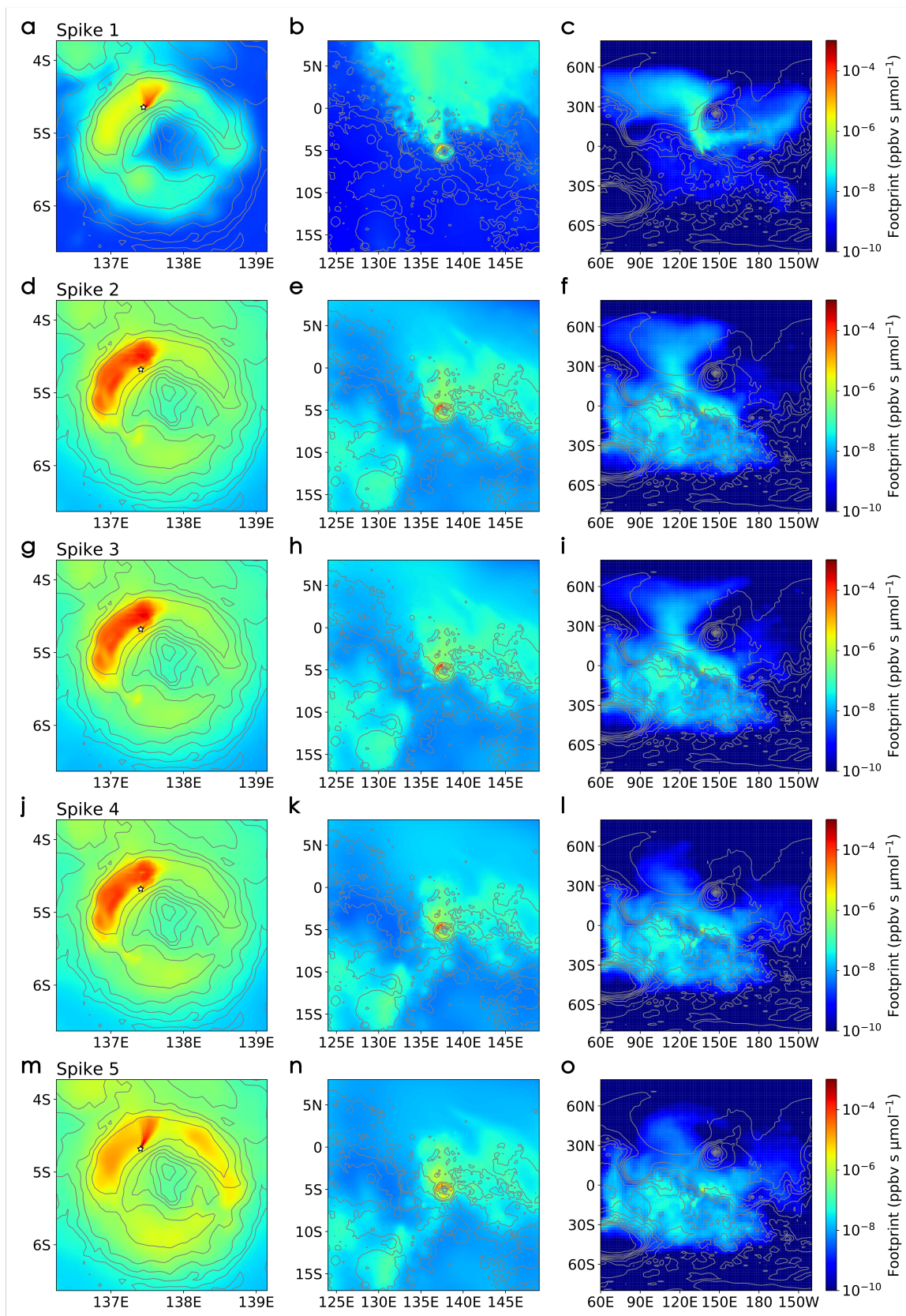


Figure 2.S4. Vertical dispersion of particles in a STILT simulation. An example simulation for Spike 1 is shown. Ten thousand particles are released in the simulation from the lower left corner of the figure. Colors show the fraction of the ten thousand particles with one-meter resolution in the vertical direction, indicating the number density of particles at different altitudes. Note that the particles are also dispersed in the horizontal direction, and almost all of the particles have left Gale crater one sol after the release (refer to Fig. 2.S3). Immediately after the particle release (in the backwards time direction), the majority of the particles climb up the northwestern slope of Mount Sharp, as is shown by the rapid ascent in this figure. This is consistent with the downslope wind along Mount Sharp in the early morning. In the daytime convective PBL, the convection parameterized in STILT randomly redistributes particles in the vertical direction. This results in a nearly homogeneous distribution of particles within the daytime PBL. Three sols after the release, some particles are still in contact with the surface. Extending the simulation out to thirty sols ultimately produces a homogeneous distribution across the lower atmosphere.



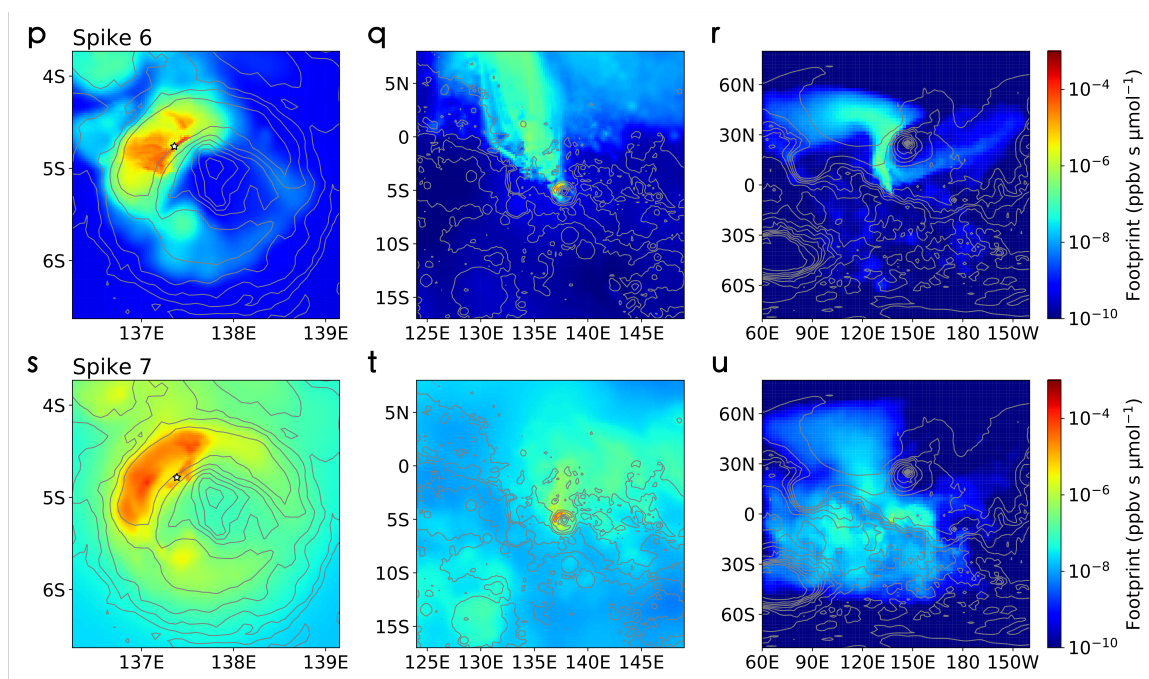
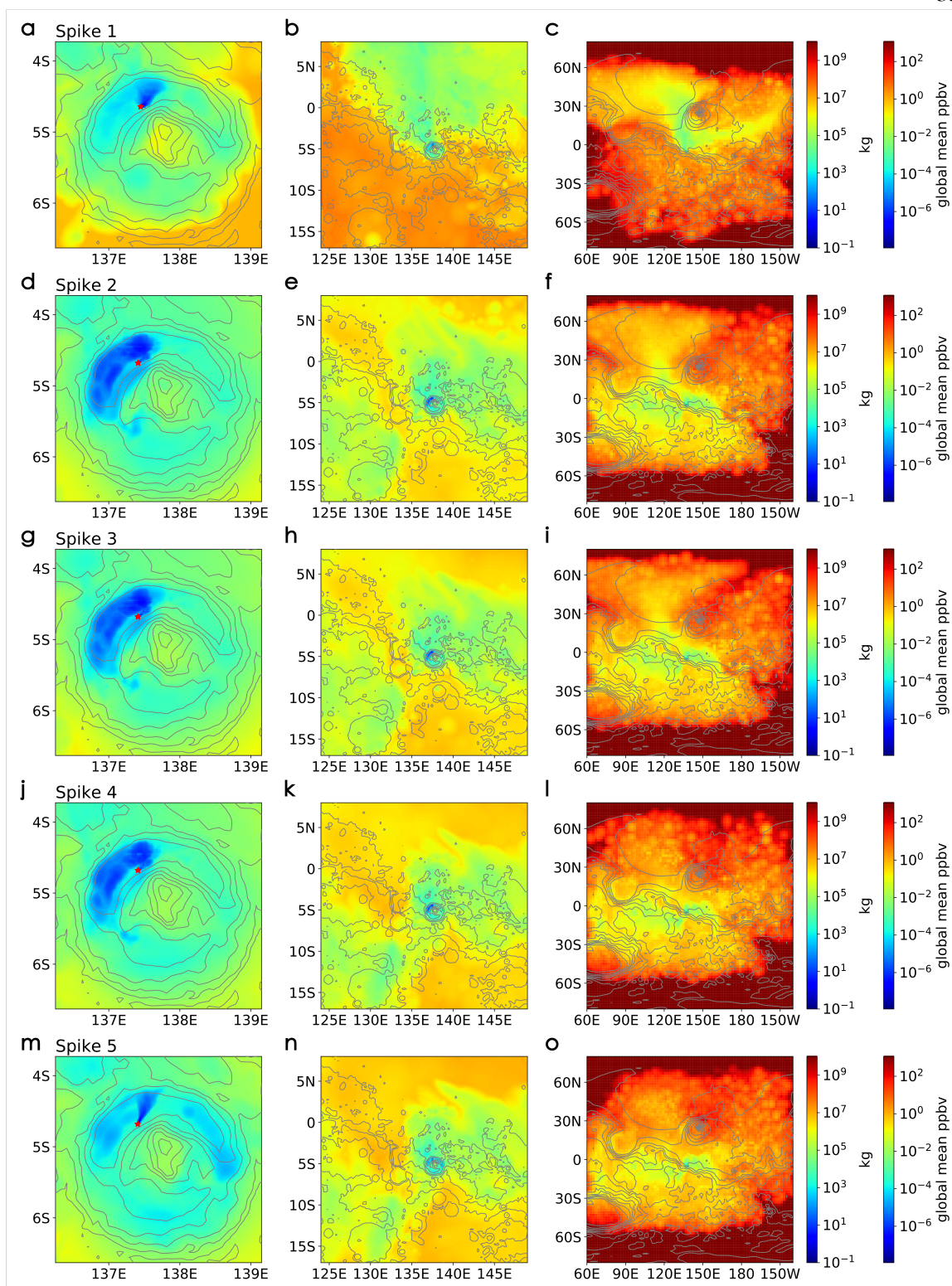


Figure 2.S5. Same as Fig. 2.3, but for all seven methane spikes. Each row shows the footprint maps of one spike at three different scales.



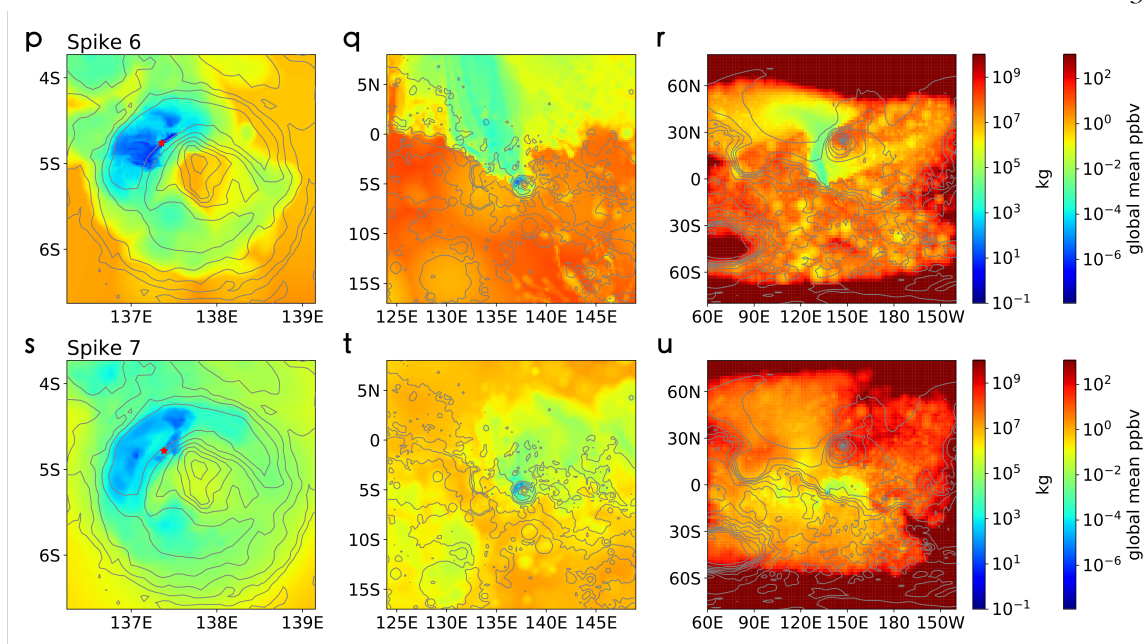


Figure 2.S6. Same as Fig. 2.4, but for all seven methane spikes. Each row shows the minimum emitted mass of methane for one spike.

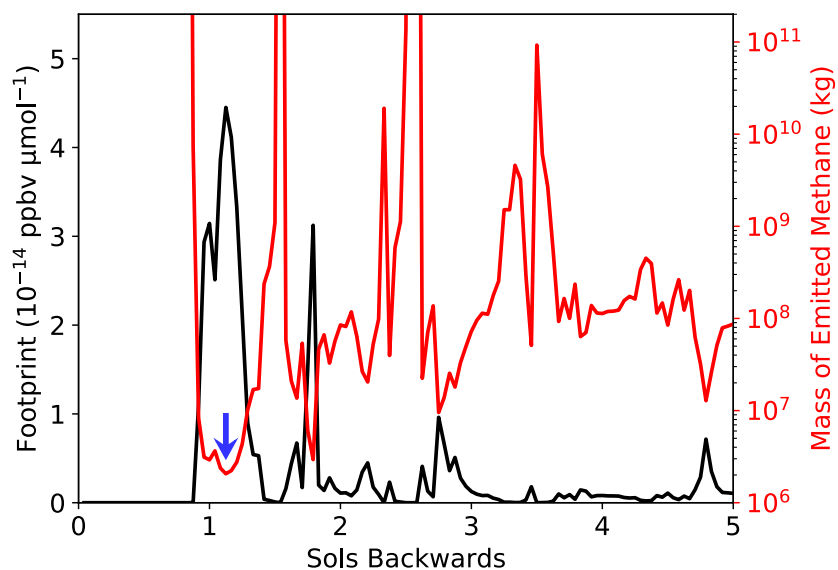


Figure 2.S7. An example time series of the footprint magnitude for Spike 1 at the center of the “E8” region in Giuranna et al. (2019) (4°S , 144°E). The putative emission site is about 390 km away from the *Curiosity* rover. The black curve shows the STILT footprint versus time backwards with respect to the time of detection. The zero footprint within the first twenty hours means that any emission that takes place at this putative emission site less than twenty hours before the detection will not reach the detection site at *Curiosity*. The red curve shows the mass of emitted methane that can give rise to the methane signal,

assuming methane is instantaneously emitted. The blue arrow indicates the moment of maximum influence of the emission site on the methane signal, which corresponds to the smallest required methane emission. To produce Spike 1, this emission site has to emit at least two thousand tons of methane, which is equivalent to 0.23 ppbv global mean methane concentration. If the emission occurred at a random time within five sols before the detection, this figure shows that, in general, 10^4 to 10^5 tons of methane need to be emitted. The emitted mass for the “E8” region found in Giuranna et al. (2019) is 1170 to 2740 tons, which is similar to the lower limit estimated in our work.

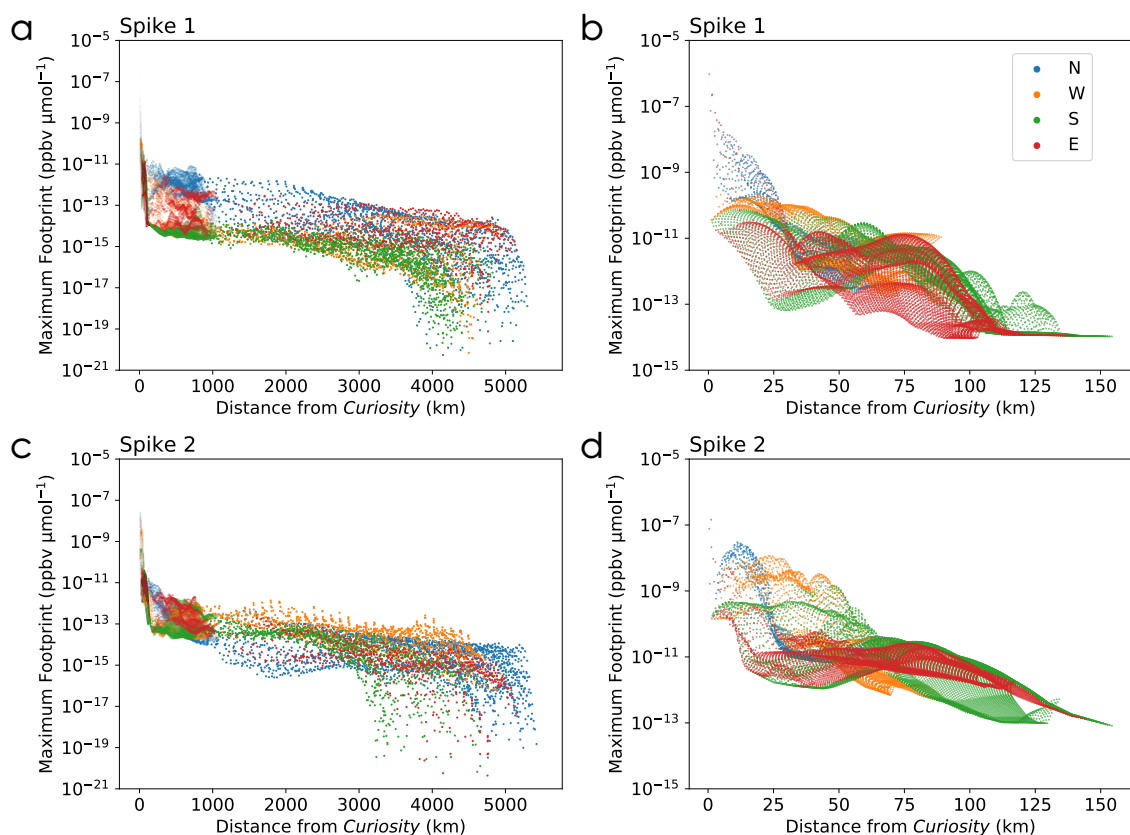


Figure 2.S8. Decay of STILT footprint with distance. Shown is the maximum STILT footprint (a, b) for Spike 1 and (c, d) for Spike 2 at every putative emission site around the detector versus the distance between the emission site and the detector. (a) and (c) show all the putative emission sites in Fig. 2.3(c) and (f). (b) and (d) only show putative emission sites within and in the vicinity of Gale crater. Blue dots indicate emission sites in the northern quadrant, yellow dots, in the western quadrant, green dots, in the southern quadrant, and red dots, in the eastern quadrant. The drop of footprint magnitude at long distances (> 3000 km) in (a) and (c) is due to an insufficient number of particles that reach these distant places in the STILT simulations. It is found that the maximum footprint decays rapidly with distance within Gale crater, whereas outside the crater, the decay is slower. This figure demonstrates of the necessity of modeling atmospheric dispersion when one wants to build a linkage between emission fluxes and methane signals, because the linkage strongly depends on the distance between the emission site and the detector.

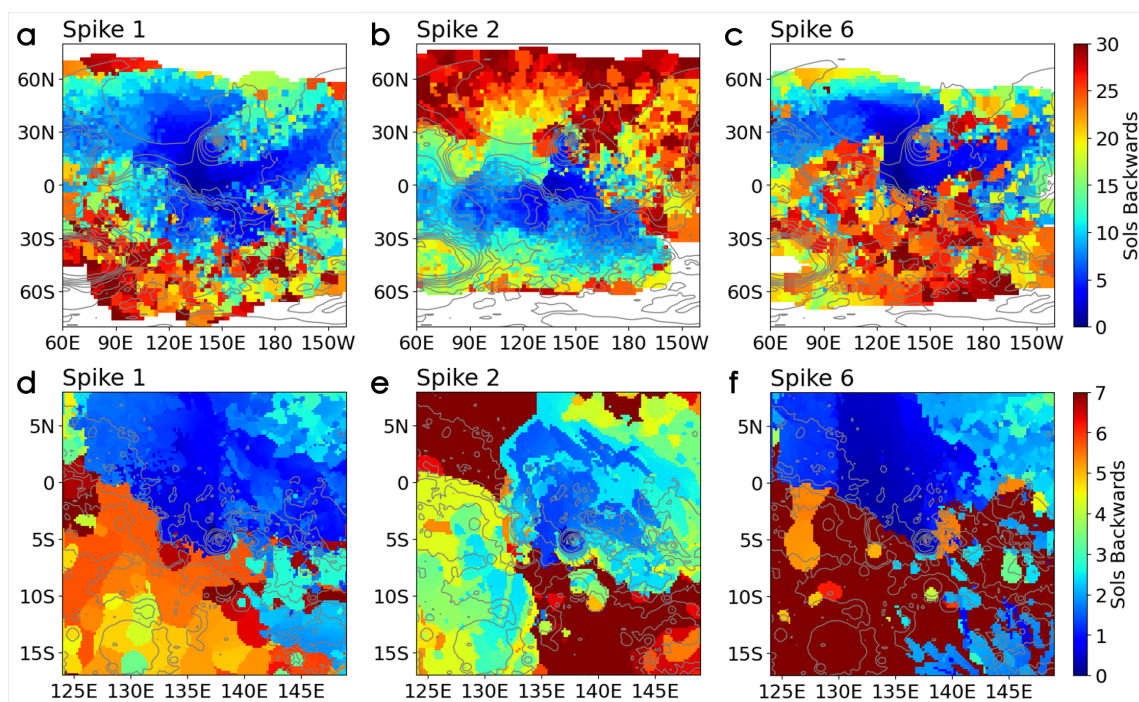


Figure 2.S9. Time of maximum STILT footprint for (a) and (d) Spike 1, (b) and (e) Spike 2, and (c) and (f) Spike 6 at all putative emission sites. One can refer to the blue arrow in Fig. 2.S7 for the meaning of “maximum STILT footprint”. This figure shows the transport timescales. (a–c) show the entire domain of the simulation. (d–f) zoom into the vicinity of Gale crater. It takes less than one sol to transport methane signals emitted from any location within Gale crater to the *Curiosity* rover. For Spikes 1 and 6, it takes less than one week to transport methane signals emitted from Elysium Planitia, Utopia Planitia, and Amazonis Planitia to the detector, whereas it can take a few weeks to more than one month to transport methane signals emitted from the southern highlands to the detector. For Spike 2, it takes about one week to transport methane signals emitted from Hesperia Planum and Terra Cimmeria to the *Curiosity* location, whereas it can take up to a few weeks to transport methane signals emitted from the northern lowlands to the detector. The figures for Spikes 3, 4, 5, and 7 are similar to those for Spike 2.

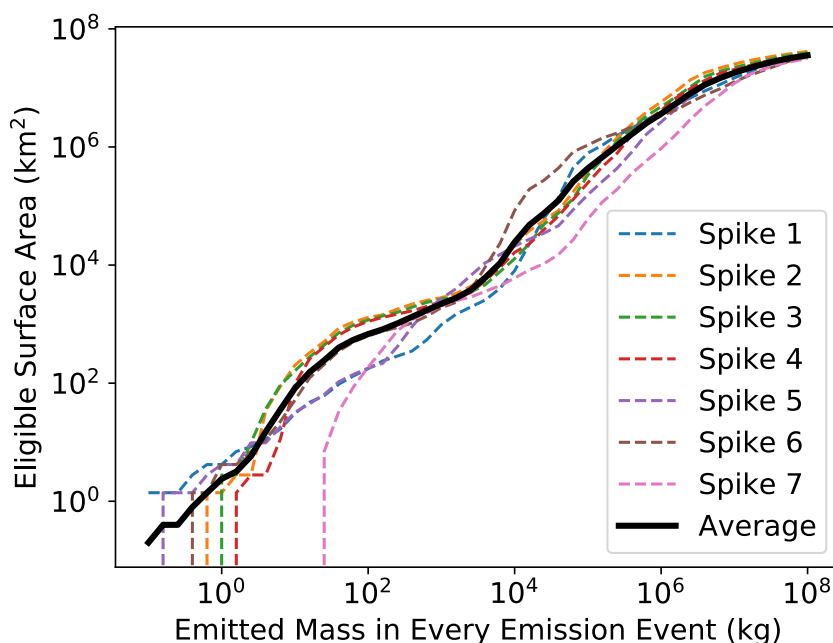


Figure 2.S10. The maximum area of the emission regions where certain amounts of emitted methane can produce the observed methane spikes. Below are two examples intended to guide a reader to interpret this figure. Assuming a putative emission site responsible for the TLS methane spikes only emitted 100 kilograms of methane (which would contribute 1.1×10^{-5} ppbv to the global mean methane concentration) for each spike, then this site must be located within an area of 180 to 1300 km^2 in the vicinity of the *Curiosity* rover. The average over the seven spikes is $\sim 700 \text{ km}^2$, less than 4% of the area of Gale crater and less than 5 in 1,000,000 the surface area of Mars. If we assume a putative emission site emitted 10 tons of methane (which would contribute 1.1×10^{-3} ppbv to the global mean methane concentration) and brought about one of the methane spikes, such emission site must be located within an area of 6000 to 84000 km^2 . The average is $\sim 24000 \text{ km}^2$, about 1.3 times the area of Gale crater and 0.017% of the surface area of Mars. This figure shows the information in Fig. 2.4 and Fig. 2.S6 from another perspective. Recalling that TGO reported an upper limit of 0.02 ppbv for the long-term steady-state methane abundance in the atmosphere assuming methane is a long-lived species, if the lifetime of methane is ~ 330 years as suggested by standard photochemical models, no more than ~ 530 kg of methane is replenished in the atmosphere every year on average. TLS detected seven methane spikes during its first 7.1 Earth years of operation, meaning that no fewer than seven emission events happened during this period of time (and possibly much more than seven). Should the emission events not significantly perturb the long-term steady state methane abundance, on average, no more than ~ 530 kg of methane can be emitted by each emission event. This figure shows that only an area of $\sim 1560 \text{ km}^2$ around the detector (about 8.4% the total area of Gale crater, or 1.1 in 100,000 of the total surface area of Mars) is able to produce an observed methane spike by emitting 530 kg of methane. This quantitatively demonstrates how lucky we may have been to send *Curiosity* to the exact place that is very close to an active surface emission site. Alternatively, there must be fast methane removal mechanisms at work, or either the TLS spikes or the TGO upper limits need to be reevaluated.

Table 2.S1. TLS methane measurements investigated in this study. Adapted from Table S2 in Webster et al. (2018) and Table 2 in Webster et al. (2021).

Name	Solar longitude Ls (degrees)	Local time at Gale crater	<i>In situ</i> methane abundance (ppbv)
Spike 1	336.12	13:55	5.78
Spike 2	55.59	03:22	5.48
Spike 3	59.20	03:22	6.88
Spike 4	72.66	02:53	6.91
Spike 5	81.84	13:26	9.34
Background level before Spike 6	265.78	01:26	0.332
Spike 6	265.91	06:29	5.55
Spike 7	41.5	03:51	20.53
Background level after Spike 7	43.3	01:52	0.211

*Chapter 3***Beyond Steady States: Coupled Atmospheric Chemistry, Radiation and Dynamics of an Exoplanet Produce Self-Sustained Oscillations**

Yangcheng Luo¹, Yongyun Hu², Jun Yang², Michael Zhang¹, Yuk L. Yung¹

¹Division of Geological and Planetary Science, California Institute of Technology,
Pasadena, CA, USA

²Department of Atmospheric and Oceanic Sciences, School of Physics, Peking
University, Beijing, China

3.1 Abstract

Nonlinearity in photochemical systems is known to allow self-sustained oscillations, but they have received little attention in studies of planetary atmospheres. Here, we present a novel, self-oscillatory solution for ozone chemistry of an exoplanet from a numerical simulation with a fully coupled, three-dimensional atmospheric chemistry-radiation-dynamics model. Forced with non-varying stellar insolation and emission flux of nitric oxide (NO), atmospheric ozone abundance oscillates by a factor of thirty over multi-decadal timescales. Such self-oscillations are a novel biosignature because they can only occur with biological nitrogen fixation contributing to NO emissions in our model. The resulting temporal variability in the atmospheric spectrum is potentially observable. Our results underscore the importance of revisiting exoplanets spectroscopically to characterizing their photochemistry and searching for extrasolar biosignature. There are also profound implications for comparative planetology and the evolution of the atmospheres of terrestrial solar-system and extrasolar planets. Fully coupled, three-dimensional atmospheric chemistry-radiation-dynamics models can reveal new phenomena that may not exist in one-dimensional models, and hence they are powerful tools for future planetary atmospheric research.

3.2 Introduction

In photochemical studies of planetary atmospheres, it is generally assumed that if all external forcings, such as insolation and emission rates, are non-varying, any initial value problem can ultimately reach a unique steady state. However, it has been discovered that nonlinearity in photochemical systems can induce complicated dynamical behaviors such as multiple steady states, limit cycle oscillations, and even chaos, in the context of Earth's atmosphere (Prather et al., 1979; White & Dietz, 1984; Kasting & Ackerman, 1985; Stewart, 1995; Krol, 1995; Feigin & Konovalov, 1996; Poppe & Lustfeld, 1996; Hess & Madronich, 1997; Krol & Poppe, 1998; Feigin et al., 1998; Konovalov et al., 1999; Konovalov & Feigin, 2000; Field et al., 2001; Kalachev & Field, 2001; Tinsley & Field, 2001a, 2001b; Hasson & Manor, 2003). For example, with a simplified box model for tropospheric photochemistry,

Field et al. (2001) found a threshold of NO emission flux below which the chemical system evolves towards a unique steady state and above which the system evolves towards a self-sustained oscillatory state. In this paper, we present a self-sustained oscillatory solution for an exoplanetary atmosphere, in which ozone and other atmospheric species undergo large-magnitude periodic oscillations, despite non-varying external forcings, such as emission and stellar insolation.

The simulation is performed using a fully coupled three-dimensional (3D) atmospheric chemistry-radiation-dynamics model. We use the planetary parameters of TRAPPIST-1e, a tidally locked terrestrial exoplanet located in the middle of the habitable zone of a late M dwarf TRAPPIST-1 (Gillon et al., 2017). Previous studies suggested that TRAPPIST-1e more likely hosts liquid water than all its six planetary siblings (Wolf, 2017), so it has become a prioritized target for atmospheric characterization and the search for biosignatures with the James Webb Space Telescope (*JWST*, Barstow & Irwin, 2016; Morley et al., 2017; Batalha et al., 2018) and future telescopes.

As in previous studies of self-oscillations in photochemistry (Stewart, 1995; Krol, 1995; Feigin & Konovalov, 1996; Poppe & Lustfeld, 1996; Hess & Madronich, 1997; Krol & Poppe, 1998; Feigin et al., 1998; Konovalov et al., 1999; Konovalov & Feigin, 2000; Field et al., 2001; Kalachev & Field, 2001; Tinsley & Field, 2001a, 2001b; Hasson & Manor, 2003), we focus on ozone chemistry with destruction pathways catalyzed by HO_x (define as the sum of OH and HO₂) and NO_x (defined as the sum of NO and NO₂). Ozone (O₃) is of particular interest to the chemistry of terrestrial exoplanets and the search for extrasolar biosignatures of photosynthetic life (Segura et al., 2003, 2005), because it is a photochemical product of O₂ and O₂ is product of photosynthesis and the driver for aerobic metabolism (Meadows, 2017; Schwieterman et al., 2018). While O₂ has a few absorption bands in the visible and near-infrared region, O₃ has a much stronger absorption band at 9.6 μm. Because of this, O₃ detection at 9.6 μm is a good proxy for O₂, especially for Proterozoic-like, low-O₂ atmospheres, as ozone abundance, as well as its absorption and emission, decreases only mildly as O₂ abundance decreases by orders of magnitude (Léger et al., 1993; Pollard & Kasting, 2005; Cooke et al., 2022). Moreover, in cloudy atmospheres, surface-emitted,

biogenic trace gases may hide beneath clouds, which mutes their spectral features. By contrast, ozone layers can be more readily observed because they are mainly located in the stratosphere, above any opaque tropospheric clouds.

Transiting exoplanets, such as TRAPPIST-1e, have a favorable feature that their atmospheres can be screened spectroscopically, and then their atmospheric compositions can be deduced from absorption features in the transmission spectrum. To facilitate the interpretation of atmospheric spectra collected in the near future, 1D (in altitude) photochemical models have been employed to study the atmospheric photochemistry of these exoplanets. Possible spectroscopic features in the transmission spectrum have been derived (e.g., O'Malley-James & Kaltenegger, 2017; Krissansen-Totton et al., 2018; Lincowski et al., 2018; Fauchez et al., 2019; Wunderlich et al., 2019). The potential of detecting O₃ has been confirmed (Lustig-Yaeger et al., 2019), but challenges are also evident given the limited signal-to-noise ratio and the lifespan of present telescopes.

Recently, simulations using fully coupled 3D chemistry-radiation-dynamics models have been performed for hypothetical atmospheres of synchronously rotating terrestrial exoplanets with Earth-like background atmospheric compositions (Proedrou & Hocke, 2016; Chen et al., 2018, 2019, 2021; Yates et al., 2020; Braam et al., 2022). Ozone abundances similar to that on Earth have been produced, but the spatial distributions are different – on Earth, there is more ozone at high latitudes, whereas the simulated ozone on tidally locked exoplanets is preferentially distributed over the nightside. Because of the high computational cost of fully coupled 3D atmospheric chemistry-radiation-dynamics simulations, all these simulations are integrated for no more than several decades, so they were unable to reveal any long temporal variabilities in ozone chemistry. In this paper, we report a fully coupled 3D atmospheric chemistry-radiation-dynamics simulation that is integrated for more than seven hundred Earth years to demonstrate the possibility of multi-decadal self-oscillations of ozone abundance on M-dwarf exoplanets. The reported periodic oscillations are not driven by stellar activities (Segura et al., 2010; Chen et al., 2021), seasonal cycles, or atmospheric dynamics (Cohen et al., 2022); instead, they are self-sustained under non-varying external forcings.

3.3 Results

3.3.1 Periodic oscillations of trace gas abundances

In the present simulation, the atmospheric O₂ mixing ratio is 0.01 times the present atmospheric level, which is approximately the O₂ mixing ratio in the Proterozoic Eon (Lyons et al., 2014). The stellar spectrum is a synthesized TRAPPIST-1 spectrum that has a moderate ultraviolet (UV) emission flux (Wilson et al., 2021, see Materials and Methods). The source of nitrogen oxides (NO_x) is mainly a model default surface emission flux of NO, which totals 8 Tg (8×10¹² g) N per Earth year, consistent with reconstructed surface NO emission rates on the pre-industrial Earth (Yienger & Levy, 1995; Lamarque et al., 2010; Bouwman et al., 2022). This emission flux mostly originates from biological nitrogen fixation. There is also a parameterized lightning emission flux (Price & Rind, 1992; Price et al., 1997), which totals about 0.1 Tg N per year (Fig. 3.S1A in Appendix), but it is negligible in the total NO_x source. Detailed information about model setup and experiment design can be found in the Materials and Methods section.

Over more than seven hundred Earth years, the atmospheric abundances of ozone and nitrogen oxides undergo seven cycles, as shown in Fig. 3.1. The average cycle period is about 100 Earth years. The maximum global mean O₃ abundance is up to 360 Dobson Units (DU), and the minimum is down to 10 DU. Meanwhile, NO_x abundance varies between 7×10¹⁷ molecules cm⁻² and 4×10¹⁸ molecules cm⁻². O₃ abundance is well anticorrelated with NO_x abundance if the latter is shifted forward by 20 years. The average O₃ and NO_x abundances are 190 DU and 2.5×10¹⁸ molecules cm⁻², respectively.

Every cycle consists of three stages (Fig. 3.1B). In Stage I, ozone abundance decreases as NO_x abundance increases, requiring more than half a cycle. In Stage II, NO_x abundance decreases by 50–75%, while ozone abundance stays low and fluctuates sometimes. Stage II takes about one fifth of a cycle. In Stage III, the ozone layer is restored while NO_x abundance stays low. Stage III also takes about one fifth of a cycle.

Figures 3.1C and 3.1D show the probability distribution functions (PDFs) and the cumulative distribution functions (CDFs) of O₃ and NO_x abundances over the simulation.

The 10th and the 90th percentiles of ozone abundance are 90 DU and 290 DU, respectively. For NO_x , they are 1.3×10^{18} molecules cm^{-2} and 3.6×10^{18} molecules cm^{-2} , respectively.

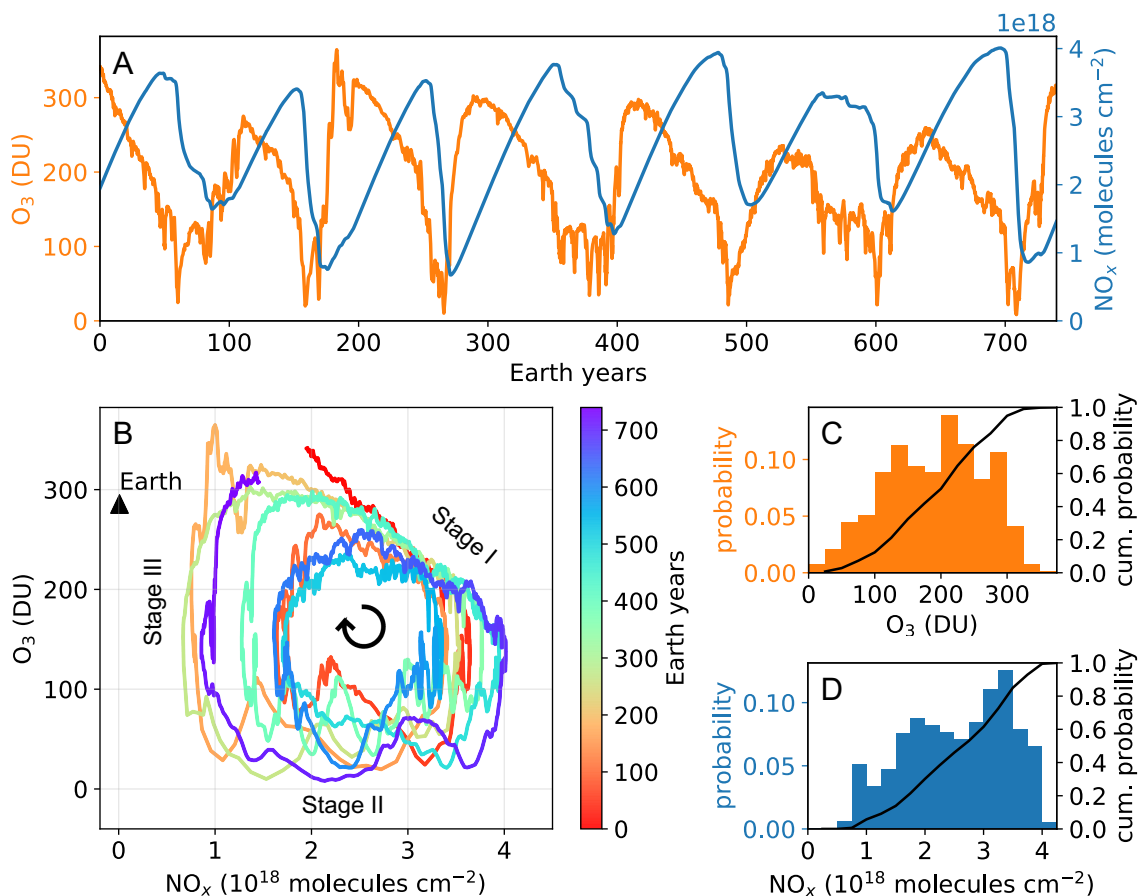


Figure 3.1. Time variability of O_3 and NO_x abundances. (A) Time series of global mean column abundances of O_3 and NO_x . $1 \text{ DU} \approx 2.69 \times 10^{16}$ molecules cm^{-2} . (B) Phase diagram of the system. The horizontal and vertical axes show global mean total column abundances of NO_x and O_3 , respectively. The photochemical state moves clockwise, as indicated by the circle arrow at the center. Colors show model time. The black triangle denotes the state on the pre-industrial Earth, where NO_x abundance is 2–3 orders of magnitude smaller than that in the simulation. (C) and (D) show the PDFs (vertical bars and left axes) and CDFs (curves and right axes) of the O_3 and NO_x abundances, respectively.

3.3.2 Mechanisms behind the self-oscillations

The oscillations in Fig. 3.1 are driven by a negative feedback loop which comprises interactions between photochemistry, radiative transfer, and transport. Figure 3.2 illustrates the key mechanisms.

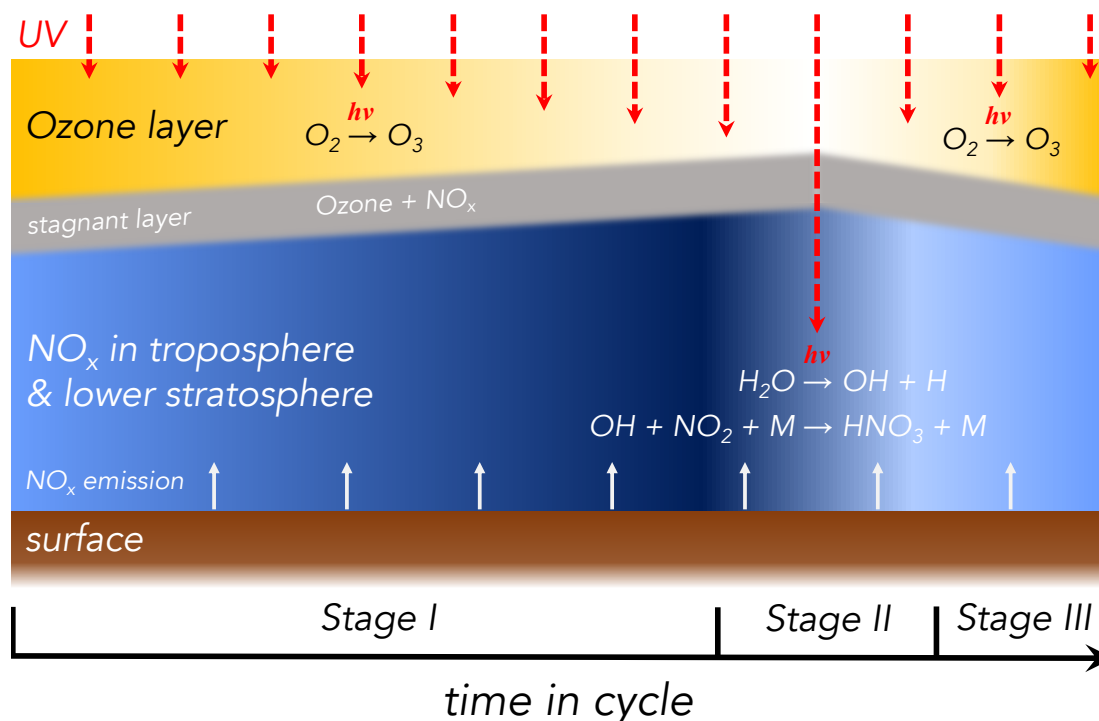


Figure 3.2. A schematic showing key processes in the negative feedback loop that drive the self-oscillations. Change in the red (blue) color denotes change in the concentration of ozone (NO_x).

In Stage I, an ozone layer is present in the middle stratosphere as a result of O_2 photolysis (Fig. 3.3A). Ozone absorbs stellar UV radiation, which warms local air and causes strong thermal inversion at the base of the ozone layer. The strong inversion is characterized by a high Brunt-Väisälä frequency (N), as shown in Fig. 3.3B. This layer of strong inversion is relatively stagnant in vertical motion. Vertical air exchange between the ozone layer above and the levels below is suppressed.

In the meantime, NO_x is emitted into the atmosphere from the surface. On Earth, tropospheric NO_x can be removed by the reaction



where M denotes an air molecule, and the replenishment of OH relies on the photolysis of tropospheric O_3 by UV to produce $\text{O}(^1\text{D})$, followed by $\text{O}(^1\text{D}) + \text{H}_2\text{O} \rightarrow 2\text{OH}$. On the exoplanet (orbiting a cool M dwarf star), however, UV insolation is weak, so tropospheric OH concentration is low and NO_x removal is sluggish. As a result, NO_x steadily accumulates

in the troposphere and in the lower stratosphere, below the aforementioned stagnant layer (Fig. 3.3C). This accumulation of NO_x is similar to the findings in (White & Dietz, 1984; Kasting & Ackerman, 1985).

In the stagnant layer, O_3 is in contact with NO_x from below and is thus consumed, as NO_x is a powerful catalyst for ozone removal through the following reactions



The net reaction is



Thus, the ozone layer is undermined from below, causing its base to retreat upwards. In the meantime, NO_x also slowly diffuses upwards through the stagnant layer and weakens the bulk ozone layer through the same reactions.

As the base of the ozone layer retreats upwards, the stagnant layer moves upwards concomitantly, allowing NO_x to occupy higher altitudes (Fig. 3.3C). Thus, O_3 keeps in contact with NO_x in the stagnant layer, and the base of the ozone layer continues to be destroyed. Eventually, when the NO_x abundance reaches its maximum, ninety percent of the ozone is removed (Fig. 3.3A). The duration of Stage I can be approximated by dividing the increase of NO_x abundance during Stage I by the surface emission flux of NO_x . If the surface emission flux of NO is tripled, the duration of Stage I will decrease from about 75 years to about 40 years (Fig. 3.S6).

The sudden decrease in the ozone abundance at the end of Stage I is induced by a regime change in the stratospheric circulation pattern, which then marks the beginning of Stage II (Fig. 3.4). The stratospheric circulation pattern is determined by the horizontal distribution of ozone, the primary absorbing molecule in the stratosphere. In early to middle Stage I, stratospheric NO_x concentration is low, so the lifetime of ozone is long enough that ozone can be transported by tropical westerlies from the substellar region where it is produced to

the nightside, and ultimately back to the dayside, forming a tropical ozone belt (Fig. 3.4A). The heating by the ozone layer results in a longitudinally quasi-symmetric pattern of the geopotential height (Fig. 3.4C), which then leads to two polar cyclones. NO_x concentration is high in the polar cyclones (mostly at the North Pole due to asymmetry in the land distribution over the two hemispheres) (Fig. 3.4E). The vertical transport of NO_x from lower altitudes to higher altitudes is mainly by ascending air in the substellar region, but as NO_x concentration in the substellar region is low, upward NO_x transport is inefficient.

However, towards the end of Stage I, NO_x concentration in the stratosphere is high enough to reduce the lifetime of ozone below the timescale at which ozone is transported out of the substellar region, so ozone is restricted around the substellar point (Fig. 3.4B). This results in localized heating in the substellar region, which then elevates isobaric surfaces in the substellar region and induces two giant cyclones in the mid-latitudes of the nightside via Rossby waves (Fig. 3.4D). The change in the pattern of atmospheric circulation causes NO_x to be expelled from the polar region and to accumulate outside the nightside mid-latitude cyclones, forming a spindle-shaped distribution (Fig. 3.4F). There is high NO_x concentration in the whole substellar region, making the upward NO_x transport by substellar ascending air very efficient. Large quantities of NO_x rise to the upper stratosphere—where the ozone layer is located—within a short period of time and destroy ozone rapidly, causing a sudden decrease in ozone abundance (Fig. 3.1B), at the time of which Stage I finishes and Stage II starts. Such regime changes in the stratospheric circulation pattern occur multiple times during Stage II and cause the fast oscillations in ozone abundances in Stage II (Fig. 3.1A, 3.1B).

In Stage II, depleted stratospheric ozone allows UV radiation to reach the lower troposphere, leading to rapid photolysis of water vapor and a rapid increase in OH concentration (Fig. 3.3, D and E). Note that this mechanism holds only when the atmospheric O_2 level is low, as high O_2 levels alone would not allow UV to reach the lower troposphere. Then, abundant OH leads to a rapid decline of NO_x through Reaction 1 (Fig. 3.3F), during which time more than half of the NO_x is removed. The product of this reaction, nitric acid (HNO_3), is then scavenged out of the atmosphere by wet deposition (Fig. 3.3G), which

balances NO emission and closes the atmospheric budget of NO_y (defined as $\text{NO} + \text{NO}_2 + \text{NO}_3 + \text{HNO}_3 + \text{HO}_2\text{NO}_2 + 2\text{N}_2\text{O}_5 + \text{ClONO}_2 + \text{BrONO}_2$). The duration of Stage II can be approximated by dividing the decrease of NO_x abundance during Stage II by the integrated reaction rate of Reaction 1 in the troposphere.

In Stage III, the NO_x abundance is at its minimum (Fig. 3.3C), so the catalytic cycle for ozone loss is slow, allowing the stratospheric ozone layer to be restored (Fig. 3.3A). The system then enters the next cycle.

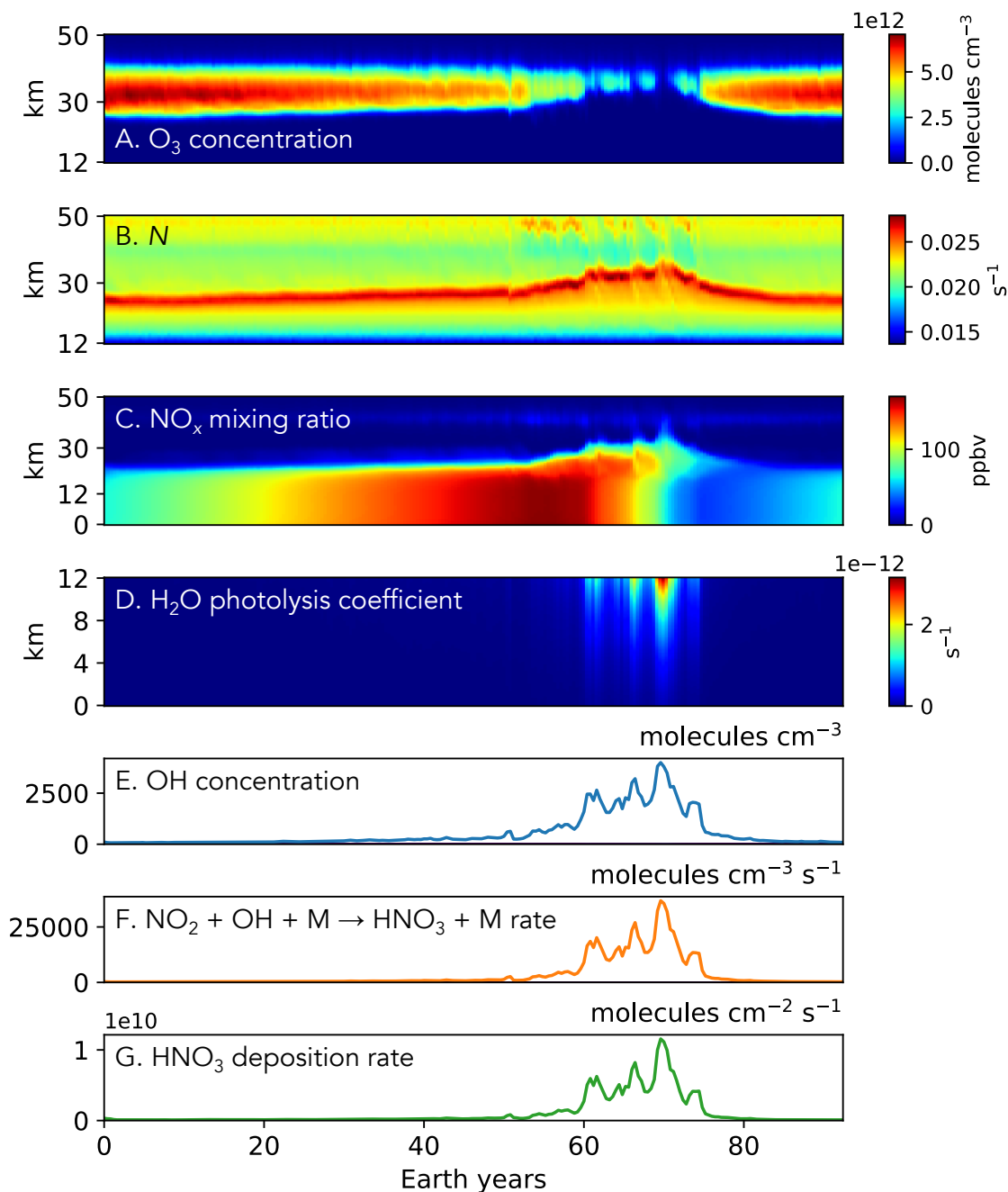


Figure 3.3. Evolution of the self-oscillatory system within a cycle. Panels show time-dependent horizontal mean (A) ozone number density, (B) Brunt-Väisälä frequency N , (C) NO_x mixing ratio in units of parts-per-billion-by-volume (ppbv), (D) the reaction rate coefficient for water vapor photolysis, (E) OH number density at 500 m altitude, (F) reaction rate of $NO_2 + OH + M \rightarrow HNO_3 + M$ at 500 m altitude, and (G) wet deposition rate of HNO_3 . Data are taken from the fourth cycle.

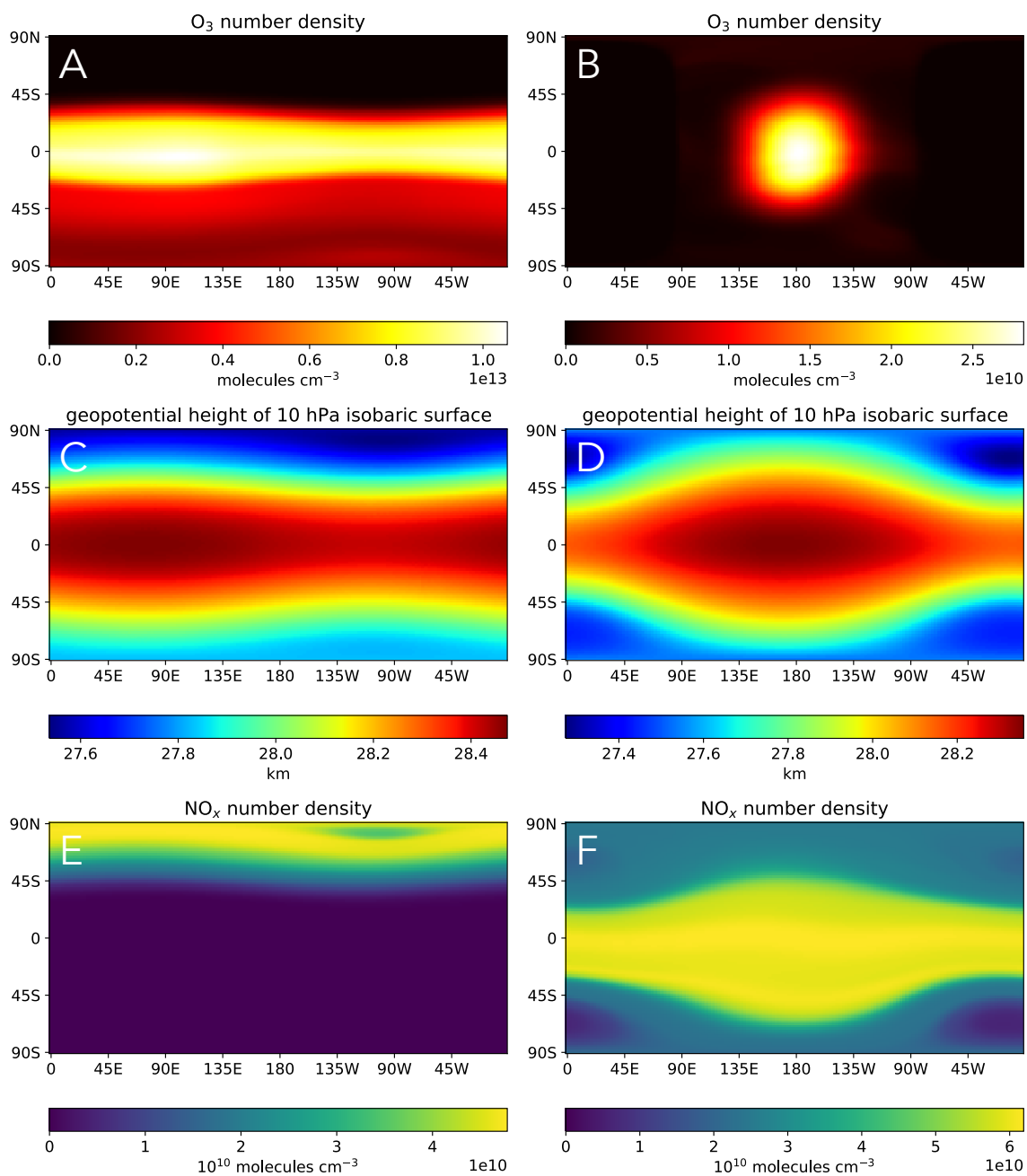


Figure 3.4. Atmospheric dynamics in the stratosphere greatly affects ozone abundance. The first row shows the horizontal distribution of ozone number density in middle stratosphere (10 hPa). Note that panels A and B have different color bars. The second row shows the horizontal distribution of the geopotential height of the 10 hPa isobaric surface. The third row shows the horizontal distribution of the NO_x number density in the middle stratosphere (10 hPa). The left column shows snapshots in early Stage I, when the stratospheric ozone layer is thick. The right column shows snapshots at the onset of Stage II, when the stratospheric ozone layer has been greatly attenuated. The substellar point is located at the center of each panel.

3.3.3 Observational prospects

Both the ozone layer and its variability can be detected by transit spectroscopy (Fig. 3.5). Averaged over the seven cycles and assuming a resolving power $\lambda/\Delta\lambda = 100$, starlight absorption by ozone enhances the transit depth at $9.6 \mu\text{m}$ by 60 parts-per-million (ppm, Fig. 3.5, A and C). Detection of this signal will be challenging for *JWST* (Lustig-Yaeger et al., 2019), but is possible for future instruments dedicated for atmospheric characterization of transiting exoplanets. Figures 3.5B and 3.5D show the temporal variability of the transit depths. The strongest variability takes place at the wings of the $9.6 \mu\text{m}$ ozone absorption band. At $9.82 \mu\text{m}$, the variability is up to 50 ppm. The variability is small at the center of the ozone absorption band due to line saturation.

The PDF and the CDF of the transit depth at $9.82 \mu\text{m}$ are shown in Fig. 3.5E. Despite the symmetry in the PDF of the ozone abundance in Fig. 3.1C, the distribution of the transit depth is left-skewed because of line saturation at high ozone abundance. The 10th and the 90th percentiles are 25 ppm and 47 ppm, respectively. The variability of NO_x absorption features is hardly detectable. A clear-sky condition is assumed in the transit depth calculations presented above. Refer to Figs. 3.S3 and 3.S4 in the Appendix for the effect of cloud on the transit depth calculations.

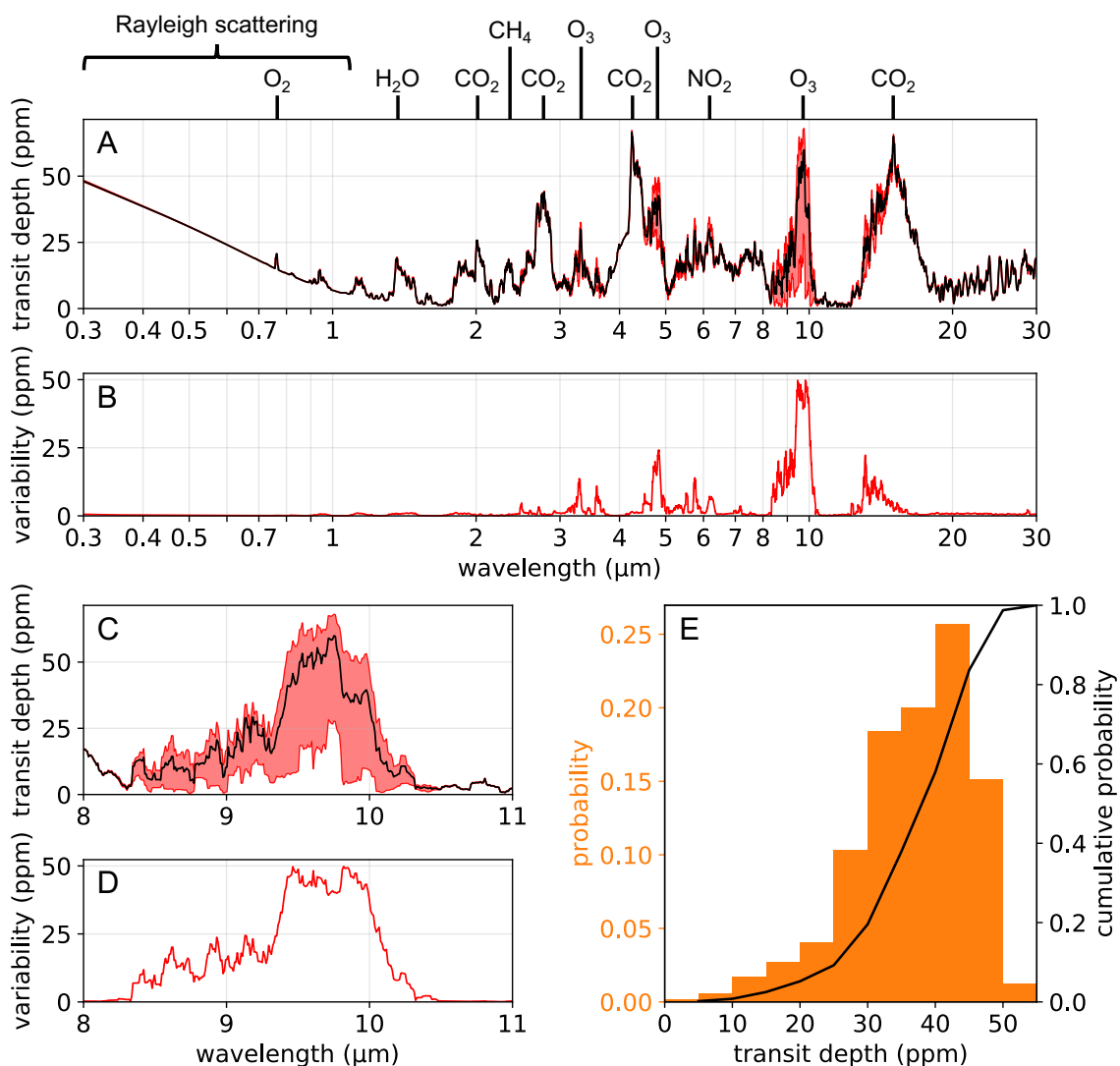


Figure 3.5. Detectability of the ozone layer and its variability. (A) Wavelength-dependent transit depth of the atmosphere. The black curve shows the time mean transit depth. The red shading shows the range of transit depths over the entire simulation. A moving average with a resolving power of 100 (the resolving power of *JWST*'s low-resolution spectroscopy) is applied. (B) Variability in the transit depth (maximum minus minimum) over the seven cycles. (C) and (D) are the same as (A) and (B), but in the vicinity of the 9.6 μm ozone absorption band. (E) The PDF (vertical bars and left axis) and CDF (curve and right axis) of the transit depth at 9.82 μm .

3.4 Discussion

Our results show that large-magnitude self-sustained oscillations in atmospheric chemistry can exist on exoplanets, which may induce significant temporal variability in transmission spectra of exoplanetary atmospheres. Such variability could be detected by

future observations that revisit atmospheric spectra of exoplanets over long periods of time. Although a complete cycle may be too long to observe, steady trends in ozone abundance, such as the decreasing trend in Stage I and the increasing trend in Stage III, if observed, could also suggest the possible presence of such oscillations.

From the mechanisms behind the self-oscillations, we can infer that without the surface NO_x emission, which mainly originates from biological nitrogen fixation, the self-oscillations would not occur (Fig. 3.S6). This is consistent with previous findings that tropospheric photochemical systems produce self-oscillations only if the NO emission flux exceeds a certain threshold (Field et al., 2001). Therefore, the temporal variability in ozone abundance reported in this paper, which is characterized by its large magnitude and slowness, is a biosignature, because they could suggest the presence of a strong NO_x source that is probably biological. This novel class of biosignature is intrinsically different from the conventional ideas of oscillations of atmospheric gases being biosignatures (Schwieterman et al., 2018) which arise from the non-uniform spatial distribution of a biosphere and the seasonality in insolation conditions. By contrast, the self-oscillations in this paper do not rely on either of the two conditions, and their period can be completely unrelated to the orbital period. The variabilities reported in this paper can also be distinguished from those induced by atmospheric dynamics (Cohen et al., 2022) and those induced by cloud dynamics (Song & Yang, 2021), as the latter two usually happen on shorter timescales and have smaller magnitudes.

It is worth noting that box models of simplified photochemical systems for the Earth's troposphere have shown that for a similar kind of self-oscillations, their oscillation period depends on model parameters (Krol & Poppe, 1998). In our model, the UV flux from the host star, the oxygen level in the planetary atmosphere, the water vapor supply, the NO_x emission rate, and other model parameters, could all potentially affect the oscillation properties such as magnitude and period, or determine whether self-oscillations can exist at all. Because of the computational cost of fully coupled, 3D atmospheric chemistry-radiation-dynamics simulations, a systematic exploration over the parameter space will be left for future work.

Oscillations in photochemical systems akin to those in this paper could also have induced the observed variabilities on solar-system planets (Marcq et al., 2013) and exoplanets (Rappaport et al., 2012; Barragán et al., 2018; Tamburo et al., 2018; Meier Valdés et al., 2022), although the nature of the oscillations can be completely different in different planetary contexts.

3.5 Materials and Methods

3.5.1 Fully coupled 3D atmospheric chemistry-radiation-dynamics simulations

The model used here is CESM-WACCM (Neale et al., 2012). CESM (Community Earth System Model, version 1.2.2) is a fully-coupled, community, global climate model that includes interactions of atmosphere, land, ocean, and sea ice, etc. WACCM (Whole Atmosphere Community Climate Model, version 4.0) serves as its atmosphere component. WACCM has fully coupled, 3D atmospheric dynamics, photochemistry, and radiative transfer, and has been extensively used to simulate ozone chemistry in the Earth's atmosphere (Marsh et al., 2013). With the top layer extending to about 6×10^{-4} Pa, WACCM fully resolves the stratosphere. The photochemistry component of WACCM is the MOZART (Modules for Ozone and Related Chemical Tracers) chemical transport model (version 4) (Emmons et al., 2010). It has 57 atmospheric species including neutral and ion constituents, and one inert atmospheric species (N_2). These species are linked by 74 photolytic and ionization reactions, 143 gas phase reactions, and 17 heterogeneous reactions on aerosol particles. The model resolves the full ozone chemistry by simulating all major reactions involving O_x (defined as $O_x = O_3 + O$), HO_x , NO_x , ClO_x (defined as $Cl + ClO$), and BrO_x (defined as $Br + BrO$). Nitrogen chemistry involving all NO_y species is also resolved.

We assume a pre-industrial chemical scenario in which only HO_x and NO_x are important catalysts for ozone loss. For boundary conditions, the model prescribes volume mixing ratios of O , O_2 , H , H_2 , N , NO , CO , and CO_2 at the upper boundary (model top), and volume mixing ratios of H_2 , CH_4 , CH_3Cl , CH_3Br , N_2O , and CO_2 at the lower boundary (surface). Emission in the model includes surface fluxes of NO , $HCHO$, and CO , and a lightning flux of NO . The model default surface emission flux of NO is 8 Tg N per year. We also perform a simulation

with a tripled surface NO flux. The simulated lightning emission of NO is about two orders of magnitude smaller than that on Earth due to the low O₂ level and tidal locking, the latter confining lightning flashes within the substellar region. For deposition, there are dry depositions of O₃, H₂O₂, NO₂, HNO₃, HO₂NO₂, CH₃OOH, HCHO, and CO, and wet depositions of H₂O₂, HNO₃, HO₂NO₂, HCl, HOCl, ClONO₂, HOBr, HBr, BrONO₂, CH₃OOH, and HCHO.

For other components of CESM, the land component used here is the diagnostic version of the Community Land Model (CLM), and the ocean component has fixed sea surface temperature and fixed sea ice distribution. The sea surface temperature and sea ice distribution are taken from one simulation for TRAPPIST-1e with 400 parts-per-million-by-volume (ppmv) CO₂ (Wolf, 2017; Fig. 3.S5 in Appendix). Sea ice temperature is calculated. The Earth's land-sea distribution and topography are used in the simulation.

The substellar point is fixed at 0°N, 180°E. The rotation period is set to 6.1 Earth days. The orbital eccentricity and obliquity are set to zero. The background atmosphere is composed of 99.79% N₂ and 0.21% O₂. To account for the low O₂ concentration, we scaled the NO emission flux from lightning by a factor of 0.103, a value obtained from thermodynamic equilibrium. The mean molecular weight of dry air is set to 28.128 g mol⁻¹. For simplicity, we use Earth's radius and surface gravity to approximate those of TRAPPIST-1e. The quasi-biennial oscillation (QBO) forcing in WACCM, which is a momentum forcing in the tropical stratosphere, is turned off. CO₂ concentration is set to 400 ppmv. The seasonality in all boundary conditions, including those on volume mixing ratios and those on emission fluxes, is smoothed out.

3.5.2 Stellar spectrum

The stellar spectrum used here is from the Mega-MUSCLES Treasury Survey (Wilson et al., 2021, Fig. 3.6). It was produced by synthesizing observations from the NASA Hubble Space Telescope (HST) and XMM-Newton and simulations using stellar models for the photosphere, chromosphere, transition region, and corona. The wavelength ranges of particular importance to photochemistry, i.e., far-UV (120–170 nm) and near-UV (170–320

nm), are primarily determined from measurements by the Cosmic Origins Spectrograph on board HST, with data gaps between 210 nm and 280 nm filled by interpolation. The spectrum is scaled to reproduce the total incident radiative energy flux at TRAPPIST-1e— 879.2 W m^{-2} . In far-UV, the simulated exoplanet receives seven times more radiative energy than Earth, whereas in near-UV, it receives only 0.03% of the radiative energy received by Earth.

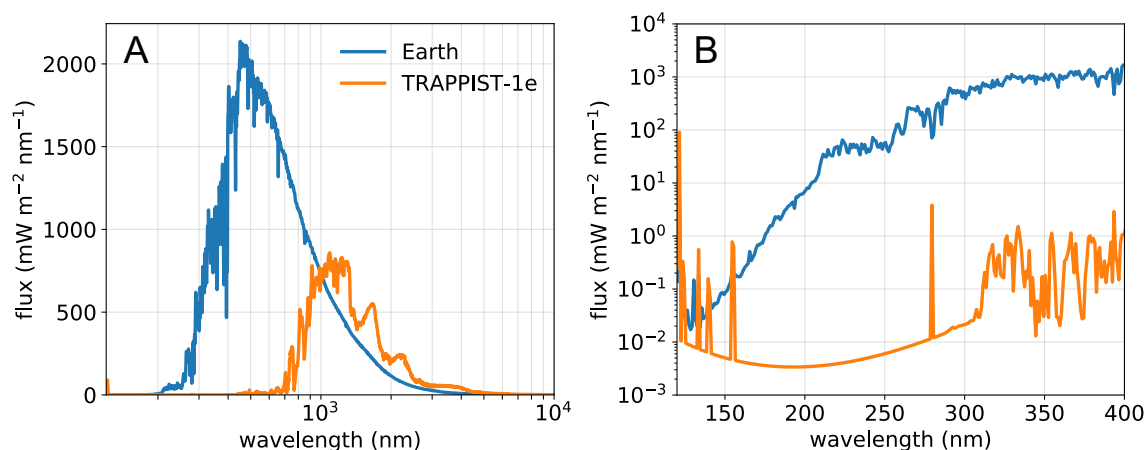


Figure 3.6. The M-dwarf stellar spectrum used in the simulation, in comparison to the solar spectrum. (A) Panchromatic and (B) UV spectra of the incoming stellar radiation at the top of the atmospheres of Earth (blue curve) and TRAPPIST-1e (orange curve). The emission lines in (B) include H I ($\text{Ly}\alpha$), N V, C II, Si IV, C IV, Mg II, and Ca II lines (Wilson et al., 2021).

3.5.3 Calculation of the transmission spectra

The transmission spectra are calculated using Exo-Transmit (Kempton et al., 2017). Users need to specify planetary and stellar radii, a planet's surface gravity, a temperature-pressure profile of the atmosphere, and concentration-pressure profiles for a variety of atmospheric species. In the transmission spectrum calculation, we set the planetary radius to 5798 km, the radius of TRAPPIST-1e, and set the stellar radius to 82930 km, the radius of TRAPPIST-1. The surface gravity of the planet is set to 9.8 m s^{-2} . We include 16 species— CH_4 , CO , CO_2 , H, HCl, H_2 , H_2CO , H_2O , N, N_2 , NO_2 , NO, O, O_2 , O_3 , and OH. Exo-Transmit then finds atmospheric opacity by interpolating between single-molecule cross section data for CH_4 , CO , CO_2 , HCl, H_2CO , H_2O , N_2 , NO_2 , NO, O_2 , O_3 , and OH between a predefined temperature-pressure grid (temperature ranging from 100 K to 3000 K with a spacing of 100

K, pressure ranging from 10^{-4} Pa to 10^8 Pa with a spacing of one order of magnitude) and collision-induced-absorption opacity data for $\text{CH}_4\text{-CH}_4$, $\text{CO}_2\text{-CO}_2$, $\text{H}_2\text{-H}_2$, $\text{H}_2\text{-H}$, $\text{H}_2\text{-CH}_4$, $\text{N}_2\text{-CH}_4$, $\text{N}_2\text{-H}_2$, $\text{N}_2\text{-N}_2$, $\text{O}_2\text{-CO}_2$, $\text{O}_2\text{-N}_2$, and $\text{O}_2\text{-O}$ between the same temperature grid, solve the radiative transfer equation using opacity sampling at a resolving power of 1000, and generates wavelength-dependent transit depths. The wavelength range is between 300 nm and 30 μm . Exo-Transmit considers the oblique path of light through the planetary atmosphere along a distant observer's line of sight. It also accounts for opacity caused by Rayleigh scattering. All opacity data in Exo-Transmit are taken from (Freedman et al., 2008, 2014; Lupu et al., 2014).

We carry out Exo-Transmit calculations for 10^{-3} to 10^5 Pa of the modelled atmosphere. To account for 3D effects, we calculate a spectrum for every latitude on the terminator of the planet and average all output transmission spectra. To account for potential cloud effects that mute molecular absorption features, we also carry out calculations with an optically thick cloud deck at 100 hPa (Figs. 3.S3, 3.S4 in Appendix). One can find the lower bound of the transit depths in these cloudy scenarios.

3.6 Appendix

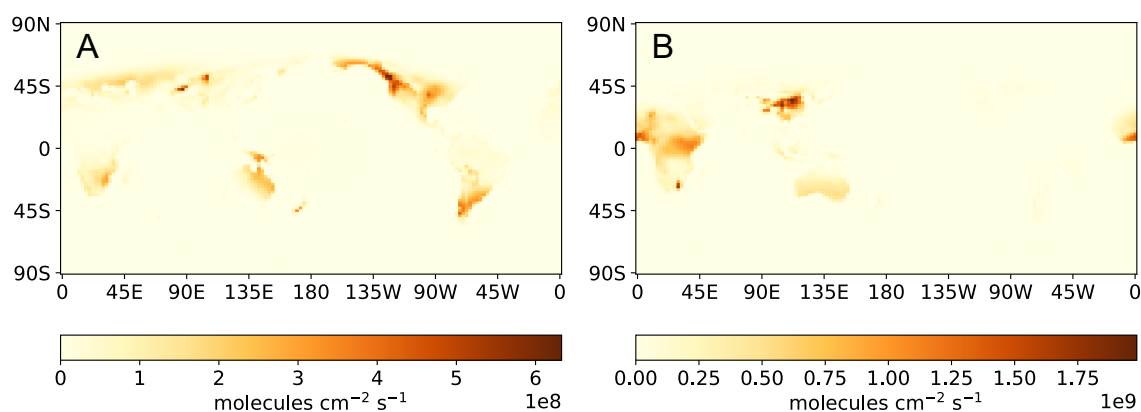


Figure 3.S1. Lightning emission of NO depends on the location of the substellar point. Column-integrated NO production rates from lightning with the substellar point fixed at (A) 0°N , 180°E and (B) 0°N , 0°E . The globally integrated NO production rate from lightning is 0.06 Tg N per year for (A) and 0.16 Tg N per year for (B).

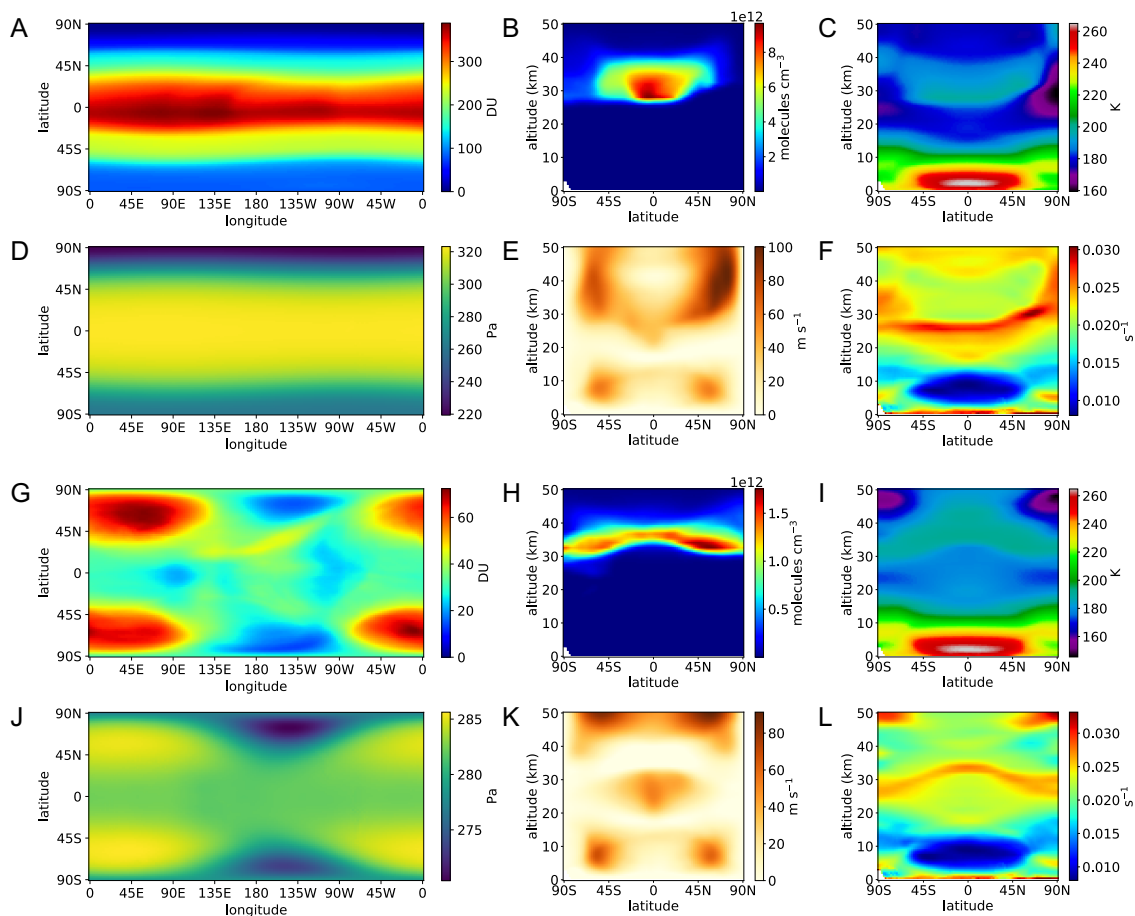


Figure 3.S2. Spatial distributions of ozone and some important atmospheric variables in different stages of the oscillations. Panels (A–F) show a representative time step in Stage I, when the ozone layer is stable. The global mean O₃ column abundance is 248 DU. (A) O₃ column abundance distribution. (B) Zonal mean O₃ number density. (C) Zonal mean atmospheric temperature. (D) Atmospheric pressure at 35 km altitude. (E) Zonal mean zonal wind speed. Positive values indicate eastward wind. (F) Zonal mean Brunt–Väisälä frequency. High values indicate strong convective stability and imply suppressed vertical mixing. Panels (G–L) show a time step when the ozone layer is unstable. The global mean O₃ column abundance is 37 DU. Patterns in panels (G–L) occasionally emerge in Stages II and III. The substellar point is located at 0°N, 180°E.

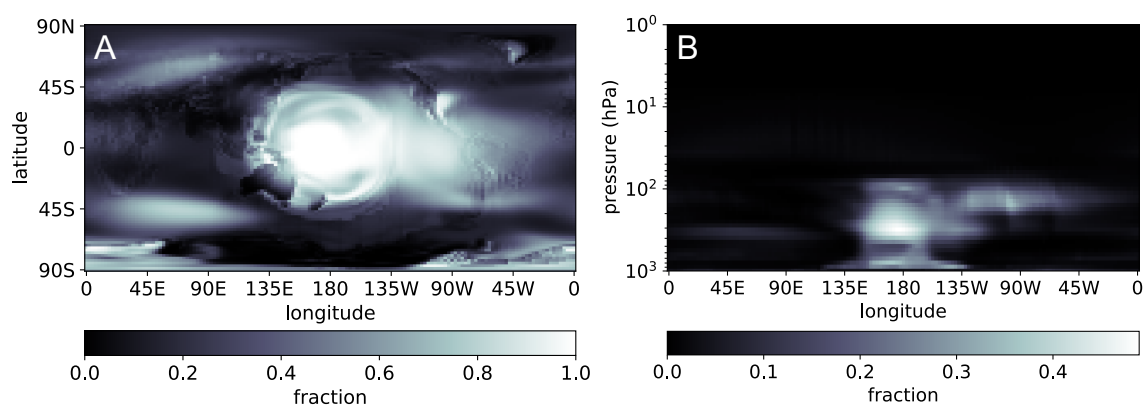


Figure 3.S3. Average cloud distribution. (A) Cloud fraction. The contributions from all vertical layers are considered. (B) Meridional mean cloud fraction as a function of longitude and atmospheric pressure. The substellar point is located at 0°N , 180°E . Convective clouds form in the substellar region and are transported eastward by westerly wind in the upper troposphere. The terminator at 90°E is almost free of cloud. Some cloud exists at the terminator at 90°W . Cloud top is located at about 100 hPa.

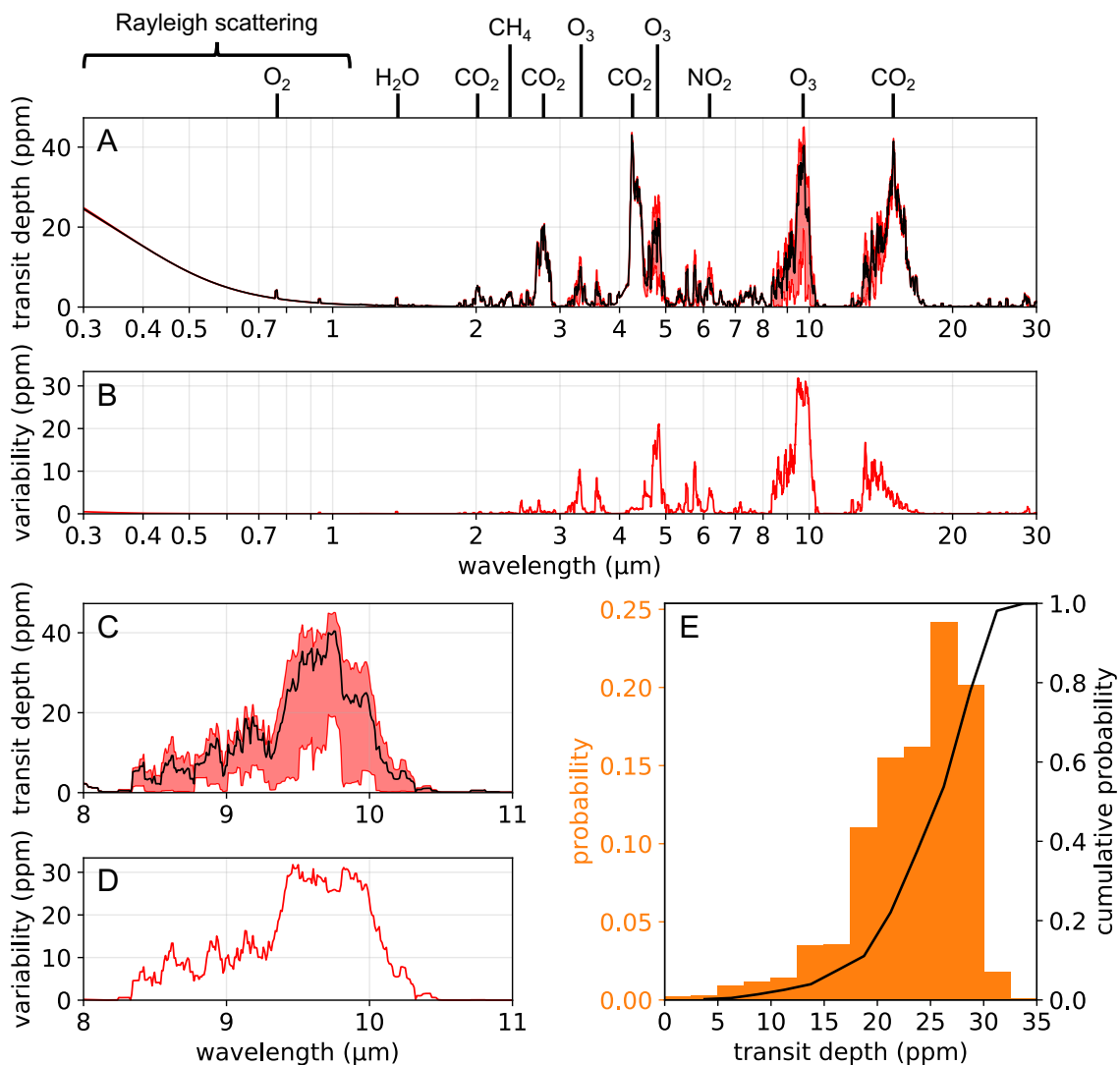


Figure 3.S4. Observational prospects in a cloudy scenario. Same as Fig. 3.5, except for an assumed, optically thick cloud deck located at 100 hPa over the entire globe which mutes all spectral features of absorbing species underneath. Compared to the clear-sky scenario, the time mean transit depth at 9.6 μm is reduced from 60 ppm to 40 ppm, which doubles the required exposure time. The variability of transit depth is reduced from 50 ppm to 30 ppm, almost tripling the required exposure time. But these reductions should be considered as the upper bound as cloud is patchy at the terminators (Fig. 3.S3).

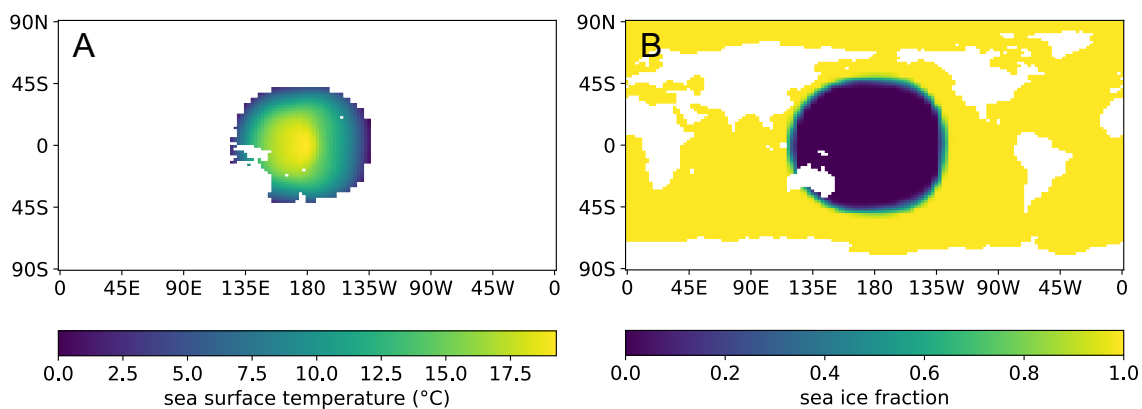


Figure 3.S5. Sea surface temperature and sea ice distribution. (A) Fixed sea surface temperature. Only grid boxes with 100% ocean fraction are shown. (B) Fixed sea ice fraction. Continent-only grid boxes are shown in white. Land-sea distribution of the modern Earth is used in the simulation.

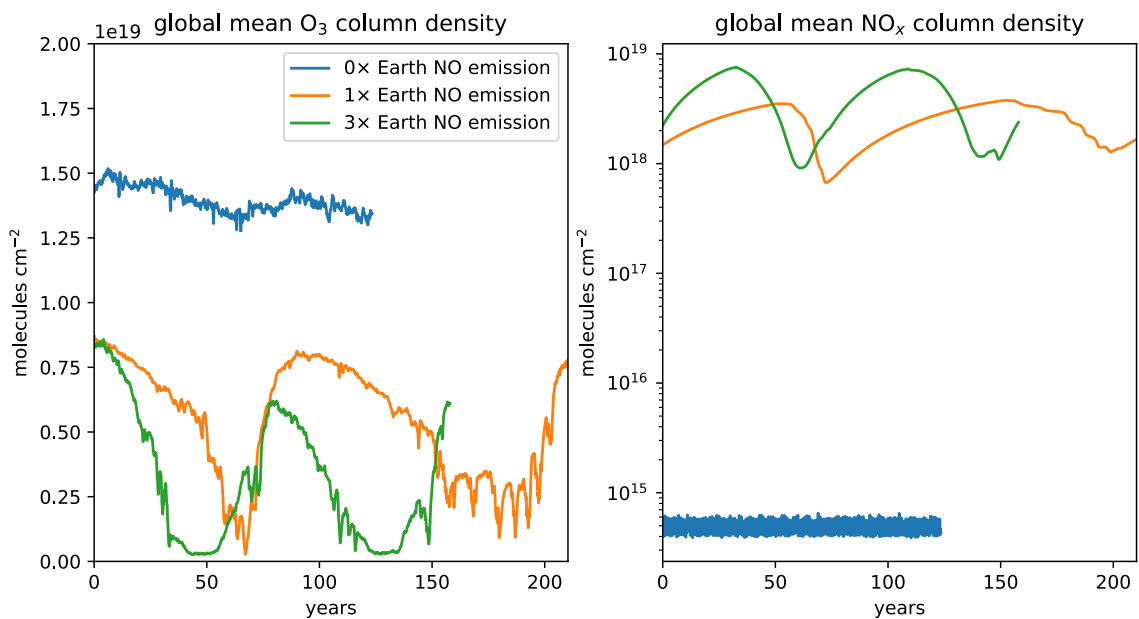


Figure 3.S6. Time series of the global mean column abundances of (left) O_3 and (right) NO_x with different NO emission fluxes. Self-sustained oscillations exist with the presence of an Earth-like surface NO emission flux or a surface NO emission flux that is three times the Earth's value. In the latter case, the oscillations are faster. There is no signature oscillation without surface NO emission.

*Chapter 4***Exchange Between the Mixed Layer and Thermocline Induced by
Mixed Layer Instability**Yangcheng Luo¹, Jörn Callies¹¹Division of Geological and Planetary Science, California Institute of Technology,
Pasadena, CA, USA

4.1 Abstract

Submesoscale turbulence in the upper ocean consists of fronts, filaments, and vortices that have horizontal scales between 100 m and 100 km. High-resolution numerical simulations have suggested that submesoscale turbulence is associated with strong vertical motion that could substantially enhance the vertical exchange between the mixed layer and the thermocline, which may have a profound impact on marine ecosystems and climate. Theoretical, numerical, and observational work indicates that submesoscale turbulence is energized primarily by baroclinic instability in the mixed layer, which is most vigorous in winter. In this study, we demonstrate how such mixed layer baroclinic instabilities induce vertical exchange between the mixed layer and the thermocline, and we propose a scaling law for the dependence of the exchange on environmental parameters. From linear stability analysis and nonlinear simulations, we show that the exchange, quantified by how much thermocline water is entrained into the mixed layer, is proportional to the mixed layer depth, is inversely proportional to the Richardson number of the thermocline, and increases with increasing Richardson number of the mixed layer. Our results imply that the tracer exchange between the mixed layer and thermocline is more efficient when the mixed layer is thicker, when the thermocline stratification is weaker, when the mixed layer stratification is stronger, or when the lateral buoyancy gradient is stronger. The scaling suggests vigorous exchange between deep mixed layers and the permanent thermocline in winter and in mode water formation areas.

4.2 Introduction

Submesoscale turbulence, characterized by horizontal scales between 100 m and 100 km, is an important feature in the upper ocean (Thomas et al., 2008; McWilliams, 2016). Unlike mesoscale motions that are typically characterized by Rossby number $Ro \ll 1$, the Rossby number of submesoscale turbulence can be up to $\mathcal{O}(1)$. Therefore, submesoscale turbulence cannot be accurately described by the quasi-geostrophic (QG) theories. With weaker geostrophic constraint that enforces horizontal nondivergence, submesoscale motions can locally generate strong vertical motions up to 100 meters per day in the upper

ocean—one order of magnitude stronger than those generated by mesoscale motions (Mahadevan & Tandon, 2006; Thomas et al., 2008). Large vertical velocities at the base of the mixed layer can lead to vertical transfer of tracers, such as nutrient, dissolved CO₂ and oxygen, and plankton, between the surface ocean and the interior. The vertical exchange has profound climatological and biological effects (Mahadevan & Archer, 2000; Lévy et al., 2001; Thomas et al., 2008; Lévy et al., 2012a; Lévy et al., 2012b; Mahadevan, 2014; Omand et al., 2015; Mahadevan, 2016; Balwada et al., 2018; Lévy et al., 2018). On one hand, strong downwelling takes heat, dissolved CO₂, and particulate organic carbon into the deep ocean (Omand et al., 2015), and then enhances heat and carbon uptake at the ocean surface (Balwada et al., 2018). The resulting acceleration in air-sea exchange has great implications in the context of global warming. Subduction of surface water can also export phytoplankton from the surface ocean into the interior, thus reducing primary productivity (Lévy et al., 2012a; Mahadevan, 2014). On the other hand, it has been proposed that enhanced upwelling speeds up primary production by taking nutrient-replete deep water into the euphotic surface layer, which overcomes surface oligotrophic conditions and leads to phytoplankton growth (Mahadevan & Archer, 2000; Lévy et al., 2001; Lévy et al., 2012a; Mahadevan, 2016), although some studies have cast doubt about the importance of submesoscale motions in this process (Lévy et al., 2018).

Submesoscale turbulence can be energized by a number of mechanisms (Mahadevan & Tandon, 2006; Thomas et al., 2008; McWilliams, 2016), such as mixed layer instability (MLI; Boccaletti et al., 2007; Callies et al., 2016), and strain-induced frontogenesis (McWilliams, 2021), etc. This paper focuses on the energization mechanism of MLI, which has been corroborated by observational evidence (Callies et al., 2015). Like baroclinic instability in the thermocline that energizes mesoscale eddies in the ocean, MLI energizes submesoscale eddies by tapping into potential energy stored in the mixed layer in the presence of a lateral buoyancy gradient caused by spatially heterogeneous surface buoyancy forcing. According to QG theories (Eady, 1949) which are often used to roughly characterize mixed layer baroclinic instability (e.g., Callies et al., 2016), the most unstable horizontal scale lies around the deformation radius of the mixed layer, $N_m h_m / f$, where N_m and h_m are the Brunt-Väisälä frequency and the thickness of the mixed layer, respectively, and f is the

Coriolis parameter. Under Richardson number $Ri \equiv N^2/\Lambda^2 \sim \mathcal{O}(1)$ conditions (where Λ is the vertical shear of the horizontal flow), this horizontal scale is slightly modified by non-QG effects (Stone, 1966, 1969, 1970). Under typical conditions of mixed layer stratification and thickness, the deformation radius of the mixed layer falls in the submesoscale range. QG theories suggest that the growth rate of MLI is close to the Eady growth rate of the mixed layer, $f\Lambda/N_m$. This scaling is also slightly modified by non-QG effects under $Ri \sim \mathcal{O}(1)$ conditions. Weak stratification in the mixed layer leads to large growth rates, which is consistent with the timescales of submesoscale turbulence—on the order of several days. Due to variations in the mixed layer depth and available potential energy, the strength of MLI undergoes seasonal cycles, consistent with the observed seasonality in submesoscale turbulence (Callies et al., 2015). The observed vertical structure of submesoscale energy, which is enhanced throughout the mixed layer and decays below its base, is also consistent with the energization mechanism of MLI (Callies et al., 2015).

Submesoscale turbulence plays two main roles in the upper ocean—restratifying the mixed layer and speeding up the exchange between the mixed layer and the thermocline. The former has received a good amount of attention (e.g., Boccaletti et al., 2007; Mahadevan et al., 2010) and a successful parameterization has been proposed (Fox-Kemper et al., 2008; Fox-Kemper & Ferrari, 2008; Fox-Kemper et al., 2011). In the parameterization, a scaling law for an overturning streamfunction for mixed layer eddies that restratifies the mixed layer is presented. The streamfunction is proportional to the product of the horizontal density gradient, the square of mixed layer depth, and the inertial period (Fox-Kemper et al., 2008), and its functionality has been demonstrated in both idealized and realistic ocean models. The streamfunction also advects tracers, but the parameterization does not explicitly account for the interaction between the mixed layer and thermocline.

As MLI is affected by various environmental conditions, such as the stratification of the mixed layer and the thermocline, the horizontal buoyancy gradient, and the vertical shear of the mean flow, it is expected that these environmental parameters also influence the vertical exchange caused by MLI-induced submesoscale motions. In this study, we first demonstrate how MLI induces vertical exchange between the mixed layer and thermocline, and then

explore the parameter dependence of the exchange. The physics revealed in this work can potentially be added to state-of-the-art boundary layer parameterization schemes in ocean global circulation models (e.g., Large et al., 1994; Fox-Kemper et al., 2011; Bachman et al., 2017; Van Roekel et al., 2018).

This article consists of two parts—linear stability analysis and nonlinear simulations, which will be discussed in the next two sections.

4.3 Linear stability analysis

4.3.1 Model formulation

We formulate the simplest model for MLI in a controlled setting—A two-layer Eady model (Fig. 4.1). We consider two layers, the upper one representing the ocean mixed layer and the lower one representing the thermocline. The mixed layer has a mean depth h_m and a Brunt-Väisälä frequency N_m . The thermocline has a mean depth h_t and a Brunt-Väisälä frequency N_t ($N_t > N_m$). These parameters are the background conditions in the linear stability analysis, and will also be the initial conditions in the nonlinear simulations presented in the next section. It is worth noting that an infinitely deep thermocline can isolate the MLI (Callies et al., 2016), but for the sake of computational feasibility, we add a flat, rigid bottom for the thermocline. In the linear stability analysis, $h_t = 5h_m$. In the nonlinear simulations, $h_t = h_m$. We only present the cases where MLI is well isolated.

For the sake of simplicity, we assume the same background horizontal buoyancy gradient (only in the y -direction) for the two layers, and we assume that the background buoyancy is continuous at the interface between the two layers, which makes the interface flat. With B representing the background buoyancy, we assume $\partial B / \partial y = -f\Lambda$. In the y - z plane, the sloping isopycnals are relatively tilted in the mixed layer and relatively flat in the thermocline. Conforming to the thermal wind relation, a vertical shear in the background flow exists in both layers, $\partial U / \partial z = \Lambda$, where U represents the background mean flow in the x -direction. We assume that the sea surface is located at $z = 0.5h_m$ and apply the rigid-lid approximation.

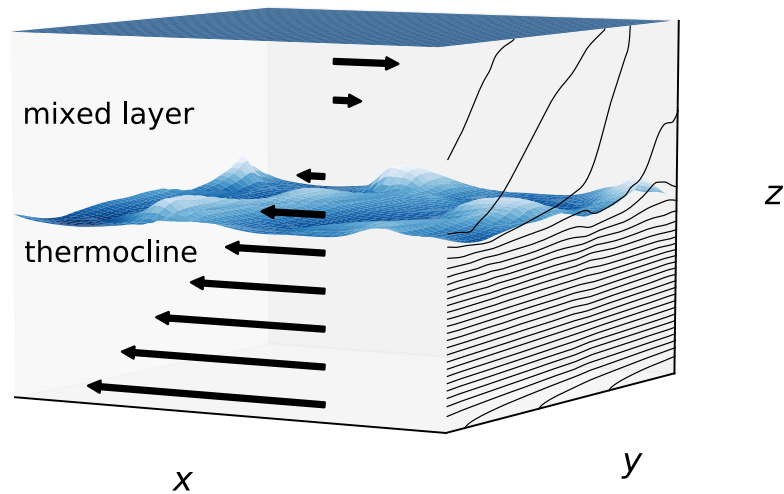


Figure 4.1. A schematic plot for the configuration of an Eady model for the mixed layer and the thermocline. A deformable interface separates the mixed layer and the thermocline. A flat sea surface is assumed. In an idealized model that isolates MLI, no model bottom exists, but in order to make numerical simulations feasible, a flat model bottom is assumed. The black arrows show the background flow in the x -direction. The contours in the y - z plane represent isopycnals. Data are taken from one of the nonlinear simulations in this study, with $Ri_m = 1$ and $Ri_t = 100$, at $t = 60 N_m/f\Lambda$.

The QG theories offer an approximate understanding of the MLI (Callies et al., 2016). Due to the discontinuity of stratification across the interface, a background potential vorticity (PV) sheet is present at the layer interface with the horizontal PV gradient in the $-y$ direction. This PV gradient gives rise to Rossby waves propagating in the $+x$ direction. The rigid surface acts as a layer with infinitely strong stratification. Due to the “effective” stratification jump across the surface, another background PV sheet is present at the surface with the horizontal PV gradient in the $+y$ direction. This PV gradient gives rise to Rossby waves propagating in the $-x$ direction. Due to the vertical shear in the background x -direction flow, the Rossby waves at the surface are Doppler shifted towards the $+x$ direction, and the Rossby waves at the interface are Doppler shifted towards the $-x$ direction. This allows the phase speeds (after Doppler shift) of the two sets of Rossby waves to be similar, thus the two sets of Rossby waves can be phase locked and mutually amplify. The mixed layer baroclinic instability hence emerges.

Rigorously speaking, the above QG reasoning only applies to circumstances where the Rossby number, Ro , (defined as $Ro = U/fL$, where U is the characteristic speed of the horizontal flow, and L is the characteristic horizontal length scale) of the two layers are much smaller than 1, but the QG reasoning still provides a heuristic perspective for understanding the dynamics. In the Eady model, Ro and Ri are related to each other by the following relationship: $Ro = 1/\sqrt{Ri}$. Therefore, the QG reasoning only applies to circumstances where Ri is much greater than 1. In the ocean, the mixed layer is typically observed to be weakly stratified and have a small Ri . The observed properties originate from two competing processes. On one hand, mechanical mixing induced by wind stress, negative surface buoyancy forcing, and cross-front Ekman transport induced by along-front wind stress can potentially reduce the stratification of the mixed layer down to zero or even negative values. On the other hand, fast-growing gravitational instability and symmetric instability can restore small Ri of the mixed layer back to 1 (Haine & Marshall, 1998). With Ri_m restored to ~ 1 , baroclinic instability becomes the fastest growing instability and further increases Ri_m by restratifying the mixed layer (Stone, 1966; Stone et al., 1969; Stone, 1970; Haine & Marshall, 1998). Therefore, in order to characterize the non-QG mixed layer dynamics with small Ri during the early stage of the development of the mixed layer baroclinic instability, we should use the primitive equations of fluid mechanics. As the magnitude of density variation in the model is far less than the density itself, we apply the Boussinesq approximation.

The primitive equations are linearized around the mean state:

$$\frac{\partial u}{\partial t} + \Lambda z \frac{\partial u}{\partial x} + w\Lambda - fv = -\frac{1}{\rho_o} \frac{\partial p}{\partial x}$$

$$\frac{\partial v}{\partial t} + \Lambda z \frac{\partial v}{\partial x} + fu = -\frac{1}{\rho_o} \frac{\partial p}{\partial y}$$

$$\frac{1}{\rho_o} \frac{\partial p}{\partial z} = b$$

$$\frac{\partial u}{\partial x} + \frac{\partial v}{\partial y} + \frac{\partial w}{\partial z} = 0$$

$$\frac{\partial b}{\partial t} + \Lambda z \frac{\partial b}{\partial x} - f \Lambda v + N^2 w = 0$$

In the equations above, u , v , and w represent perturbation velocities in the x -, y -, and z -directions on top of the background velocities $U = \Lambda(z - 0.5h_m)$, $V = W = 0$. p and b represent perturbation pressure and perturbation buoyancy. It is worth noting that the perturbation buoyancy is on top of the background buoyancy field that has a gradient of $-f\Lambda$ in the $+y$ direction and a gradient of N^2 in the $+z$ direction. The Brunt-Väisälä frequency N is equal to N_m in the mixed layer and is equal to N_t in the thermocline. For the sake of simplicity, hydrostatic approximation is adopted in the vertical momentum equation. Non-hydrostatic effects are shown to be insignificant for baroclinic instability unless the vertical shear Λ is far smaller than the Coriolis parameter f (Stone, 1971; Mahadevan, 2006; Callies & Ferrari, 2018).

Nondimensionalization is then performed to reduce the number of environmental parameters in the equations and simplify the parameter space. We pick the deformation radius of the mixed layer, $N_m h_m / f$, as the horizontal length scale, and the thicknesses of the two layers, h_m and h_t , as the vertical length scales for the mixed layer and the thermocline, respectively. For horizontal perturbation velocities, we pick Λh_m , the difference in the background horizontal velocity from the bottom of the mixed layer to the surface, as the velocity scale. We then choose the scales for all other variables based on dimensional relationships in geostrophic balance and hydrostatic balance—we pick $\Lambda h_m f / N_m$ and $\Lambda h_t f / N_m$ for the perturbation vertical velocity w in the mixed layer and the thermocline, respectively, $\rho_0 \Lambda h_m^2 N_m$ for the perturbation pressure in the two layers, $\Lambda h_m N_m$ and $\Lambda h_m^2 N_m / h_t$ for the perturbation buoyancy in the mixed layer and the thermocline, respectively, and $N_m / f \Lambda$ for time. The resulting dimensionless equations for the mixed layer are

$$\frac{1}{\sqrt{\text{Ri}_m}} \left(\frac{\partial u'}{\partial t'} + z' \frac{\partial u'}{\partial x'} + w' \right) - v' = - \frac{\partial p'}{\partial x'}$$

$$\frac{1}{\sqrt{\text{Ri}_m}} \left(\frac{\partial v'}{\partial t'} + z' \frac{\partial v'}{\partial x'} \right) + u' = - \frac{\partial p'}{\partial y'}$$

$$\begin{aligned}\frac{\partial p'}{\partial z'} &= b' \\ \frac{\partial u'}{\partial x'} + \frac{\partial v'}{\partial y'} + \frac{\partial w'}{\partial z'} &= 0 \\ \frac{1}{\sqrt{\text{Ri}_m}} \left(\frac{\partial b'}{\partial t'} + z' \frac{\partial b'}{\partial x'} - v' \right) + w' &= 0\end{aligned}$$

The resulting dimensionless equations for the thermocline are

$$\begin{aligned}\frac{1}{\sqrt{\text{Ri}_m}} \left(\frac{\partial u'}{\partial t'} + \gamma z' \frac{\partial u'}{\partial x'} + \gamma w' \right) - v' &= -\frac{\partial p'}{\partial x'} \\ \frac{1}{\sqrt{\text{Ri}_m}} \left(\frac{\partial v'}{\partial t'} + \gamma z' \frac{\partial v'}{\partial x'} \right) + u' &= -\frac{\partial p'}{\partial y'} \\ \frac{\partial p'}{\partial z'} &= b' \\ \frac{\partial u'}{\partial x'} + \frac{\partial v'}{\partial y'} + \frac{\partial w'}{\partial z'} &= 0 \\ \frac{1}{\sqrt{\text{Ri}_m}} \left(\frac{\partial b'}{\partial t'} + \gamma z' \frac{\partial b'}{\partial x'} - \gamma v' \right) + \frac{\text{Ri}_t}{\text{Ri}_m} \gamma^2 w' &= 0\end{aligned}$$

where primes denote dimensionless variables.

The dimensionless equations show that the problem is only determined by three dimensionless numbers—the Richardson number of the mixed layer (Ri_m), the Richardson number of the thermocline (Ri_t), and the ratio of the thermocline thickness to the mixed layer thickness ($\gamma = h_t/h_m$). For the boundary conditions, we assume zero vertical velocities at the sea surface and at the base of the thermocline. w and p are continuous at the layer interface. Plugging in wave ansatzes such as $u = \text{Re}\{\hat{u}(z)\exp[i(kx + ly - \omega t)]\}$ for all the variables u , v , w , p , and b , where k and l are the horizontal wavenumbers in the x - and y -directions, respectively, the equations above can be transformed into an eigenvalue problem of ω . We then use Dedalus, an open-source code that solves differential equations using spectral methods (Burns et al., 2020), to solve the discretized equations and obtain a

numerical solution for the dispersion relationship for different combinations of the three dimensionless parameters. In the solution $\omega = \omega(k, l; \text{Ri}_m, \text{Ri}_t, \gamma)$, ω is a complex number. Its real part ω_r can be used to retrieve the horizontal phase speed in the x - and y -directions, c_x and c_y — $c_x = \omega_r/k$ and $c_y = \omega_r/l$. The imaginary part of ω , denoted as σ , is the exponential growth rate of the instability. In addition to the dispersion relationship, the vertical structures of the oscillation amplitude of all the variables, namely, $\hat{u}(z)$, $\hat{v}(z)$, $\hat{w}(z)$, $\hat{p}(z)$, and $\hat{b}(z)$, can also be obtained. These can inform where MLI-induced motion is the strongest and how energy is vertically distributed.

Preliminary test experiments show that $\gamma = 5$ is sufficient for isolating MLI from the influence of the rigid bottom of the thermocline, so we use $\gamma = 5$ in all the linear stability analyses. In the spectral space, we resolve the mixed layer, located between $z = 0.5 h_m$ and $z = -0.5 h_m$, with 128 Chebyshev modes. We also resolve the thermocline, located between $z = -0.5 h_m$ and $z = -5.5 h_m$, with 128 Chebyshev modes. The vertical resolutions of the two layers are hence 128 unevenly spaced vertical layers in the mixed layer and 128 unevenly spaced vertical layers in the thermocline in the physical space. The grid spacing is smaller near the ocean surface, near the layer interface, and near the bottom of the thermocline. It is larger in the interior of each layer.

4.3.2 Results

As shown in Stone (1966), at the same k , the largest growth rate always takes place when $l = 0$, so we focus on the $l = 0$ cases.

The dispersion relationship shows two peaks in the growth rate curve, similar to Fig. 5a in Callies et al. (2016). The peak at smaller wavenumbers corresponds to the thermocline baroclinic instability, produced by the PV gradient reversal between the surface and the bottom of the thermocline. The maximum growth rate, $\sim 0.3 f\Lambda/N_t$, takes place near the Rossby deformation radius of the thermocline at $1.6 N_t h_t/f$. The peak at larger wavenumbers corresponds to MLI. The maximum growth rate takes place near the Rossby deformation radius of the mixed layer, ranging from $1.1 N_m h_m/f$ to $1.6 N_m h_m/f$,

depending on Ri of the two layers. The maximum growth rate is between $0.23 f\Lambda/N_m$ and $0.3 f\Lambda/N_m$. As typically $N_t h_t \gg N_m h_m$, the two growth rate peaks are well separated from each other in terms of spatial scales. Also, as typically $N_t \gg N_m$, MLI always outcompetes thermocline instability in terms of the maximum growth rate.

Figure 4.2 shows typical spatial structures associated with the fastest growing MLI modes in the x - z plane. As shown by the plots of u , v , and w oscillations, the MLI-induced flow is mostly confined within the mixed layer, from $z = -0.5 h_m$ to $z = 0.5 h_m$, and the modes tilt in the $-x$ direction. The largest amplitudes of u and v oscillations are located at the surface ($z = 0.5 h_m$) and at the layer interface ($z = -0.5 h_m$) (Fig. 4.2a, b). On the contrary, the largest amplitude of the w oscillation takes place at the midplane of the mixed layer (Fig. 4.2c). Importantly, the oscillations of u , v , and w all extend into the upper part of the thermocline. In particular, the w oscillation at the layer interface can cause vertical displacement of the interface, resulting in vertical exchange between the mixed layer and thermocline. The dependence of the vertical structure of the w oscillation on Ri_t is illustrated in Fig. 4.3. At the layer interface ($z = -0.5 h_m$), the amplitude of the w oscillation decreases as Ri_t increases, indicating that large Ri_t suppresses vertical motion at the layer interface.

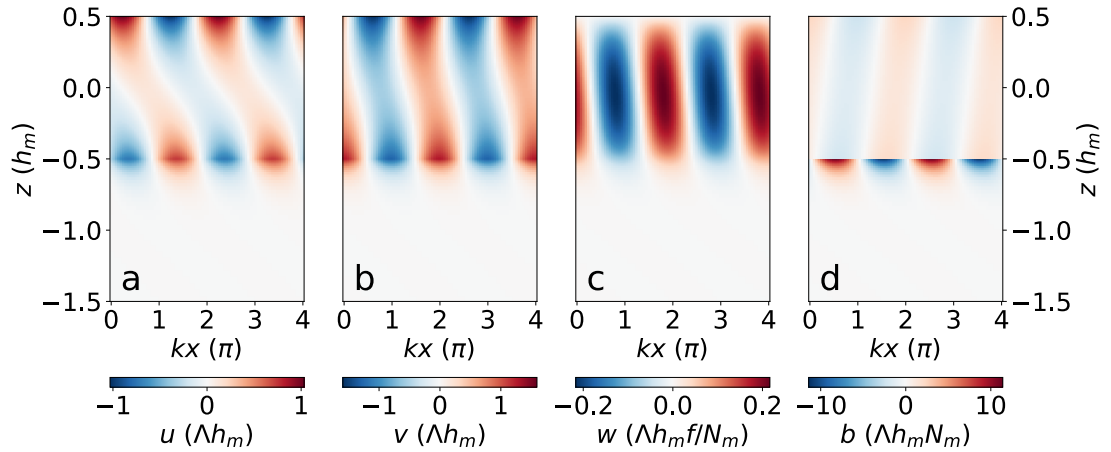


Figure 4.2. Spatial structures of the MLI modes. The four panels show (a) u , (b) v , (c) w , and (d) b . The x -axes show the distance in the x -direction multiplied by the most unstable k . The y -axes show depth. The mixed layer is located between $z = 0.5 h_m$ and $z = -0.5 h_m$. The thermocline is located below $z = -0.5 h_m$ (only the upper part is shown). The quantity against which a variable is nondimensionalized is shown in parentheses. Data are taken from the linear analysis with $Ri_m = 1$ and $Ri_t = 100$. The

magnitudes of the variables are scaled such that the horizontally averaged energy in the water column is equal to $\rho_0 \Lambda^2 h_m^3$.

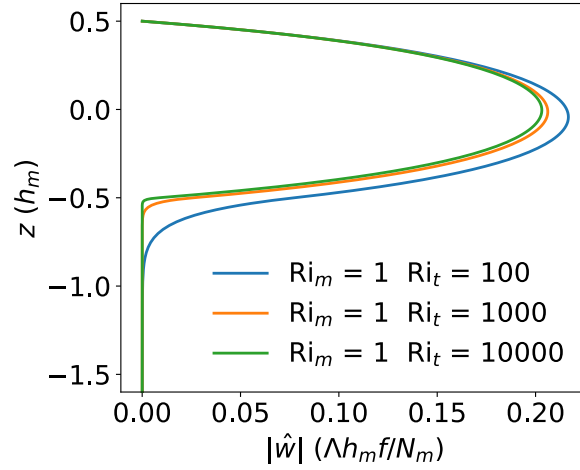


Figure 4.3. Large Richardson numbers of the thermocline, Ri_t , suppress vertical velocity at the interface between the mixed layer and the thermocline. Shown are the vertical structures of the amplitude of the MLI-induced w oscillation. The interface is located at $z = -0.5 h_m$. Data are taken from three linear stability analyses. The magnitudes of the variables are scaled such that the horizontally averaged energy in the water column is equal to $\rho_0 \Lambda^2 h_m^3$.

The spatial structure of the b oscillation is different from those of u , v , and w (Fig. 4.2d). The largest amplitude takes place beneath the layer interface. In the thermocline, the amplitude decays with depth, and the modes tilt towards the $-x$ direction. The amplitude of the b oscillation in the mixed layer is small, and its largest values take place at the surface and just above the interface. The modes in the mixed layer tilt towards the $+x$ direction. There is an abrupt phase shift across the interface. For typical Richardson numbers of the mixed layer and the thermocline, the phase shift is $\sim 180^\circ$, due to the fact that the MLI-induced motion in the y - z plane is oriented between the isopycnal slopes in the mixed layer and in the thermocline. The value of the phase shift depends on Ri_m and Ri_t .

It is worth noting that the oscillation amplitudes shown in Figs. 4.2 and 4.3 scale with the square root of eddy energy. Eddy energy is defined as the sum of eddy kinetic energy (EKE) and eddy potential energy (EPE). Under Boussinesq approximation, EKE takes the form

$$\text{EKE} = \frac{1}{2} \rho_0 (u^2 + v^2)$$

And EPE takes the form

$$\text{EPE} = \frac{\rho_0 b^2}{2N^2}$$

where N is evaluated with N_m or N_t accordingly in the two layers. To illustrate the spatial structures of the MLI modes, we normalize the horizontal mean column-integrated eddy energy to $\rho_0 \Lambda^2 h_m^3$. The normalization has a physical meaning—the energy associated with the eddies in the mixed layer is roughly comparable to the energy associated with the mean state in the mixed layer. This roughly marks the transition point from the linear phase of the instability development to the nonlinear phase. The relationship between the energy normalization and the transition point will be further discussed in the Discussion and Summary section.

Figure 4.4 shows the dependence of linear model on Ri_m and Ri_t . The ranges of the Richardson numbers discussed here, $1 \leq \text{Ri}_m \leq 3160$, $63 \leq \text{Ri}_t \leq 10^5$, cover all typical conditions in the real upper ocean. Our test results show that when Ri_m and Ri_t are too close to each other (e.g., when the stratification jump across the interface between the mixed layer and the thermocline is small enough), MLI modes extend downwards far below the base of the mixed layer and touch the bottom of the thermocline. To avoid the interference from the artificial thermocline bottom, we only present the cases with $\text{Ri}_t \geq 30 \text{ Ri}_m$, such that the largest oscillation amplitudes of u , v , w , p , and b in the interior of the thermocline are all smaller than 1% of their largest amplitudes in the mixed layer.

Figure 4.4a shows the dependence of the most unstable x -direction wavenumber k (the k associated with the highest growth rate of the instability) on Ri_m and Ri_t . In the middle right part of the figure, Ri_m is ~ 100 , and Ri_t approaches 10^5 , so the mixed layer approaches the QG limit and the base of the mixed layer approximates a rigid bottom. This analogy was highlighted in Nakamura & Held (1989) when they described a low PV layer sandwiched by two high PV layers. (High Ri is equivalent to high PV, as will be shown in the next section.) The most unstable k takes its highest value $\sim 1.6 f / N_m h_m$ in the middle right part of the figure, consistent with the result from the QG Eady model for baroclinic instability (Eady, 1949). As Ri_m decreases, the mixed layer moves away from the QG limit, and the most

unstable k (k_{max}) decreases towards $\sim 1.1 f/N_m h_m$. This decreasing trend of k_{max} is consistent with the analytical solution in Stone et al. (1966) for a single-layer model:

$$k_{max} \approx \left(\frac{5/2}{1 + 1/Ri} \right)^{1/2} \frac{f}{Nh}$$

This behavior is observed for a broad range of Ri_t , indicating that non-QG dynamics in general results in larger horizontal scales of baroclinic instability (in units of the Rossby deformation radius) than QG dynamics. When Ri_t approaches Ri_m , the most unstable k also decreases due to the modification of the MLI modes by the thermocline as the MLI modes penetrate deeper into the thermocline.

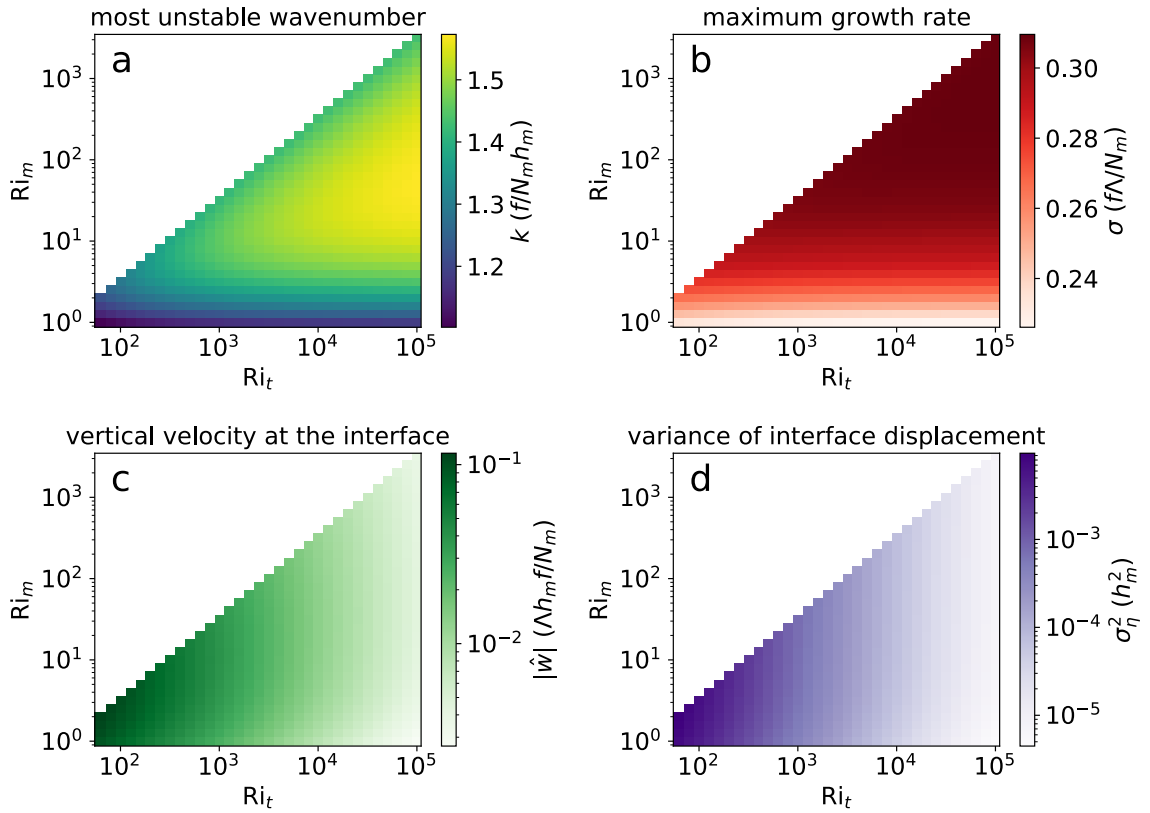


Figure 4.4. Dependence of the behaviors of the linear model on the Richardson numbers of the two layers. The four panels show the dependence of (a) the most unstable x -direction wavenumber k_{max} , (b) the largest growth rate of the instability over all horizontal wavenumbers, (c) the oscillation amplitude of w at the layer interface, and (d) the variance of the vertical displacement of the interface, η , on the Richardson numbers of the mixed layer and of the thermocline, Ri_m and Ri_t . The magnitudes of the variables are scaled such that the horizontally averaged energy in the water column is equal to $\rho_0 \Lambda^2 h_m^3$.

The maximum growth rate of mixed layer instability (“maximum” with respect to different k) depends on Ri_m only (Fig. 4.4b). In the upper half of the figure where $Ri_m \gg 1$, the result from the QG Eady model is reproduced—the maximum growth rate is about $0.3 f\Lambda/N_m$. As Ri_m decreases, the mixed layer moves away from the QG limit, and the maximum growth rate decreases, again consistent with the scaling in Stone (1966):

$$\sigma_{max} \approx \left(\frac{5/54}{1 + 1/Ri} \right)^{1/2} \frac{f\Lambda}{N}$$

This indicates that non-QG dynamics results in slower growth of baroclinic instability (in units of $f\Lambda/N$, the dimension for the growth rate). Note that this is a secondary effect on top of the change in the growth rate dimension itself, which equals f/\sqrt{Ri} and increases with stronger non-QG dynamics at decreasing Ri . Also note that the trends in k_{max} and σ_{max} are independent of the energy normalization.

With the column-integrated energy normalized to $\rho_0\Lambda^2h_m^3$, the nondimensionalized vertical velocity at the layer interface has a strong dependence on Ri_t and a negligible dependence on Ri_m (Fig. 4.4c). Increasing Ri_t from 10^2 to 10^5 reduces the nondimensionalized w oscillation amplitude at the interface from $0.1 \Lambda h_m f/N_m$ to $0.003 \Lambda h_m f/N_m$. The reduction of w at the base of the mixed layer is unrelated to the amplitude of w in the interior of the mixed layer, whose change is small, as illustrated in Fig. 4.3. Taking the scale of w (which is $\Lambda h_m f/N_m = h_m f/\sqrt{Ri_m}$) into consideration, the oscillation amplitude of the dimensional w decreases with increasing Ri_m —the former is proportional to $1/\sqrt{Ri_m}$ (with the column-integrated energy normalized to $\rho_0\Lambda^2h_m^3$).

Figure 4.4d provides another perspective for how large Ri_t damps vertical motion at the base of the mixed layer—the variance of the vertical displacement of the layer interface, η . η is approximately zero in the initial state. The magnitude of the interface deformation is a more straightforward indicator of the vertical exchange across the base of the mixed layer than the magnitude of w , as the amplification of the interface deformation is caused by the correlation between w and η , rather than w alone. This is because the growth rate of the variance of the vertical displacement of the interface is

$$\frac{d\sigma_\eta^2}{dt} = \frac{d\overline{\eta^2}}{dt} = \frac{\partial\overline{\eta^2}}{\partial t} = \overline{2\eta \frac{\partial\eta}{\partial t}} = \overline{2\eta w}$$

where overbars denote horizontal average and $\partial\eta/\partial t = w$ is used. If η and w are in phase, the deformation of the interface grows, and vice versa.

Like w at the layer interface, the nondimensionalized (against h_m) variance of the interface displacement strongly depends on Ri_t and does not depend on Ri_m . Increasing Ri_t from 10^2 to 10^5 results in its decrease from $0.01 h_m^2$ to $5 \times 10^{-6} h_m^2$. But unlike w at the layer interface, the scale of σ_η^2 (which is h_m^2) does not contain Ri_m , so the dimensional σ_η^2 has no Ri_m dependence (with the column-integrated energy normalized to $\rho_0 \Lambda^2 h_m^3$). This is seemingly inconsistent with the negative Ri_m dependence of w at the layer interface. The key to resolve the inconsistency lies in the scale of time— $N_m/f\Lambda = \sqrt{\text{Ri}_m}/f$, which scales with $\sqrt{\text{Ri}_m}$, canceling out the reducing effect of increasing Ri_m on the scale of w .

It is worth noting that the magnitudes of w and σ_η^2 relies on the energy normalization, as stated above, but it is roughly the transition points from the linear phase to the nonlinear phase of the instability development that are being compared here. It is also worth noting that the $\sqrt{\text{Ri}_t}$ dependences shown in Figs. 4.4c and 4.4d should be understood qualitatively, as nonlinearity in the later stage of the instability development can stretch sinusoidal waves to filaments that the wave ansatzes can no longer describe, and the exchange happens when filaments of thermocline water are entrained into the mixed layer, as shown by the nonlinear simulations in the next section.

The dimension chosen for σ_η^2 and the parameter dependence of the nondimensionalized σ_η^2 inform where strong exchange between the mixed layer and the thermocline can be found in the real ocean. The dimension itself, h_m^2 , implies that deep mixed layers, as observed in regions with negative surface buoyancy forcing and strong wind-induced mixing, e.g., the Southern Ocean (e.g., de Boyer Montégut et al., 2004), are favorable for strong vertical exchange. The dependence of σ_η^2 on $\text{Ri}_t = N_t^2/\Lambda^2$ implies that weakly stratified thermocline, as observed in the Southern Ocean and in the mode water formation regions in the western part of subtropical gyres, and strong horizontal buoyancy gradient (or

equivalently, strong vertical shear in the background flow), as observed in the Southern Ocean and near the western boundary currents, are favorable for strong vertical exchange across the base of the mixed layer.

4.4 Nonlinear simulations

4.4.1 Model formulation

To characterize the parameter dependence of the vertical exchange in the nonlinear phase of the instability development, we pose an initial-value problem, where the system freely evolves from idealized initial states. No external forcings are enforced. The model configuration is modified based on that in the linear stability analysis—only γ is reduced from 5 to 1 in order to better resolve the mixed layer. The simulation domain spans from $x = 0$ to $12 N_m h_m / f$, from $y = 0$ to $12 N_m h_m / f$, and from $z = -1.5 h_m$ to $0.5 h_m$. The domain is doubly periodic in the horizontal directions. In the initial states, the upper half of the domain (from $z = -0.5 h_m$ to $0.5 h_m$) represents the mixed layer with a small Richardson number Ri_m , and the lower half (from $z = -1.5 h_m$ to $-0.5 h_m$) represents the thermocline with a large Ri_t . Note that computationally, there is only one layer sandwiched by two rigid lids representing the sea surface and the bottom of the thermocline (an artificial boundary only for computational feasibility), and the layer is initially weakly stratified in the upper half and strongly stratified in the lower half. This is different from the two-layer model in the linear stability analysis.

The nonlinear terms that are dropped in the linear stability analysis are now restored

$$\frac{\partial u}{\partial t} + (\Lambda z + u) \frac{\partial u}{\partial x} + v \frac{\partial u}{\partial y} + w \left(\Lambda + \frac{\partial u}{\partial z} \right) - f v = - \frac{1}{\rho_o} \frac{\partial p}{\partial x} + \mathcal{F}(u)$$

$$\frac{\partial v}{\partial t} + (\Lambda z + u) \frac{\partial v}{\partial x} + v \frac{\partial v}{\partial y} + w \frac{\partial v}{\partial z} + f u = - \frac{1}{\rho_o} \frac{\partial p}{\partial y} + \mathcal{F}(v)$$

$$\frac{1}{\rho_o} \frac{\partial p}{\partial z} = b$$

$$\frac{\partial u}{\partial x} + \frac{\partial v}{\partial y} + \frac{\partial w}{\partial z} = 0$$

$$\frac{\partial b}{\partial t} + (\Lambda z + u) \frac{\partial b}{\partial x} + v \left(-f\Lambda + \frac{\partial b}{\partial y} \right) + w \frac{\partial b}{\partial z} = \mathcal{F}(b)$$

where $\mathcal{F}(u)$, $\mathcal{F}(v)$, and $\mathcal{F}(b)$ represent hyperviscosity terms that are used to limit forward cascade of energy and stabilize the numerical simulation. The Prandtl number $\text{Pr} = 1$ is assumed, which means that momentum diffusion and thermal diffusion are at an equal pace. \mathcal{F} consists of fourth-order hyperviscosity in the horizontal directions and second-order hyperviscosity in the vertical direction. It takes the form

$$\mathcal{F} = -\mu \left(\frac{\partial^4}{\partial x^4} + 2 \frac{\partial^4}{\partial x^2 \partial y^2} + \frac{\partial^4}{\partial y^4} \right) + \nu \frac{\partial^2}{\partial z^2}$$

The fourth-order hyperviscosity in the horizontal directions can more efficiently suppress fine-scale horizontal gradients.

Note that the decomposition of buoyancy into background buoyancy B and perturbation buoyancy b in the nonlinear simulations is different from that in the linear stability analysis. In the linear stability analysis, the background B has a vertical stratification N^2 , whereas in the nonlinear simulations, N^2 is in the initial state of the perturbation b , which allows significant variations in N^2 .

In addition to the five variables in the linear stability analysis, we apply a tracer field c to trace water that is initially in the thermocline. c follows an equation similar to the buoyancy equation

$$\frac{\partial c}{\partial t} + (\Lambda z + u) \frac{\partial c}{\partial x} + v \frac{\partial c}{\partial y} + w \frac{\partial c}{\partial z} = \mathcal{F}(c)$$

For boundary conditions, we apply rigid boundaries $w = 0$ at the top of the mixed layer and at the bottom of the thermocline. No surface or bottom stress is assumed: $\partial u / \partial z = \partial v / \partial z = 0$. Meanwhile, no buoyancy forcing or tracer injection is applied at the boundaries: $\partial b / \partial z = 0$, $\partial c / \partial z = 0$.

The initial state of the model consists of a background x -direction flow $U = \Lambda(z - 0.5 h_m)$ with the perturbation flow $u = v = w = 0$. On top of a background lateral buoyancy gradient $\partial B/\partial y = -f\Lambda$, the vertical gradient of the perturbation buoyancy b is initialized using a \tanh function in order to mitigate truncation error associated with the step function:

$$b = \left[-\frac{1}{2} \left(\frac{\text{Ri}_t}{\text{Ri}_m} - 1 \right) \text{Ri}_m^{1/2} \frac{z_0}{h_m} \ln \left(2 \cosh \frac{z + 0.5 h_m}{z_0} \right) + \frac{1}{2} \left(\frac{\text{Ri}_t}{\text{Ri}_m} + 1 \right) \text{Ri}_m^{1/2} \frac{z}{h_m} + \frac{1}{4} \left(\frac{\text{Ri}_t}{\text{Ri}_m} - 1 \right) \text{Ri}_m^{1/2} \right] \Lambda h_m N_m$$

where $z_0 = 0.02 h_m$ is an arbitrarily chosen parameter that represents the thickness of the “smooth zone” between the mixed layer and the thermocline in the initial state. Away from the layer interface, $\partial b/\partial z \approx N_m^2$ in the mixed layer, and $\partial b/\partial z \approx N_t^2$ in the thermocline. b is continuous at the initial layer interface. The tracer concentration c is set to 1 (dimensionless) in the thermocline and 0 in the mixed layer. We will refer to c as the “binary tracer” hereinafter.

As in the linear stability analysis, the equations above are nondimensionalized. We pick the Rossby deformation radius of the mixed layer in the initial state, $N_m h_m / f$, as the horizontal length scale, the initial thickness of the mixed layer h_m as the vertical length scale, Λh_m as the scale for the perturbation horizontal velocity u and v . We then choose the scales for all other variables (except c) according to dimensional relationships in geostrophic balance and hydrostatic balance—we pick $\Lambda h_m f / N_m$ for perturbation vertical velocity w , $\rho_0 \Lambda h_m^2 N_m$ for perturbation pressure, $\Lambda h_m N_m$ for perturbation buoyancy, and $N_m / f \Lambda$ for time. The hyperviscosity coefficients μ and ν are nondimensionalized as follows— $\mu = \Lambda N_m^3 h_m^4 / f^3 \text{Re}$, $\nu = \Lambda h_m^2 f / N_m \text{Re}$, where Re is the Reynolds number which indicates the relative importance of the advection terms with respect to the hyperviscosity terms. Re should be as large as possible. We set $\text{Re} = 10^4$, the largest possible Re that does not incur checkerboard instability.

The dimensionless equations of motion are

$$\frac{1}{\sqrt{\text{Ri}_m}} \left[\frac{\partial u'}{\partial t'} + (z' + u') \frac{\partial u'}{\partial x'} + v' \frac{\partial u'}{\partial y'} + w' \left(1 + \frac{\partial u'}{\partial z'} \right) \right] - v' = -\frac{\partial p'}{\partial x'} + \mathcal{F}'(u')$$

$$\frac{1}{\sqrt{\text{Ri}_m}} \left[\frac{\partial v'}{\partial t'} + (z' + u') \frac{\partial v'}{\partial x'} + v' \frac{\partial v'}{\partial y'} + w' \frac{\partial v'}{\partial z'} \right] + u' = -\frac{\partial p'}{\partial y'} + \mathcal{F}'(v')$$

$$\frac{\partial p'}{\partial z'} = b'$$

$$\frac{\partial u'}{\partial x'} + \frac{\partial v'}{\partial y'} + \frac{\partial w'}{\partial z'} = 0$$

$$\frac{1}{\sqrt{\text{Ri}_m}} \left[\frac{\partial b'}{\partial t'} + (z' + u') \frac{\partial b'}{\partial x'} + v' \left(-1 + \frac{\partial b'}{\partial y'} \right) + w' \frac{\partial b'}{\partial z'} \right] = \mathcal{F}'(b')$$

$$\frac{1}{\sqrt{\text{Ri}_m}} \left[\frac{\partial c'}{\partial t'} + (z' + u') \frac{\partial c'}{\partial x'} + v' \frac{\partial c'}{\partial y'} + w' \frac{\partial c'}{\partial z'} \right] = \mathcal{F}'(c')$$

where \mathcal{F}' takes the form

$$\mathcal{F}' = -\frac{1}{\sqrt{\text{Ri}_m}} \frac{1}{\text{Re}} \left(\frac{\partial^4}{\partial x'^4} + 2 \frac{\partial^4}{\partial x'^2 \partial y'^2} + \frac{\partial^4}{\partial y'^4} \right) + \frac{1}{\sqrt{\text{Ri}_m}} \frac{1}{\text{Re}} \frac{\partial^2}{\partial z'^2}$$

We use Dedalus to solve the initial value problem. In the spectral space, we use 192 Fourier modes in both x - and y -directions, and use 256 Chebyshev modes in the z -direction. Translated into the physical space, these are equivalent to 192 evenly spaced grids in both x - and y -directions and 256 unevenly spaced grids in the z -direction. The linear stability analysis shows that the wavelength of mixed layer instability in the x -direction ranges from 3.9 to 5.7 $N_m h_m / f$. Therefore, with 192 Fourier modes resolving 12 $N_m h_m / f$ in the horizontal directions, each wavelength is resolved by 62 to 91 grids. The vertical grids are denser near the sea surface and near the bottom of the thermocline, and are sparser near the center of the water column where the base of the mixed layer is located in the initial state.

We add a white noise field to the perturbation buoyancy field b in order to break symmetry in the initial state. The values of the white noise at all grid points follow a Gaussian distribution with a mean value of zero and a standard deviation of 10^{-3} .

We sample six combinations of Ri_m and Ri_t : (1) $Ri_m = 1$ and $Ri_t = 10^2$, (2) $Ri_m = 1$ and $Ri_t = 10^3$, (3) $Ri_m = 1$ and $Ri_t = 10^4$, (4) $Ri_m = 10$ and $Ri_t = 10^3$, (5) $Ri_m = 10$ and $Ri_t = 10^4$, and (6) $Ri_m = 10^2$ and $Ri_t = 10^4$. Ri_m and Ri_t not only determine the initial state, but also determine the magnitude of deviation from QG dynamics. All the simulations start at $t = 0$ and end at $t = 100 N_m/f\Lambda$.

4.4.2 Results

Every nonlinear simulation undergoes four stages of evolution (Fig. 4.5). As its high-wavenumber variability is damped by diffusion, the artificially introduced white noise in the initial state quickly forms a pattern that is revealed in the linear stability analysis in Section 2.2, which is characterized by parallel stripes orienting in the y -direction with alternate positive and negative buoyancy anomalies in the x -direction (Fig. 4.5a). This demonstrates that the fastest growing mode of baroclinic stability is associated with $l = 0$. The buoyancy anomalies then grow exponentially until the relative vorticity becomes comparable to f , at which time a transition from the linear phase to the nonlinear phase happens (Fig. 4.5b). The subsequent nonlinear phase is characterized by small cyclonic and anticyclonic eddies that transport momentum, buoyancy, and the binary tracer (Fig. 4.5c). Gradually, the inverse cascade of energy comes into play, during which period of time vortices merge and grow in size. By the end of each simulation, there is a cyclonic vortex centered around a negative buoyancy anomaly at the midplane of the mixed layer (Fig. 4.5d), and the horizontally averaged buoyancy anomaly at this level has decreased below zero (the mean value in the initial state).

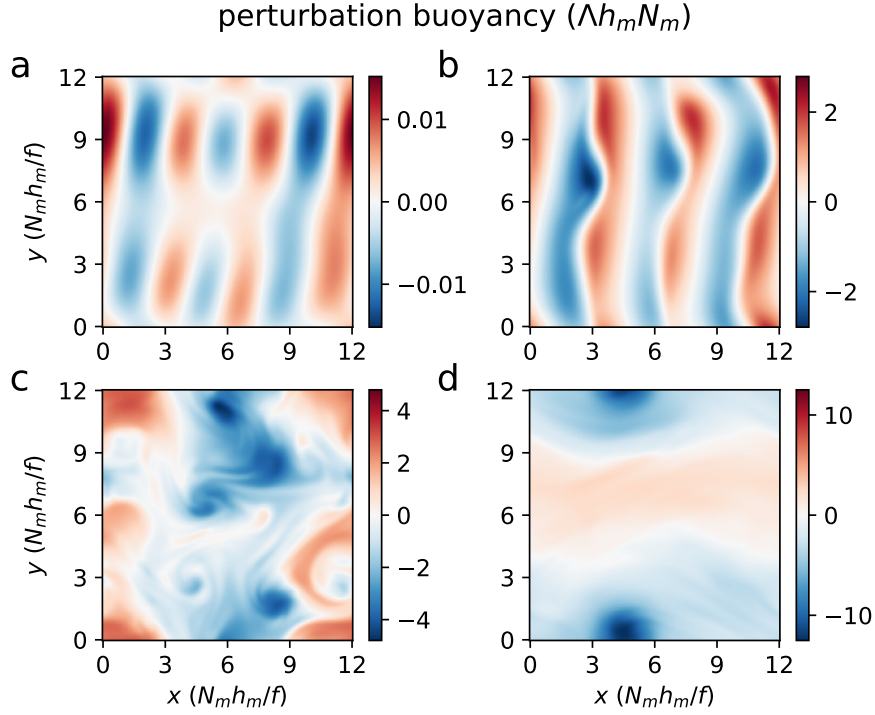


Figure 4.5. Snapshots of the evolution of the perturbation buoyancy b at the midplane of the mixed layer in a nonlinear simulation. Four panels show the four different stages of the evolution: (a) the linear phase, at $t = 29 N_m/f\Lambda$, (b) the transition point between the linear phase and the nonlinear phase, at $t = 48 N_m/f\Lambda$, (c) the early nonlinear phase, at $t = 55 N_m/f\Lambda$, and (d) the late nonlinear phase when the inverse cascade of energy has taken effect, at $t = 85$. Data are taken from a nonlinear simulation with $Ri_m = 10$ and $Ri_t = 10^3$.

After the nonlinear phase starts at $t \approx 50 N_m/f\Lambda$, vertical displacement of the base of the mixed layer becomes finite-amplitude, leading to entrainment of thermocline water into the mixed layer. This is evident from the evolving binary tracer and hydrostatic PV fields (Fig. 4.6). Hydrostatic PV is defined as

$$q_h = \left(f + \frac{\partial v}{\partial x} - \frac{\partial u}{\partial y} \right) \frac{\partial b}{\partial z} - \frac{\partial v}{\partial z} \frac{\partial b}{\partial x} + \left(\Lambda + \frac{\partial u}{\partial z} \right) \left(-f\Lambda + \frac{\partial b}{\partial y} \right)$$

In the initial state, $q_h = f\partial b/\partial z - f\Lambda^2 = fN^2 - f\Lambda^2 = f\Lambda^2(Ri - 1)$. Therefore, if we pick $f\Lambda^2$ as the dimension for PV, the nondimensionalized value q'_h in the initial state is equal to $Ri - 1$. Thus, water mass has a high nondimensionalized PV in the thermocline and a low nondimensionalized PV in the mixed layer in the initial state. Since PV is approximately conserved (it is rigorously conserved if the flow is inviscid), as the system

evolves, high hydrostatic PV serves as a tracer of thermocline water as high binary tracer concentration does. Figure 4.6a shows an x-z cross section of the binary tracer field, where water from the shallow thermocline with high tracer concentration forms filaments that extend upwards into the mixed layer. The cross section of hydrostatic PV shows similar patterns to that of the binary tracer in the lower part of the mixed layer, where high PV thermocline water forms filaments and is entrained upwards (Fig. 4.6b), similar to the PV intrusions into the low-PV intermediate layer caused by vortex rollup in Garner et al. (1992). As the low buoyancy and high PV thermocline water is gradually entrained into the mixed layer, at the midplane of the mixed layer ($z = 0$), the average buoyancy decreases, and vorticity has an increasingly positive bias, as shown in Fig. 4.5d.

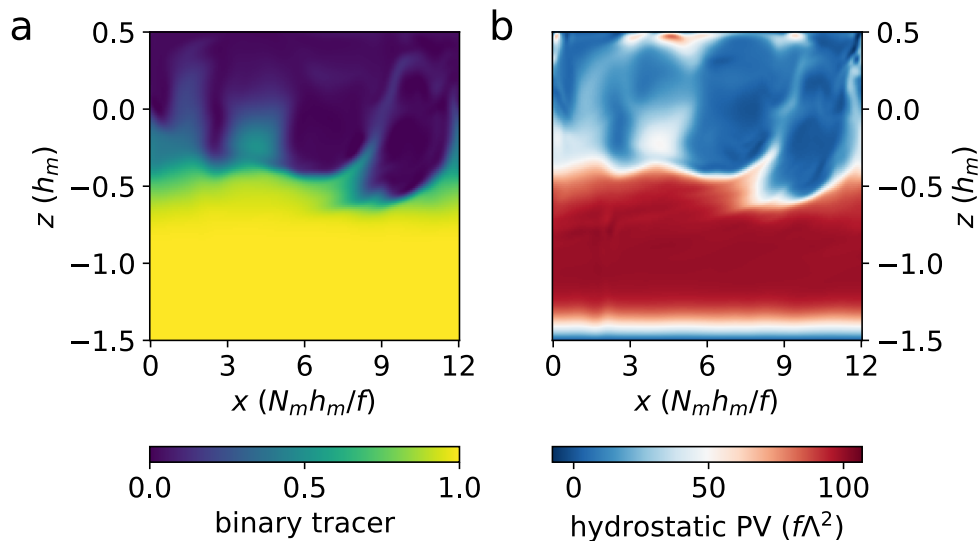


Figure 4.6. Binary tracer and hydrostatic PV trace each other in the nonlinear phase of nonlinear simulations. Thermocline water with (a) high binary tracer concentration and (b) high PV is entrained into the mixed layer. The initial interface between the mixed layer and the thermocline is located at $z = -0.5$. Data are taken from the nonlinear simulation with $Ri_m = 1$ and $Ri_t = 100$.

Unlike the lower part of the mixed layer where high PV filaments and high binary tracer filaments largely trace each other, the higher part of the mixed layer shows apparent discrepancies between the two. The binary tracer concentration near the sea surface keeps a close-to-zero value, because no tracer input is present at the surface (Fig. 4.6a). By contrast, high-PV blobs and filaments frequently appear near the sea surface, which can then be transported downwards into the interior of the mixed layer. This is because PV can be created

or destroyed in the presence of viscosity. The upward PV flux can be decomposed into three terms – an advection term

$$wq$$

a diffusion term

$$-\left(f + \frac{\partial v}{\partial x} - \frac{\partial u}{\partial y}\right)\mathcal{F}(b)$$

and a viscosity term

$$\frac{\partial b}{\partial x}\mathcal{F}(v) - \left(-f\Lambda + \frac{\partial b}{\partial y}\right)\mathcal{F}(u)$$

At the boundaries, the advection term is zero because $w = 0$, but the diffusion term and the viscosity term can be non-zero, leading to non-zero PV flux into or out of the domain.

Figure 4.7a shows the horizontally averaged binary tracer concentration in the interior of the mixed layer during the late linear phase and the nonlinear phase of the simulations. Consistent with the findings in the linear stability analysis, at any fixed Ri_m , increasing Ri_t suppresses the vertical exchange between the mixed layer and the thermocline. The analogy between a rigid boundary and an interface with an infinitely stratified layer (or a layer with an infinitely high Richardson number) in Nakamura & Held (1989) can inspire a scaling law between the amount of vertical exchange that happens between the mixed layer and thermocline (which is characterized by amount of thermocline water entrained into the interior of the mixed layer per unit area, defined as the “entrainment depth”) and the thermocline Richardson number Ri_t . The reasoning is as follows:

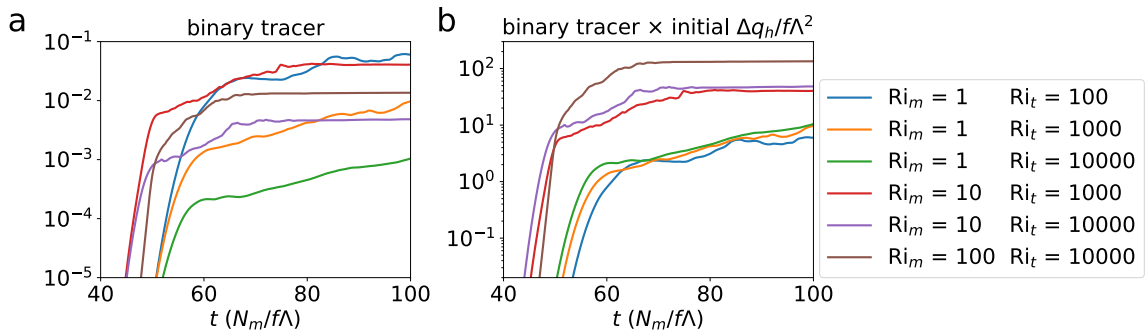


Figure 4.7. The amount of thermocline water entrained into the mixed layer is inversely proportional to the Richardson number difference between the mixed layer and the thermocline in the initial state. (a) Time series of the average binary tracer concentration in the interior of the mixed layer (at $z = 0.1 h_m$). (b) Times series of the product of the average binary tracer concentration in the interior of the mixed layer (at $z = 0.1 h_m$) and the difference between the Richardson numbers (which are the nondimensionalized PV) of the mixed layer and thermocline in the initial state. We present the level of $z = 0.1 h_m$ instead of the midplane of the mixed layer in the initial state ($z = 0$) because the base of the mixed layer is elevated by diffusion (see next section).

We assume that at realistic thermocline Richardson numbers, the analogy in Nakamura & Held (1989) is still approximately valid. Under this assumption, the mixed layer is sandwiched between two approximately symmetric boundaries (the rigid boundary at the sea surface and the quasi-rigid interface between the mixed layer and the thermocline). As is indicated by the nondimensionalization in Section 3.1, the dynamics in the mixed layer is determined by a single dimensionless number Ri_m . It means that the dimensionless hydrostatic PV q'_h (nondimensionalized against $f\Lambda^2$) in the mixed layer is only a function of Ri_m , dimensionless depth z' , and dimensionless time t' :

$$q'_h = q'_h(\text{Ri}_m, z', t')$$

We denote the column integrated PV in the mixed layer as Q_h , and its dimensionless form (nondimensionalized against $f\Lambda^2 h_m$) as Q'_h . Then, as the vertical integration excludes the dependence on z' , Q'_h is only a function of Ri_m and t' :

$$Q'_h = Q'_h(\text{Ri}_m, t')$$

Therefore, the PV increase rate in the mixed layer $R' \equiv \partial Q'_h / \partial t'$ also only depends on Ri_m and t' :

$$R' = R'(\text{Ri}_m, t')$$

We assume that at sufficiently large Ri_t , the PV increase in the mixed layer depends on no thermocline properties. Because PV can be regarded as a conserved quantity carried by fluid parcels in the limit of large Re , and the two boundaries of the mixed layer are approximately symmetric, the above assumption implies that the PV increase in the mixed layer is half sourced from the sea surface and half sourced from the interface with the

thermocline, the latter via high-PV thermocline water peeling off the thermocline and getting entrained into the mixed layer in filaments.

We denote the entrainment depth into the thermocline as D and its dimensionless form as D' ($D = h_m D'$), the PV contribution to the mixed layer from the thermocline (half of the total PV increase rate in the mixed layer) can be decomposed as the product of the PV difference between the two layers and the rate of change of the entrainment depth:

$$\frac{1}{2} R'(\text{Ri}_m, t') = (\text{Ri}_t - \text{Ri}_m) \frac{dD'}{dt'}$$

where Ri_t and Ri_m are the dimensionless hydrostatic PV of the thermocline and the mixed layer, respectively.

The left-hand side of the equation above has no Ri_t dependency, so the right-hand side also has no Ri_t dependency. That is to say, dD'/dt' can be decomposed as

$$\frac{dD'}{dt'} = \frac{1}{\text{Ri}_t - \text{Ri}_m} \varphi(\text{Ri}_m, t')$$

where φ is a dimensionless function of Ri_m and t' .

This means that the (dimensionless) entrainment depth at a certain time, D' , also takes the form

$$D' = \frac{1}{\text{Ri}_t - \text{Ri}_m} \Phi(\text{Ri}_m, t')$$

where Φ is the integral of φ over t' and is also a dimensionless function.

Figure 4.7b shows the time series of the product of the horizontally averaged binary tracer concentration (which represents the amount of vertical exchange between the mixed layer and the thermocline) multiplied by the initial $\text{Ri}_t - \text{Ri}_m$ in the nonlinear phases of the instability development. We can observe that for the same Ri_m , the curves with different Ri_t 's approximately converge, thus confirming the proposed scaling law.

Back to the dimensionless form,

$$D = h_m D' = \frac{h_m}{\text{Ri}_t - \text{Ri}_m} \Phi \left(\text{Ri}_m, \frac{f\Lambda}{N_m} t \right) \approx \frac{h_m}{\text{Ri}_t} \Phi \left(\text{Ri}_m, \frac{f\Lambda}{N_m} t \right)$$

The “ \approx ” sign holds because Ri_t is typically much greater than Ri_m in the real ocean. If we use the entrainment depth as a metric for the vertical exchange between the mixed layer and the thermocline, we can conclude that the vertical exchange is proportional to the thickness of the mixed layer, and is inversely proportional to the Richardson number of the thermocline. These are consistent with the qualitative results in the linear stability analysis. When the mixed layer is deep or the thermocline Richardson number is small, the w mode of mixed layer instability can extend deeper into the thermocline, causing thermocline water from a higher depth to be entrained into the mixed layer.

Figure 4.7b also shows the dependence of the product on Ri_m —the product increases with increasing Ri_m , which is ostensibly inconsistent with the finding in the linear stability analysis that the variance of the vertical displacement of the mixed layer base is independent of Ri_m . This discrepancy is due to the fact that normalizing the horizontally averaged column-integrated eddy energy to $\rho_0 \Lambda^2 h_m^3$ in the linear stability analysis does not precisely track the moment when the linear phase transitions into the nonlinear phase. Figure 4.8a shows the time series of the horizontally averaged column integrated EKE in the nonlinear simulations, as nondimensionalized against $\rho_0 \Lambda^2 h_m^3$. The nondimensionalized EKE first exponentially increases with time and then levels off at the transition point between the linear phase and the nonlinear phase. With the same Ri_t , the EKE in the nonlinear phase increases with Ri_m . Since the fraction of EKE in eddy energy is similar in different cases (ranging from 0.25 to 0.37), the eddy energy in the nonlinear phase also increases with Ri_m . This means that when normalizing the horizontally averaged column-integrated eddy energy to $\rho_0 \Lambda^2 h_m^3$ in the linear stability analysis (the horizontal dashed line in Fig. 4.8a), the oscillation amplitude is overestimated in the small- Ri_m cases and is underestimated in the large- Ri_m cases.

A scaling for the dependence of the energy at the transition point on Ri_m is provided below: The criterion for the transition from the linear phase to the nonlinear phase is $\zeta/f \sim 1$ (Fig. 4.8b), where ζ is the relative vorticity

$$\zeta \sim \frac{u}{L}$$

where u is the perturbation horizontal velocity and L is the horizontal length scale. Due to non-QG effects, the horizontal length scale depends on Ri_m (Stone, 1966):

$$L = \frac{2\pi}{k_{max}} \approx \frac{2\pi N_m h_m}{f} \left(\frac{1 + 1/Ri_m}{5/2} \right)^{1/2}$$

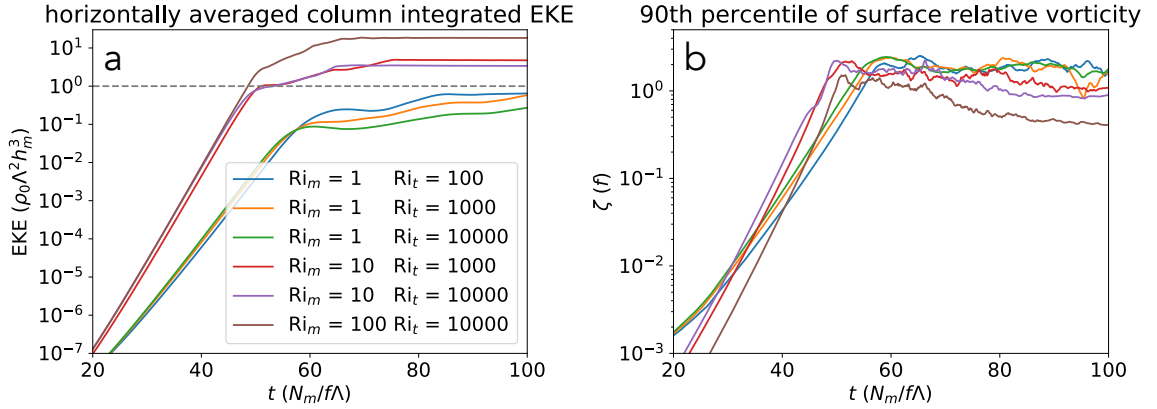


Figure 4.8. The transition from the linear phase to the nonlinear phase happens when the surface relative vorticity reaches f and the eddy kinetic energy reaches different levels, which depend on the Richardson number of the mixed layer. Shown are the time series of (a) the horizontal mean vertically integrated eddy kinetic energy in the nonlinear simulations and (b) the 90th percentile of the relative vorticity at the surface ($z = 0.5$).

Plugging $u = \Lambda h_m u'$ and the expression of L in the expression of relative vorticity, we get

$$\zeta \sim \frac{\Lambda f u'}{2\pi N_m} \left(\frac{5/2}{1 + 1/Ri_m} \right)^{1/2}$$

Solving $\zeta/f \sim 1$ for u' , we get u' increasing with Ri_m :

$$u' \propto (Ri_m + 1)^{1/2}$$

Therefore, the nondimensionalized energy, and its column integral at the transition point scale with $Ri_m + 1$. Figures 4.4d shows that if the nondimensionalized column-integrated energy is normalized to the same value, the variance of the displacement of the mixed layer base has no dependence on Ri_m . Since the nondimensionalized column-integrated energy at

the transition point increases with Ri_m , the variance of the displacement of the mixed layer base at the transition point also increases with Ri_m , leading to stronger vertical exchange at higher Ri_m .

The slope of the exponential growth of EKE in Fig. 4.8 is different with different Ri_m due to the modifications of non-QG dynamics to the growth rate of baroclinic instability (Stone, 1966).

4.5 Discussion and summary

In the nonlinear simulations, an artificial hyperviscosity that dampens variations on small spatial scales that accumulates during the forward cascade of energy is indispensable for stabilizing the model. The magnitude of the hyperviscosity, measured by the reciprocal of the Reynolds number, must be appropriate, such that the artificial diffusion of momentum, buoyancy, and tracer is minor to the advection and meanwhile the model always stays numerically stable. With a higher model resolution, smaller-scale flow can be resolved, and the hyperviscosity required by numerical stability can be smaller. We have chosen the largest Reynolds number required by the current model resolution, with which the PV budget in the mixed layer is closed (which is used as an indicator for model stability). A Reynolds number of 10^4 is deemed sufficient, and the findings in this study are believed to be robust with respect to different, sufficiently large Reynolds numbers.

Effectively, the diffusive fluxes of tracer introduced by the artificial diffusivity and viscosity elevate the base of the mixed layer and reduce the thickness of the mixed layer, as shown in Fig. 4.9. The leftmost column in Fig. 4.9 shows the nondimensionalized advective upward flux of tracer, wc . The second column shows the nondimensionalized diffusive upward flux of tracer, $-v\partial c/\partial z$. The third column shows the nondimensionalized advective upward flux of hydrostatic PV. The fourth column shows the nondimensionalized diffusive upward flux of PV. The rightmost column shows the nondimensionalized viscous upward flux of PV. In the linear phase, diffusive fluxes of the thermocline tracer and hydrostatic PV dominate, elevating the base of the mixed layer to different depths, depending on the ratio of Ri_t to Ri_m . After the transition point, advective fluxes dominate in the mixed layer above the

elevated bottom. Figure 4.10 shows that in the nonlinear phase, the thermocline tracer and hydrostatic PV are both almost homogenous in the vertical direction in the mixed layer, so the level $z = 0.1 h_m$ (which is slightly higher than the initial base of the mixed layer, $z = 0$) is chosen to represent the mixed layer in terms of tracer concentration.

Diffusion elevates the base of the mixed layer to different depths at different ratios of Ri_t/Ri_m (Fig. 4.9, second column and fourth column). Larger Ri_t/Ri_m results in a higher elevation, and thinner “effective mixed layer” in the nonlinear phase where entrained thermocline tracer and PV can be homogenized by submesoscale eddies. With the same amount of thermocline water entrained into the mixed layer, a thinner mixed layer results in a higher concentration of thermocline water, which explains why the product of the average binary tracer concentration in the mixed layer and the initial difference PV difference between the mixed layer and thermocline for the same Ri_m increases with increasing Ri_t in Fig. 4.7b.

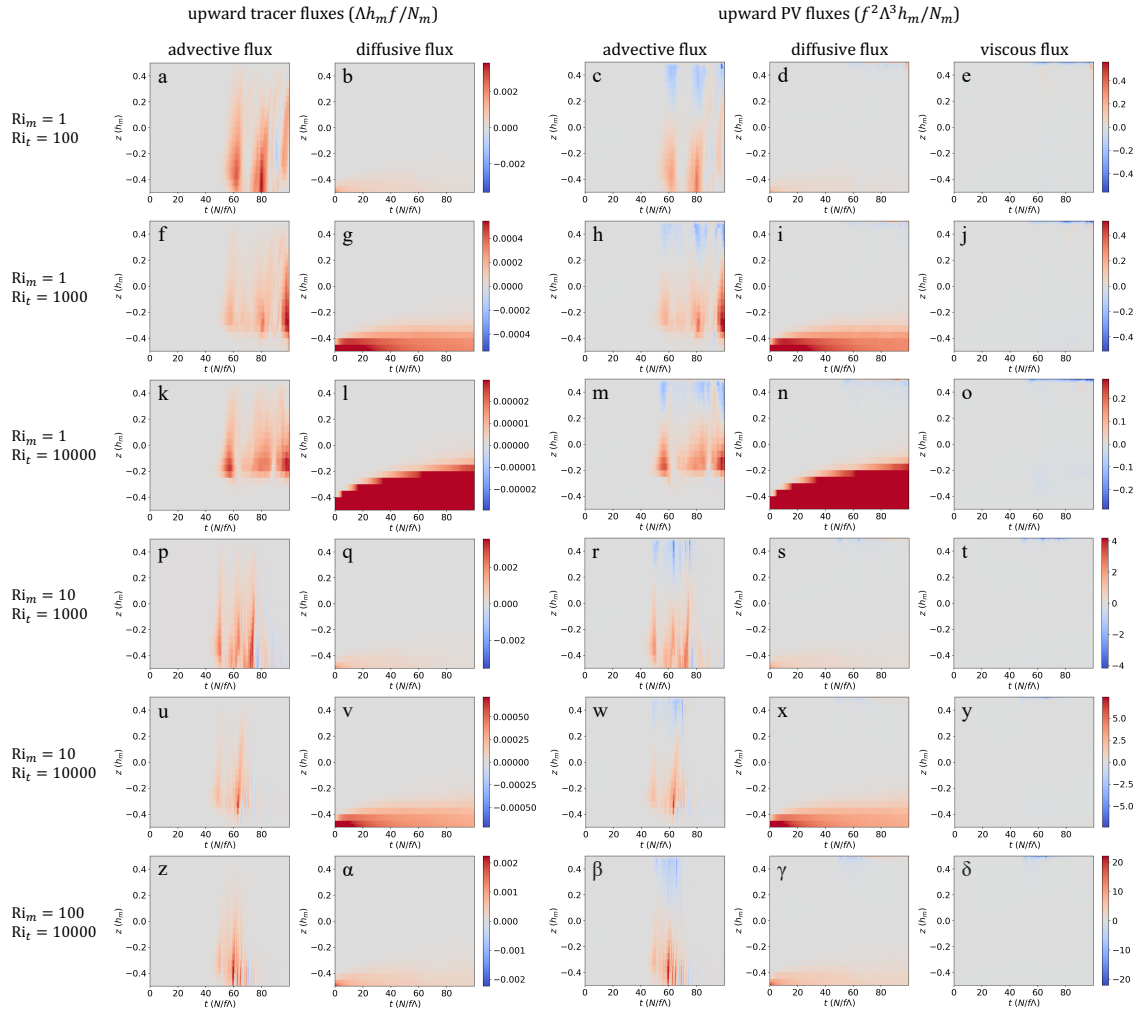


Figure 4.9. In the nonlinear phase of the instability development, advective fluxes dominate in the vertical transport of the binary tracer and PV above the “effective” base of the mixed layer that is elevated by diffusion. Shown are the horizontally averaged upward fluxes of the binary tracer and PV within the mixed layer as functions of time and depth. Each row shows one simulation, with the Richardson numbers of the simulation indicated on the left. The left two columns show the two terms of the upward tracer flux, with the two plots in the same row sharing the same colorbar. The right three columns show the three terms of the upward PV flux, with the three plots in the same row sharing the same colorbar. The colors show nondimensionalized fluxes, with their dimensions shown at the top of the figure.

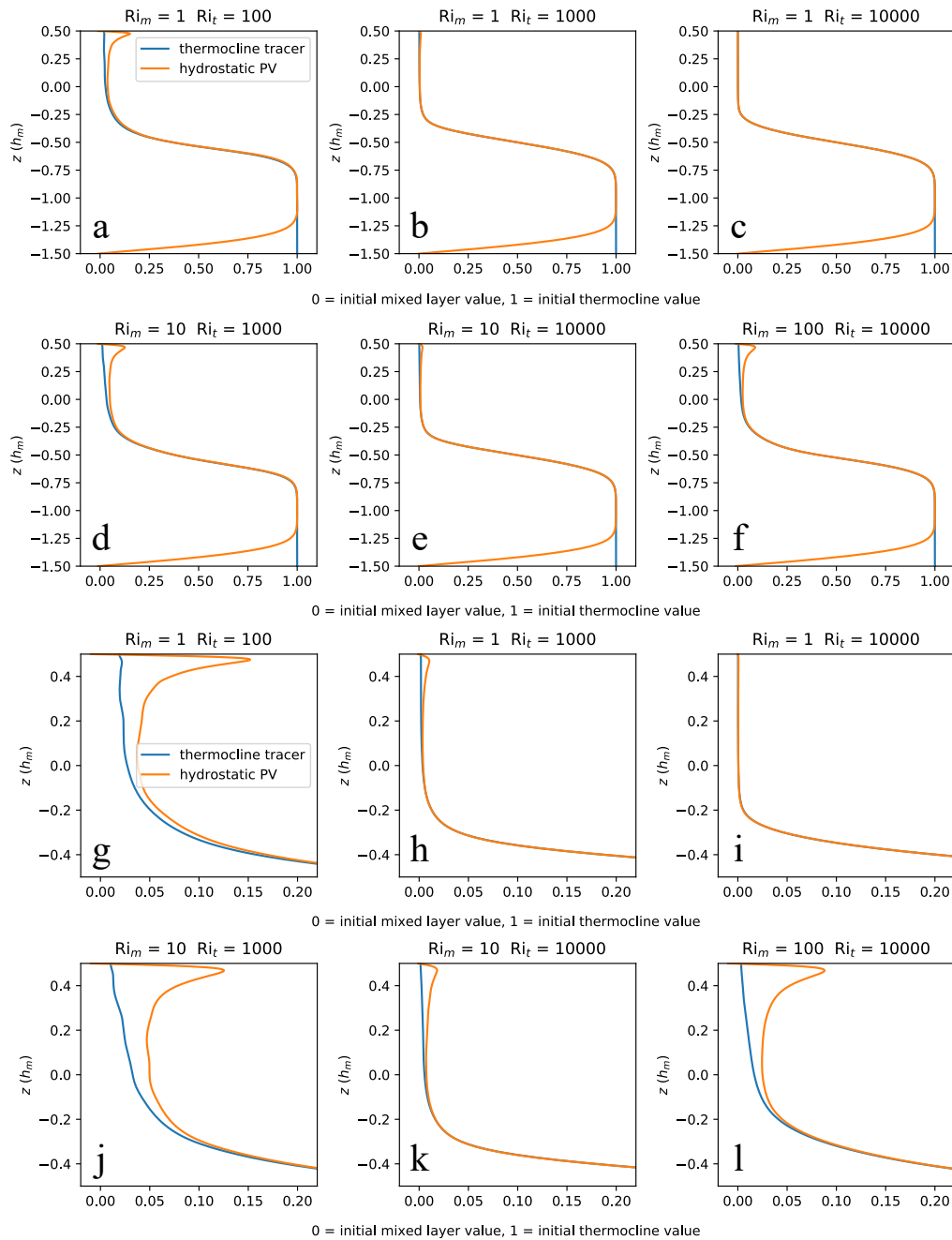


Figure 4.10. In the nonlinear phase, the binary tracer concentration and hydrostatic PV are homogenized by eddies in the mixed layer. Shown are the horizontally averaged binary tracer concentration (blue curves) and hydrostatic PV (orange curves) at $t = 70 N_m / f \Lambda$. (a–f) Vertical profiles in both the initial mixed layer and the initial thermocline. (g–l) Vertical profiles in the initial mixed layer. The Richardson numbers are shown above each panel. Both the binary tracer concentration and the PV are normalized such that the initial values in the mixed layer are equal to 0 and the initial values in the thermocline are equal to 1. Both the horizontally averaged binary tracer concentration and hydrostatic PV are roughly homogeneous between $z = -0.1 h_m$ and $z = 0.3 h_m$. That is the reason why $z = 0.1 h_m$ is chosen to represent the whole mixed layer in terms of the binary tracer concentration in Fig. 4.7.

In this study, we develop a scaling law for how the vertical exchange between the mixed layer and the thermocline energized by mixed layer instability depend on environmental parameters. In an idealized configuration, we perform linear stability analysis and nonlinear simulations based on non-QG equations to investigate the linear phase and the nonlinear phase of the instability development, respectively. We find that mixed layer instability can induce vertical velocity in the shallow thermocline, which deforms the interface between the mixed layer and the thermocline and finally causes thermocline water to be entrained into the interior of the mixed layer. Mixed layer instability can induce vertical velocity deeper into the thermocline when the mixed layer is thicker or the thermocline Richardson number is smaller. The induced vertical velocity at the base of the mixed layer is stronger when the thermocline Richardson number is smaller. We propose a scaling law that the vertical exchange between the mixed layer and the thermocline, characterized by how much thermocline water is entrained into the mixed layer, is proportional to the mixed layer depth and inversely proportional to the thermocline Richardson number. The vertical exchange also increases with an increasing mixed layer Richardson number. Our results imply that the tracer exchange between the mixed layer and the thermocline is more efficient when the mixed layer is deeper, the lateral buoyancy gradient is larger, the thermocline stratification is weaker, and the mixed layer stratification is stronger. Parameterization based on the scaling law proposed in this paper can potentially be implemented in ocean general circulation models. The scaling laws suggest vigorous exchange between deep mixed layers and the permanent thermocline in winter and between the mixed layer and weakly stratified thermocline in mode water formation zones.

Chapter 5

Conclusions

The three chapters of this thesis have discussed three examples of how 3D modeling transcends the limitations of 1D modeling and reveals new solutions, phenomena, and scalings in planetary atmospheres and Earth's ocean. Altogether, they have demonstrated the usefulness of 3D thinking and 3D models in solving problems, discovering new phenomena, and developing theories in the context of the atmosphere-ocean systems on planets. It is the author's intention to encourage the applications of 3D models in photochemical modeling for (exo)planets and theoretical studies in ocean science with the rise in computational power through time. 3D models may help solve long standing problems and make innovations in planetary science, atmospheric science, and ocean science. Below are the major findings in each chapter and the author's recommendations for future directions.

Chapter 2:

The inconsistency between the results of the near-surface *in situ* methane measurements and the satellite remote sensing measurements on Mars can be reconciled if and only if an active methane emission hot spot is located in the immediate vicinity of the *Curiosity* rover in northwestern Gale crater or unknown physical or chemical processes are rapidly removing methane. The transport and dispersion of methane plumes should be modelled properly with 3D models. To completely solve the various puzzles with methane on Mars, Mars missions in the near future should still regard real-time observations for methane as one of their priorities. Novel observational techniques using novel observational geometries should be considered, such as instruments that land on Aeolis Mons overlooking the crater floor of Gale, instruments that land on the crater floor measuring scattered light from the zenith, and a network of small landers with methane sensors that can conduct synergistic observations at Gale. These observational techniques potentially have a better chance to detect methane as they can examine the regions that are the closest to methane emission sites. Advances in

atmospheric modeling will also be useful, such as reproducing winds that are more consistent with observations in Mars GCMs, etc.

Chapter 3:

Under certain conditions, large-magnitude self-sustained photochemical oscillations can take place in the atmospheres of terrestrial planets. The resulting large temporal variability in ozone abundance on exoplanets, if observed, may suggest a strong surface NO_x emission source, which could signal extrasolar life participating in the nitrogen cycle on exoplanets. Fully coupled, 3D atmospheric chemistry-radiation-dynamics models can reveal new phenomena that may not exist in 1D models, and hence they are demonstrated to be powerful tools for future planetary atmospheric research. The author recommends more applications of such 3D models in studying planetary and exoplanetary atmospheres, which are still lacking to date due to computing costs. Developing non-Earth-centric 3D models will be very helpful in advancing our understanding in diverse atmospheres of planets and exoplanets, including reduced atmospheres, hazy atmospheres, and thick atmospheres, etc.

Chapter 4:

Submesoscale turbulence energized by baroclinic instability in the ocean mixed layer can induce exchange between the surface ocean and the ocean interior. Various environmental physical parameters affect the exchange rate. The exchange is stronger where the ocean mixed layer is thicker, the Richardson number of the thermocline is smaller, and the Richardson number of ocean mixed layer is larger. The associated nutrient supply from the ocean interior to the surface ocean is also expected to be stronger under these conditions, potentially leading to higher primary productivity of marine life. Subsequent work may include testing the proposed scaling laws against observations and the implementation of the proposed scaling laws in ocean models. The physics revealed in this chapter could also supplement and improve existing theories on mixed layer restratification from the perspective of potential vorticity that is entrained from the thermocline.

BIBLIOGRAPHY

- Allen, M., et al. (1981). Vertical transport and photochemistry in the terrestrial mesosphere and lower thermosphere (50–120 km). *Journal of Geophysical Research: Space Physics*, **86**(A5), 3617–3627. doi: 10.1029/JA086iA05p03617.
- Aoki, S., et al. (2018). Stringent upper limit of CH₄ on Mars based on SOFIA/EXES observations. *Astronomy and Astrophysics*, **610**, A78. doi: 10.1051/0004-6361/201730903.
- Bachman, S. D., B. et al. (2017). Parameterization of frontal symmetric instabilities. I: Theory for resolved fronts. *Ocean Modelling*, **109**, 72–95. doi: 10.1016/j.ocemod.2016.12.003.
- Balwada, D., et al. (2018). Submesoscale vertical velocities enhance tracer subduction in an idealized Antarctic Circumpolar Current. *Geophysical Research Letters*, **45**(18), 9790–9802. doi: 10.1029/2018GL079244.
- Barragán, O., et al. (2018). K2-141 b. A 5-M \oplus super-Earth transiting a K7 V star every 6.7 h. *Astronomy & Astrophysics*, **612**, A95. doi: 10.1051/0004-6361/201732217.
- Barstow, J. K., & Irwin, P. G. (2016). Habitable worlds with JWST: Transit spectroscopy of the TRAPPIST-1 system?. *Monthly Notices of the Royal Astronomical Society: Letters*, **461**(1), L92–L96. doi: 10.1093/mnrasl/slw109.
- Batalha, N. E., et al. (2018). Strategies for constraining the atmospheres of temperate terrestrial planets with JWST. *The Astrophysical Journal Letters*, **856**(2), L34. doi: 10.3847/2041-8213/aab896.
- Boccaletti, G., et al. (2007). Mixed layer instabilities and restratification. *Journal of Physical Oceanography*, **37**(9), 2228–2250. doi: 10.1175/JPO3101.1.
- Bouwman, A. F., et al. (2002). Emissions of N₂O and NO from fertilized fields: Summary of available measurement data. *Global Biogeochemical Cycles*, **16**(4), 6–1. doi: 10.1029/2001GB001811.
- Braam, M., et al. (2022). Lightning-induced chemistry on tidally-locked Earth-like exoplanets. *Monthly Notices of the Royal Astronomical Society*, **517**(2), 2383–2402. doi: 10.1093/mnras/stac2722.
- Burns, K. J., et al. (2020). Dedalus: A flexible framework for numerical simulations with spectral methods. *Physical Review Research*, **2**(2), 023068. doi: 10.1103/PhysRevResearch.2.023068.
- Callies, J., et al. (2015). Seasonality in submesoscale turbulence. *Nature Communications*, **6**(1), 1–8. doi: 10.1038/ncomms7862.
- Callies, J., et al. (2016). The role of mixed-layer instabilities in submesoscale turbulence. *Journal of Fluid Mechanics*, **788**, 5–41. doi: 10.1017/jfm.2015.700.
- Callies, J., & Ferrari, R. (2018). Baroclinic instability in the presence of convection. *Journal of Physical Oceanography*, **48**(1), 45–60. doi: 10.1175/JPO-D-17-0028.1.

- Chen, H., et al. (2018). Biosignature anisotropy modeled on temperate tidally locked M-dwarf planets. *The Astrophysical Journal Letters*, **868**(1), L6. doi: 10.3847/2041-8213/aaedb2.
- Chen, H., et al. (2019). Habitability and spectroscopic observability of warm M-dwarf exoplanets evaluated with a 3D chemistry-climate model. *The Astrophysical Journal*, **886**(1), 16. doi: 10.3847/1538-4357/ab4f7e.
- Chen, H., et al. (2021). Persistence of flare-driven atmospheric chemistry on rocky habitable zone worlds. *Nature Astronomy*, **5**(3), 298–310. doi: 10.1038/s41550-020-01264-1.
- Christensen, P. R., et al. (2001). Mars Global Surveyor Thermal Emission Spectrometer experiment: Investigation description and surface science results. *Journal of Geophysical Research: Planets*, **106**(E10), 23823–23871. doi: 10.1029/2000JE001370.
- Cicerone, R. J., & Oremland, R. S. (1988). Biogeochemical aspects of atmospheric methane. *Global Biogeochemical Cycles*, **2**(4), 299–327. doi: 10.1029/GB002i004p00299.
- Cohen, M., et al. (2022). Longitudinally asymmetric stratospheric oscillation on a tidally locked exoplanet. *The Astrophysical Journal*, **930**(2), 152. doi: 10.3847/1538-4357/ac625d.
- Cooke, G. J., et al. (2022). A revised lower estimate of ozone columns during Earth's oxygenated history. *Royal Society open science*, **9**(1), 211165. doi: 10.1098/rsos.211165.
- de Boyer Montégut, C., et al. (2004). Mixed layer depth over the global ocean: An examination of profile data and a profile-based climatology. *Journal of Geophysical Research: Oceans*, **109**(C12). doi: 10.1029/2004JC002378.
- Draxler, R. R., & Hess, G. D. (1998). An overview of the HYSPLIT_4 modelling system for trajectories. *Australian Meteorological Magazine*, **47**(4), 295–308.
- Eady, E. T. (1949). Long waves and cyclone waves. *Tellus*, **1**(3), 33–52. doi: 10.3402/tellusa.v1i3.8507.
- Emmons, L. K., et al. (2010). Description and evaluation of the Model for Ozone and Related chemical Tracers, version 4 (MOZART-4). *Geoscientific Model Development*, **3**(1), 43–67. doi: 10.5194/gmd-3-43-2010.
- Fasoli, B., et al. (2018). Simulating atmospheric tracer concentrations for spatially distributed receptors: Updates to the Stochastic Time-Inverted Lagrangian Transport model's R interface (STILT-R version 2). *Geoscientific Model Development*, **11**(7), 2813–2824. doi: 10.5194/gmd-11-2813-2018.
- Faucher, T. J., et al. (2019). Impact of clouds and hazes on the simulated JWST transmission spectra of habitable zone planets in the TRAPPIST-1 system. *The Astrophysical Journal*, **887**(2), 194. doi: 10.3847/1538-4357/ab5862.
- Feigin, A. M., & Konovalov, I. B. (1996). On the possibility of complicated dynamic behavior of atmospheric photochemical systems: Instability of the Antarctic photochemistry during the ozone hole formation. *Journal of Geophysical Research: Atmospheres*, **101**(D20), 26023–26038. doi: 10.1029/96JD02011.

- Feigin, A. M., et al. (1998). Toward an understanding of the nonlinear nature of atmospheric photochemistry: Essential dynamic model of the mesospheric photochemical system. *Journal of Geophysical Research: Atmospheres*, **103**(D19), 25447–25460. doi: 10.1029/98JD01569.
- Field, C. B., et al. (1998). Primary production of the biosphere: Integrating terrestrial and oceanic components. *Science*, **281**(5374), 237–240. doi: 10.1126/science.281.5374.237.
- Field, R. J., et al. (2001). Characterization of oscillation and a period-doubling transition to chaos reflecting dynamic instability in a simplified model of tropospheric chemistry. *Journal of Geophysical Research: Atmospheres*, **106**(D7), 7553–7565. doi: 10.1029/2000JD900638.
- Fonseca, R. M., et al. (2018). Planetary boundary layer and circulation dynamics at Gale Crater, Mars. *Icarus*, **302**, 537–559. doi: 10.1016/j.icarus.2017.11.036.
- Fonti, S., & Marzo, G. A. (2010). Mapping the methane on Mars. *Astronomy & Astrophysics*, **512**, A51. doi: 10.1051/0004-6361/200913178.
- Formisano, V., et al. (2004). Detection of methane in the atmosphere of Mars. *Science*, **306**(5702), 1758–1761. doi: 10.1126/science.1101732.
- Fox-Kemper, B., et al. (2008). Parameterization of mixed layer eddies. Part I: Theory and diagnosis. *Journal of Physical Oceanography*, **38**(6), 1145–1165. doi: 10.1175/2007JPO3792.1.
- Fox-Kemper, B., & Ferrari, R. (2008). Parameterization of mixed layer eddies. Part II: Prognosis and impact. *Journal of Physical Oceanography*, **38**(6), 1166–1179. doi: 10.1175/2007JPO3788.1.
- Fox-Kemper, B., et al. (2011). Parameterization of mixed layer eddies. III: Implementation and impact in global ocean climate simulations. *Ocean Modelling*, **39**(1-2), 61–78. doi: 10.1016/j.ocemod.2010.09.002.
- Freedman, R. S., et al. (2008). Line and mean opacities for ultracool dwarfs and extrasolar planets. *The Astrophysical Journal Supplement Series*, **174**(2), 504. doi: 10.1086/521793.
- Freedman, R. S., et al. (2014). Gaseous mean opacities for giant planet and ultracool dwarf atmospheres over a range of metallicities and temperatures. *The Astrophysical Journal Supplement Series*, **214**(2), 25. doi: 10.1088/0067-0049/214/2/25.
- Garner, S. T., et al. (1992). Nonlinear equilibration of two-dimensional Eady waves: A new perspective. *Journal of Atmospheric Sciences*, **49**(21), 1984–1996. doi: 10.1175/1520-0469(1992)049%3c1984:NEOTDE%3e2.0.CO;2.
- Geminale, A., et al. (2008). Methane in Martian atmosphere: Average spatial, diurnal, and seasonal behaviour. *Planetary and Space Science*, **56**(9), 1194–1203. doi: 10.1016/j.pss.2008.03.004.
- Gerbig, C., et al. (2003). Toward constraining regional-scale fluxes of CO₂ with atmospheric observations over a continent: 2. Analysis of COBRA data using a receptor-oriented framework. *Journal of Geophysical Research: Atmospheres*, **108**(D24). doi: 10.1029/2003JD003770.

- Gillon, M., et al. (2017). Seven temperate terrestrial planets around the nearby ultracool dwarf star TRAPPIST-1. *Nature*, **542**(7642), 456–460. doi: 10.1038/nature21360.
- Giuranna, M., et al. (2019). Independent confirmation of a methane spike on Mars and a source region east of Gale Crater. *Nature Geoscience*, **12**(5), 326–332. doi: 10.1038/s41561-019-0331-9.
- Gough, R. V., et al. (2010). Methane adsorption on a Martian soil analog: An abiogenic explanation for methane variability in the Martian atmosphere. *Icarus*, **207**(1), 165–174. doi: 10.1016/j.icarus.2009.11.030.
- Grenfell, J. L., et al. (2022). Atmospheric processes affecting methane on Mars. *Icarus*, **382**, 114940. doi: 10.1016/j.icarus.2022.114940.
- Grotzinger, J. P., et al. (2015). Deposition, exhumation, and paleoclimate of an ancient lake deposit, Gale crater, Mars. *Science*, **350**(6257). doi: 10.1126/science.aac7575.
- Guzewich, S. D., et al. (2013). High-altitude dust layers on Mars: Observations with the Thermal Emission Spectrometer. *Journal of Geophysical Research: Planets*, **118**(6), 1177–1194. doi: 10.1002/jgre.20076.
- Guzewich, S. D., et al. (2014). Thermal tides during the 2001 Martian global-scale dust storm. *Journal of Geophysical Research: Planets*, **119**(3), 506–519. doi: 10.1002/2013JE004502.
- Haine, T. W., & Marshall, J. (1998). Gravitational, symmetric, and baroclinic instability of the ocean mixed layer. *Journal of Physical Oceanography*, **28**(4), 634–658. doi: 10.1175/1520-0485(1998)028%3c0634:GSABIO%3e2.0.CO;2.
- Hanna, S. R. (1984). Applications in air pollution modeling. In *Atmospheric turbulence and air pollution modelling* (pp. 275-310). Springer, Dordrecht. doi: 10.1007/978-94-010-9112-1_7.
- Hasson, A. S., & Manor, R. E. (2003). Steady-state instability in tropospheric chemical mechanisms. *Atmospheric Environment*, **37**(34), 4735–4745. doi: 10.1016/j.atmosenv.2003.08.018.
- Hess, P. G., & Madronich, S. (1997). On tropospheric chemical oscillations. *Journal of Geophysical Research: Atmospheres*, **102**(D13), 15949–15965. doi: 10.1029/97JD00526.
- Hébrard, E., et al. (2012). An aerodynamic roughness length map derived from extended Martian rock abundance data. *Journal of Geophysical Research: Planets*, **117**(E4). doi: 10.1029/2011JE003942.
- Hu, R., et al. (2016). Hypotheses for near-surface exchange of methane on Mars. *Astrobiology*, **16**(7), 539–550. doi: 10.1089/ast.2015.1410.
- Kalachev, L. V., & Field, R. J. (2001). Reduction of a model describing ozone oscillations in the troposphere: Example of an algorithmic approach to model reduction in atmospheric chemistry. *Journal of Atmospheric Chemistry*, **39**(1), 65–93. doi: 10.1023/A:1010649217616.

- Kasting, J. F., & Ackerman, T. P. (1985). High atmospheric NO_x levels and multiple photochemical steady states. *Journal of Atmospheric Chemistry*, **3**(3), 321–340. doi: 10.1007/BF00122522.
- Kempton, E. M. R., et al. (2017). Exo-Transmit: An open-source code for calculating transmission spectra for exoplanet atmospheres of varied composition. *Publications of the Astronomical Society of the Pacific*, **129**(974), 044402. doi: 10.1088/1538-3873/aa61ef.
- Kite, E. S., et al. (2017). Methane bursts as a trigger for intermittent lake-forming climates on post-Noachian Mars. *Nature Geoscience*, **10**(10), 737–740. doi: 10.1038/ngeo3033.
- Knak Jensen, S. J., et al. (2014). A sink for methane on Mars? The answer is blowing in the wind. *Icarus*, **236**, 24–27. doi: 10.1016/j.icarus.2014.03.036.
- Knutsen, E. W., et al. (2021). Comprehensive investigation of Mars methane and organics with ExoMars/NOMAD. *Icarus*, **357**, 114266. doi: 10.1016/j.icarus.2020.114266.
- Konovalov, I. B., et al. (1999). Toward understanding of the nonlinear nature of atmospheric photochemistry: Multiple equilibrium states in the high-latitude lower stratospheric photochemical system. *Journal of Geophysical Research: Atmospheres*, **104**(D3), 3669–3689. doi: 10.1029/1998JD100037.
- Konovalov, I. B., & Feigin, A. M. (2000). Toward an understanding of the nonlinear nature of atmospheric photochemistry: Origin of the complicated dynamic behaviour of the mesospheric photochemical system. *Nonlinear Processes in Geophysics*, **7**(1/2), 87–104. doi: 10.5194/npg-7-87-2000.
- Korablev, O., et al. (2019). No detection of methane on Mars from early ExoMars Trace Gas Orbiter observations. *Nature*, **568**(7753), 517–520. doi: 10.1038/s41586-019-1096-4.
- Kort, E. A., et al. (2008). Emissions of CH₄ and N₂O over the United States and Canada based on a receptor-oriented modeling framework and COBRA-NA atmospheric observations. *Geophysical Research Letters*, **35**(18). doi: 10.1029/2008GL034031.
- Krasnopolsky, V. A. (2012). Search for methane and upper limits to ethane and SO₂ on Mars. *Icarus*, **217**(1), 144–152. doi: 10.1016/j.icarus.2011.10.019.
- Krasnopolsky, V. A., et al. (2004). Detection of methane in the Martian atmosphere: Evidence for life?. *Icarus*, **172**(2), 537–547. doi: 10.1016/j.icarus.2004.07.004.
- Krissansen-Totton, J., et al. (2018). Detectability of biosignatures in anoxic atmospheres with the James Webb Space Telescope: A TRAPPIST-1e case study. *The Astronomical Journal*, **156**(3), 114. doi: 10.3847/1538-3881/aad564.
- Krol, M. C. (1995). Comment on “Multiple steady states in atmospheric chemistry” by Richard W. Stewart. *Journal of Geophysical Research: Atmospheres*, **100**(D6), 11699–11702. doi: 10.1029/95JD00846.
- Krol, M. C., & Poppe, D. (1998). Nonlinear dynamics in atmospheric chemistry rate equations. *Journal of Atmospheric Chemistry*, **29**(1), 1–16. doi: 10.1023/A:1005843430146.

- Lamarque, J. F., et al. (2010). Historical (1850–2000) gridded anthropogenic and biomass burning emissions of reactive gases and aerosols: Methodology and application. *Atmospheric Chemistry and Physics*, **10**(15), 7017–7039. doi: 10.5194/acp-10-7017-2010.
- Large, W. G., et al. (1994). Oceanic vertical mixing: A review and a model with a nonlocal boundary layer parameterization. *Reviews of Geophysics*, **32**(4), 363–403. doi: 10.1029/94RG01872.
- Lee, C., et al. (2011). Demonstration of ensemble data assimilation for Mars using DART, MarsWRF, and radiance observations from MGS TES. *Journal of Geophysical Research: Planets*, **116**(E11). doi: 10.1029/2011JE003815.
- Lefèvre, F., & Forget, F. (2009). Observed variations of methane on Mars unexplained by known atmospheric chemistry and physics. *Nature*, **460**(7256), 720–723. doi: 10.1038/nature08228.
- Léger, A., et al. (1993). Search for primitive life on a distant planet: Relevance of O₂ and O₃ detections. *Astronomy and Astrophysics*, **277**, 309.
- Lévy, M., et al. (2001). Impact of sub-mesoscale physics on production and subduction of phytoplankton in an oligotrophic regime. *Journal of Marine Research*, **59**(4), 535–565. doi: 10.1357/002224001762842181.
- Lévy, M., et al. (2012a). Bringing physics to life at the submesoscale. *Geophysical Research Letters*, **39**(14). doi: 10.1029/2012GL052756.
- Lévy, M., et al. (2012b). Large-scale impacts of submesoscale dynamics on phytoplankton: Local and remote effects. *Ocean Modelling*, **43**, 77–93. doi: 10.1016/j.ocemod.2011.12.003.
- Lévy, M., et al. (2018). The role of submesoscale currents in structuring marine ecosystems. *Nature Communications*, **9**(1), 1–16. doi: 10.1038/s41467-018-07059-3.
- Lin, J. C., et al. (2003). A near-field tool for simulating the upstream influence of atmospheric observations: The Stochastic Time-Inverted Lagrangian Transport (STILT) model. *Journal of Geophysical Research: Atmospheres*, **108**(D16). doi: 10.1029/2002JD003161.
- Lin, J. C., et al. (2004). Measuring fluxes of trace gases at regional scales by Lagrangian observations: Application to the CO₂ Budget and Rectification Airborne (COBRA) study. *Journal of Geophysical Research: Atmospheres*, **109**(D15). doi: 10.1029/2004JD004754.
- Lin, J. C., et al. (2012). Lagrangian Modeling of the Atmosphere. *Geophysical Monograph Series*, **200**, 349. doi: 10.1029/GM200.
- Lincowski, A. P., et al. (2018). Evolved climates and observational discriminants for the TRAPPIST-1 planetary system. *The Astrophysical Journal*, **867**(1), 76. doi: 10.3847/1538-4357/aae36a.
- Luo, Y., et al. (2021). Mars methane sources in northwestern Gale crater inferred from back trajectory modeling. *Earth and Space Science*, **8**(11), e2021EA001915. doi: 10.1029/2021EA001915.

- Lupu, R. E., et al. (2014). The atmospheres of earthlike planets after giant impact events. *The Astrophysical Journal*, **784**(1), 27. doi: 10.1088/0004-637X/784/1/27.
- Lustig-Yaeger, J., et al. (2019). The detectability and characterization of the TRAPPIST-1 exoplanet atmospheres with JWST. *The Astronomical Journal*, **158**(1), 27. doi: 10.3847/1538-3881/ab21e0.
- Lyons, T. W., et al. (2014). The rise of oxygen in Earth's early ocean and atmosphere. *Nature*, **506**(7488), 307–315. doi: 10.1038/nature13068.
- Macatangay, R., et al. (2008). A framework for comparing remotely sensed and in-situ CO₂ concentrations. *Atmospheric Chemistry and Physics*, **8**(9), 2555–2568. doi: 10.5194/acp-8-2555-2008.
- Mahadevan, A., & Archer, D. (2000). Modeling the impact of fronts and mesoscale circulation on the nutrient supply and biogeochemistry of the upper ocean. *Journal of Geophysical Research: Oceans*, **105**(C1), 1209–1225. doi: 10.1029/1999JC900216.
- Mahadevan, A. (2006). Modeling vertical motion at ocean fronts: Are nonhydrostatic effects relevant at submesoscales?. *Ocean Modelling*, **14**(3–4), 222–240. doi: 10.1016/j.ocemod.2006.05.005.
- Mahadevan, A., & Tandon, A. (2006). An analysis of mechanisms for submesoscale vertical motion at ocean fronts. *Ocean Modelling*, **14**(3–4), 241–256. doi: 10.1016/j.ocemod.2006.05.006.
- Mahadevan, A., et al. (2010). Rapid changes in mixed layer stratification driven by submesoscale instabilities and winds. *Journal of Geophysical Research: Oceans*, **115**(C3). doi: 10.1029/2008JC005203.
- Mahadevan, A. (2014). Eddy effects on biogeochemistry. *Nature*, **506**(7487), 168–169. doi: 10.1038/nature13048.
- Mahadevan, A. (2016). The impact of submesoscale physics on primary productivity of plankton. *Annual Review of Marine Science*, **8**, 161–184. doi: 10.1146/annurev-marine-010814-015912.
- Mahaffy, P. R., et al. (2012). The sample analysis at Mars investigation and instrument suite. *Space Science Reviews*, **170**(1), 401–478. doi: 10.1007/s11214-012-9879-z.
- Mallia, D. V., et al. (2015). Impacts of upwind wildfire emissions on CO, CO₂, and PM_{2.5} concentrations in Salt Lake City, Utah. *Journal of Geophysical Research: Atmospheres*, **120**(1), 147–166. doi: 10.1002/2014JD022472.
- Manabe, S., & Stouffer, R. J. (1980). Sensitivity of a global climate model to an increase of CO₂ concentration in the atmosphere. *Journal of Geophysical Research: Oceans*, **85**(C10), 5529–5554. doi: 10.1029/JC085iC10p05529.
- Marcq, E., et al. (2013). Variations of sulphur dioxide at the cloud top of Venus's dynamic atmosphere. *Nature Geoscience*, **6**(1), 25–28. doi: 10.1038/ngeo1650.
- Marsh, D. R., et al. (2013). Climate change from 1850 to 2005 simulated in CESM1 (WACCM). *Journal of Climate*, **26**(19), 7372–7391. doi: 10.1175/JCLI-D-12-00558.1.

- McWilliams, J. C. (2016). Submesoscale currents in the ocean. *Proceedings of the Royal Society A: Mathematical, Physical and Engineering Sciences*, **472**(2189), 20160117. doi: 10.1098/rspa.2016.0117.
- McWilliams, J. C. (2021). Oceanic frontogenesis. *Annual Review of Marine Science*, **13**, 227–253. doi: 10.1146/annurev-marine-032320-120725.
- Meadows, V. S. (2017). Reflections on O₂ as a biosignature in exoplanetary atmospheres. *Astrobiology*, **17**(10), 1022–1052. doi: 10.1089/ast.2016.1578.
- Meier Valdés, E., et al. (2022). Weak evidence for variable occultation depth of 55 Cnc e with TESS. *Astronomy & Astrophysics*, **663**, A95. doi: 10.1051/0004-6361/202243768.
- Mischna, M. A., et al. (2011). Atmospheric modeling of Mars methane surface releases. *Planetary and Space Science*, **59**(2–3), 227–237. doi: 10.1016/j.pss.2010.07.005.
- Montmessin, F., et al. (2021). A stringent upper limit of 20 pptv for methane on Mars and constraints on its dispersion outside Gale crater. *Astronomy and Astrophysics*, **650**, A140. doi: 10.1051/0004-6361/202140389.
- Moores, J. E., et al. (2019a). Methane seasonal cycle at Gale Crater on Mars consistent with regolith adsorption and diffusion. *Nature Geoscience*, **12**(5), 321–325. doi: 10.1038/s41561-019-0313-y.
- Moores, J. E., et al. (2019b). The methane diurnal variation and microseepage flux at Gale crater, Mars as constrained by the ExoMars Trace Gas Orbiter and Curiosity observations. *Geophysical Research Letters*, **46**(16), 9430–9438. doi: 10.1029/2019GL083800.
- Morley, C. V., et al. (2017). Observing the atmospheres of known temperate Earth-sized planets with JWST. *The Astrophysical Journal*, **850**(2), 121. doi: 10.3847/1538-4357/aa927b.
- Mumma, M. J., et al. (2009). Strong release of methane on Mars in northern summer 2003. *Science*, **323**(5917), 1041–1045. doi: 10.1126/science.1165243.
- Nair, H., et al. (1994). A photochemical model of the Martian atmosphere. *Icarus*, **111**(1), 124–150. doi: 10.1006/icar.1994.1137.
- Nakamura, N., & Held, I. M. (1989). Nonlinear equilibration of two-dimensional Eady waves. *Journal of the Atmospheric Sciences*, **46**(19), 3055–3064. doi: 10.1175/1520-0469(1989)046%3c3055:NEOTDE%3e2.0.CO;2.
- Neale, R. B., et al. (2012). Description of the NCAR community atmosphere model (CAM 5.0). *NCAR Tech. Note NCAR/TN-486+ STR*, **1**(1), 1–12.
- Newman, C. E., et al. (2017). Winds measured by the Rover Environmental Monitoring Station (REMS) during the Mars Science Laboratory (MSL) rover's Bagnold Dunes Campaign and comparison with numerical modeling using MarsWRF. *Icarus*, **291**, 203–231. doi: 10.1016/j.icarus.2016.12.016.

- Newman, C. E., et al. (2020). Using InSight Wind Data to Validate Atmospheric Models and Improve Predictions for Other Locations on Mars. Paper presented at the AGU Fall Meeting 2020, online.
- Oehler, D. Z., & Etioppe, G. (2017). Methane seepage on Mars: Where to look and why. *Astrobiology*, *17*(12), 1233–1264. doi: 10.1089/ast.2017.1657.
- O'Malley-James, J. T., & Kaltenegger, L. (2017). UV surface habitability of the TRAPPIST-1 system. *Monthly Notices of the Royal Astronomical Society: Letters*, *469*(1), L26–L30. doi: 10.1093/mnrasl/slx047.
- Omand, M. M., et al. (2015). Eddy-driven subduction exports particulate organic carbon from the spring bloom. *Science*, *348*(6231), 222–225. doi: 10.1126/science.1260062.
- Oze, C., & Sharma, M. (2005). Have olivine, will gas: serpentinization and the abiogenic production of methane on Mars. *Geophysical Research Letters*, *32*(10). doi: 10.1029/2005GL022691.
- Pla-García, J., et al. (2019). Comparing MSL Curiosity rover TLS-SAM methane measurements with Mars Regional Atmospheric Modeling System atmospheric transport experiments. *Journal of Geophysical Research: Planets*, *124*(8), 2141–2167. doi: 10.1029/2018JE005824.
- Pollard, D., & Kasting, J. F. (2005). Snowball Earth: A thin-ice solution with flowing sea glaciers. *Journal of Geophysical Research: Oceans*, *110*(C7). doi: 10.1029/2004JC002525.
- Poppe, D., & Lustfeld, H. (1996). Nonlinearities in the gas phase chemistry of the troposphere: Oscillating concentrations in a simplified mechanism. *Journal of Geophysical Research: Atmospheres*, *101*(D9), 14373–14380. doi: 10.1029/96JD00339.
- Prather, M. J., et al. (1979). Stratospheric chemistry: Multiple solutions. *Geophysical Research Letters*, *6*(3), 163–164. doi: 10.1029/GL006i003p00163.
- Price, C., & Rind, D. (1992). A simple lightning parameterization for calculating global lightning distributions. *Journal of Geophysical Research: Atmospheres*, *97*(D9), 9919–9933. doi: 10.1029/92JD00719.
- Price, C., et al. (1997). NO_x from lightning: 1. Global distribution based on lightning physics. *Journal of Geophysical Research: Atmospheres*, *102*(D5), 5929–5941. doi: 10.1029/96JD03504.
- Proedrou, E., & Hocke, K. (2016). Characterising the three-dimensional ozone distribution of a tidally locked Earth-like planet. *Earth, Planets and Space*, *68*(1), 1–20. doi: 10.1186/s40623-016-0461-x.
- Putzig, N. E., et al. (2005). Global thermal inertia and surface properties of Mars from the MGS mapping mission. *Icarus*, *173*(2), 325–341. doi: 10.1016/j.icarus.2004.08.017.
- Rappaport, S., et al. (2012). Possible disintegrating short-period super-Mercury orbiting KIC 12557548. *The Astrophysical Journal*, *752*(1), 1. doi: 10.1088/0004-637X/752/1/1.

- Richardson, M. I., et al. (2007). PlanetWRF: A general purpose, local to global numerical model for planetary atmospheric and climate dynamics. *Journal of Geophysical Research: Planets*, **112**(E9). doi: 10.1029/2006JE002825.
- Schwieterman, E. W., et al. (2018). Exoplanet biosignatures: A review of remotely detectable signs of life. *Astrobiology*, **18**(6), 663–708. doi: 10.1089/ast.2017.1729.
- Segura, A., et al. (2003). Ozone concentrations and ultraviolet fluxes on Earth-like planets around other stars. *Astrobiology*, **3**(4), 689–708. doi: 10.1089/153110703322736024.
- Segura, A., et al. (2005). Biosignatures from Earth-like planets around M dwarfs. *Astrobiology*, **5**(6), 706–725. doi: 10.1089/ast.2005.5.706.
- Segura, A., et al. (2010). The effect of a strong stellar flare on the atmospheric chemistry of an Earth-like planet orbiting an M dwarf. *Astrobiology*, **10**(7), 751–771. doi: 10.1089/ast.2009.0376.
- Smith, D. E., et al. (2001). Mars Orbiter Laser Altimeter: Experiment summary after the first year of global mapping of Mars. *Journal of Geophysical Research: Planets*, **106**(E10), 23689–23722. doi: 10.1029/2000JE001364.
- Song, X., & Yang, J. (2021). Asymmetry and variability in the transmission spectra of tidally locked habitable planets. *Frontiers in Astronomy and Space Sciences*, **8**:708023. doi: 10.3389/fspas.2021.708023.
- Stein, A. F., et al. (2015). B., Cohen, MD, and Ngan, F.: NOAA'S HYSPLIT atmospheric transport and dispersion modeling system, *Bulletin of the American Meteorological Society*, **96**, 2059–2077. doi: 10.1175/BAMS-D-14-00110.1.
- Stewart, R. W. (1995). Dynamics of the low to high NO_x transition in a simplified tropospheric photochemical model. *Journal of Geophysical Research: Atmospheres*, **100**(D5), 8929–8943. doi: 10.1029/95JD00691.
- Stone, P. H. (1966). On non-geostrophic baroclinic stability. *Journal of the Atmospheric Sciences*, **23**(4), 390–400. doi: 10.1175/1520-0469(1966)023%3c0390:ONGBS%3e2.0.CO;2.
- Stone, P. H., et al. (1969). Preliminary results of experiments with symmetric baroclinic instabilities. *Journal of Atmospheric Sciences*, **26**(5), 991–996. doi: 10.1175/1520-0469(1969)026%3c0991:PROEWS%3e2.0.CO;2.
- Stone, P. H. (1970). On non-geostrophic baroclinic stability: Part II. *Journal of Atmospheric Sciences*, **27**(5), 721–726. doi: 10.1175/1520-0469(1970)027%3c0721:ONGBSP%3e2.0.CO;2.
- Stone, P. H. (1971). Baroclinic stability under non-hydrostatic conditions. *Journal of Fluid Mechanics*, **45**(4), 659–671. doi: 10.1017/S0022112071000260.
- Tamburo, P., et al. (2018). Confirming variability in the secondary eclipse depth of the super-Earth 55 Cancri e. *The Astronomical Journal*, **155**(5), 221. doi: 10.3847/1538-3881/aabd84.

- Thomson, D. J. (1987). Criteria for the selection of stochastic models of particle trajectories in turbulent flows. *Journal of Fluid Mechanics*, **180**, 529–556. doi: 10.1017/S0022112087001940.
- Thomas, L. N., et al. (2008). Submesoscale processes and dynamics. *Ocean Modeling in an Eddy Regime*, **177**, 17–38. doi: 10.1029/177GM04.
- Tinsley, M. R., & Field, R. J. (2001a). Steady state instability and oscillation in simplified models of tropospheric chemistry. *The Journal of Physical Chemistry A*, **105**(50), 11212–11219. doi: 10.1021/jp010571t.
- Tinsley, M. R., & Field, R. J. (2001b). Dynamic instability in tropospheric photochemistry: An excitability threshold. *Geophysical Research Letters*, **28**(23), 4437–4440. doi: 10.1029/2001GL013675.
- Toigo, A. D., et al. (2012). The impact of resolution on the dynamics of the Martian global atmosphere: Varying resolution studies with the MarsWRF GCM. *Icarus*, **221**(1), 276–288. doi: 10.1016/j.icarus.2012.07.020.
- Van Roekel, L., et al. (2018). The KPP boundary layer scheme for the ocean: Revisiting its formulation and benchmarking one-dimensional simulations relative to LES. *Journal of Advances in Modeling Earth Systems*, **10**(11), 2647–2685. doi: 10.1029/2018MS001336.
- Webster, C. R., et al. (2015). Mars methane detection and variability at Gale crater. *Science*, **347**(6220), 415–417. doi: 10.1126/science.1261713.
- Webster, C. R., et al. (2018). Background levels of methane in Mars' atmosphere show strong seasonal variations. *Science*, **360**(6393), 1093–1096. doi: 10.1126/science.aaq0131
- Webster, C. R., et al. (2021). Day-night differences in Mars methane suggest nighttime containment at Gale crater. *Astronomy and Astrophysics*, **650**(2021) A166. doi: 10.1051/0004-6361/202040030.
- White, W. H., & Dietz, D. (1984). Does the photochemistry of the troposphere admit more than one steady state?. *Nature*, **309**(5965), 242–244. doi: 10.1038/309242a0.
- Wilson, D. J., et al. (2021). The Mega-MUSCLES spectral energy distribution of TRAPPIST-1. *The Astrophysical Journal*, **911**(1), 18. doi: 10.3847/1538-4357/abe771.
- Wolf, E. T. (2017). Assessing the habitability of the TRAPPIST-1 system using a 3D climate model. *The Astrophysical Journal Letters*, **839**(1), L1. doi: 10.3847/2041-8213/aa693a.
- Wunderlich, F., et al. (2019). Detectability of atmospheric features of Earth-like planets in the habitable zone around M dwarfs. *Astronomy & Astrophysics*, **624**, A49. doi: 10.1051/0004-6361/201834504.
- Yates, J. S., et al. (2020). Ozone chemistry on tidally locked M dwarf planets. *Monthly Notices of the Royal Astronomical Society*, **492**(2), 1691–1705. doi: 10.1093/mnras/stz3520.
- Yienger, J. J., & Levy, H. (1995). Empirical model of global soil-biogenic NO_x emissions. *Journal of Geophysical Research: Atmospheres*, **100**(D6), 11447–11464. doi: 10.1029/95JD00370.

- Yung, Y. L., & DeMore, W. B. (1982). Photochemistry of the stratosphere of Venus: Implications for atmospheric evolution. *Icarus*, **51**(2), 199–247. doi: 10.1016/0019-1035(82)90080-X.
- Yung, Y. L., et al. (1984). Photochemistry of the atmosphere of Titan: Comparison between model and observations. *Astrophysical Journal Supplement Series*, **55** (3), 465–506. doi: 10.1086/190963.
- Yung, Y. L., et al. (2018). Methane on Mars and habitability: Challenges and responses. *Astrobiology*, **18**(10), 1221–1242. doi: 10.1089/ast.2018.1917.
- Zahnle, K. (2015). Play it again, SAM. *Science*, **347**(6220), 370–371. doi: 10.1126/science.aaa3687.